Canadian Journal of Analytical Sciences and Spectroscopy

CONTENTS   VOLUME 52, No. 5

Impact of sample preparation process on protein/peptide marker identification: shot-gun screening by MALDI-TOF-MS

Susantha Mohottalage, Subramanian Karthikeyan, Renaud Vincent and Prem Kumarathasan*

Inhalation Toxicology and Aerobiology Section, Safe Environments Programme, Healthy Environments and Consumer Safety Branch, Health Canada, Tunney's Pasture, PL0803C, Ottawa, ON, Canada, K1A 0K9

Abstract

Sample preparation scenarios were assessed for use in rapid screening of potential toxicological biomarkers using matrix assisted laser desorption ionization-time of flight mass spectrometry (MALDI-TOF-MS). Plasma from Fisher 344 rats exposed to clean air or ozone served as a model to examine factors affecting reliability of biomarker analyses. Plasma samples were clarified by either 10 kDa or 30 kDa molecular weight cut-off (MWCO) filters, and spotted either directly on MALDI-targets or after clean-up using Vivapure C18 spin cartridges. Our results showed reduced number of mass spectral peaks for samples clarified by 30 kDa filtration. Analyte losses were also noted with C18 clean-up, and so was increased analytical variation. Mass spectral information mined using the bioinformatics software ClinProTools identified a model consisting of 5 candidate biomarkers (m/z 1070.3, 1144.5, 1570.2, 1738.3 and 2095.8 Da) that best differentiated ozone and air exposures. Percent true classification values were higher for test data sets of samples prepared by 10 kDa filtration irrespective of C18 clean-up. Furthermore, a semi-quantitative analysis of specific candidate markers identified in samples prepared by 10 kDa filtration also showed a significant (p<0.05) ozone-dependent increase in expression. Overall, our results suggest that sample preparation process can affect the integrity of biomarker identification.

Keywords*: sample preparation, biomarker, protein/peptide screening, MALDI-TOF-MS, data mining.*

Résumé

On a évalué les scénarios de préparation des échantillons aux fins de dépistage rapide des biomarqueurs toxicologiques potentiels par la technique MALDI-TOF-MS. Le plasma de rats 344 Fisher exposés à l'air ou à l'ozone a servi de modèle pour examiner les facteurs influant sur la fiabilité des analyses de biomarqueurs. On a clarifié les échantillons avec nos filtres de coupure par poids moléculaire (PM) de 10 kDa ou 30 kDa. Les filtrats ont été ensuite observés sur cibles MALDI, directement ou après nettoyage à l'aide de cartouches à rotation Vivapure C18. Nos résultats ont démontré moins de pointes dans la masse spectrale pour le plasma clarifié à l'aide des filtres de coupure à 30 kDa. Les pertes d'analyte ont été observées lors du nettoyage au C18, ainsi qu'une variation analytique plus importante. L'information sur la masse spectrale obtenue à l'aide du logiciel bio-informatique ClinProTools pour biomarqueurs, a permis de cerner le meilleur modèle permettant de différencier l'exposition à l'ozone de l'exposition à l'air; ce modèle comprend 5 marqueurs potentiels (m/z 1070.3, 1144.5, 1570.2, 1738.3 et 2095.8 Da). Les valeurs de pourcentage de classification réelles étaient plus élevées pour les échantillons préparés avec le filtre 10kDa, avec ou sans nettoyage au C18. En outre, l'analyse semi-quantitative de marqueurs potentiels spécifiques identifiés dans les échantillons filtrés à 10 kDa a démontré une augmentation significative (p<0.05) avec traitement, comparativement aux contrôles. Dans l'ensemble, nos résultats laissent supposer que le processus de préparation des échantillons peut influer sur l'intégrité de l'identification des biomarqueurs.

*Author to whom correspondence should be addressed: e-mail: Premkumari_kumarathasan@hc-sc.gc.ca

Introduction

Proteins are involved in virtually all cellular functions, control cellular regulatory mechanisms, and are potentially modified under various pathological conditions. Proteome analysis thus can be used to identify sensitive and specific markers of biological changes to assess adverse effects of external stimuli/insult to an organism. The typical proteome approach used involve initial separation of proteins by two-dimensional polyacrylamide gel electrophoresis (2D-PAGE), high performance liquid chromatography or by capillary electrophoresis (CE) followed by identification using mass spectrometry (1-9). Although 2D-PAGE is unchallenged in its ability to resolve thousands of proteins, this technique is laborious, time-consuming, requires large quantities of proteins and cannot be easily converted into a fast screening test.

The development of surface-enhanced laser desorption/ionization-time of flight (SELDI-TOF) MS permitted comparably convenient protein marker screening (10). SELDI is an affinity-based MS method in which proteins are selectively adsorbed to a chemically modified surface (Ciphergen ProteinChip® Array), and are characterized using a time-of-flight mass spectrometer (11). Although this approach is robust and amenable to automation and handles crude biological samples, it suffers due to inferior resolution and accuracy of analysis compared to MALDI-TOF-MS. The MALDI-TOF-MS technology therefore, appears to be attractive for the purpose of screening for proteins/peptides. Even though MALDI analysis can be adversely affected by matrix interference from the sample, this can be overcome by proper clean-up procedures (3). A potential problem that can arise due to direct analysis without pre-purification or fractionation of complex biological matrices such as plasma by MALDI-TOF-MS is occurrence of signal suppression that is caused by competition for proton during ionization. There are reports on factors affecting the quality of mass spectra when direct protein analyses are conducted.(12, 13) On the other hand, with complex matrices, use of multiple steps for sample clean-up or fractionation prior to analysis by MALDI-TOF-MS can introduce experimental artefacts such as sample auto-oxidation and potential analyte loss. It is essential to find a balance of such phenomena to get optimal information for reliable investigation of toxicological markers.

The aim of present study was therefore, to identify a quick and simple sample preparation method to obtain optimal and reproducible mass spectral information on proteins and peptides in complex biological matrices using MALDI-TOF-MS that can be applied to screen for treatment-related markers. In this study we have used plasma samples, derived from Fisher 344 male rats, which were exposed to air or ozone to evaluate these methods.

Experimental

Chemicals

Analytical grade purity acetonitrile (ACN) was obtained from common commercial suppliers. De-ionized water was laboratory-generated using de-ionized water generating system (Millipore, Milli-QTM). Nitrogen (N_2) was of ultra high purity (UHP) grade and was obtained from Praxair (Mississauga, ON, Canada). Peptide calibration standard II (bradykinin 1-7, angiotensin II, angiotensin I, substance P, bombesin, rennin substrate, ACTH clip 1-17, ACTH clip 18-39, somatostatin 28), protein calibration standard I (insulin, ubiquitin I, cytochrome C and myoglobin) and α-cyano-4-hydroxycinnamic acid were procured from Bruker Daltonics GmbH (Leipzig, Germany). Ten kDa and 30 kDa ultrafree-microcentrifuge MWCO filters, trifluoroacetic acid (TFA), ethylenediaminetetraacetic acid (EDTA), phenylmethylsulfonyl fluoride (PMSF), diethylenetriaminepentaacetic acid (DETPA) were purchased from Sigma-Aldrich Co. (St. Louis, MO, USA). Butylatedhydroxytoluene (BHT) was purchased from United States Biochemical Corporation (Cleveland, OH, USA). Vivapure® C18 type salt removing micro spin cartridges were purchased from Vivascience AG, (Hannover, Germany).

Biological Samples

Fisher 344 male rats (body weight 200-250g, barrier raised, specific pathogen-free) were obtained from Charles River (St-Constant, PQ, Canada) at least one week before the experiments and were given food and water *ad libitum*. The animals were maintained following the standard operating procedures established by the Animal Resources Division, Health Canada, and pursuing the guidelines of the Canadian Council on Animal care. The experimental procedures were reviewed by the Animal Care Committee of Health Canada. Rats (N=4-6) were exposed to clean air or ozone (0.8 ppm) for 4 hr by nose only exposure as described by Kumarathasan *et al.* (14). Immediately after exposure, the animals were anaesthetized with sodium pentobarbital (65 mg/kg, ip). The trachea was exposed and cannulated; blood was withdrawn from the abdominal aorta and transferred

into vacuutainer tubes (15) containing EDTA and PMSF, as stabilizers. Blood samples were centrifuged at 2800 rpm (IEC, MicroMAX®) for 10 min to collect plasma. Plasma samples were treated with BHT and DETPA, additional stabilizers to prevent autoxidation of samples as reported earlier (14).

Plasma sample preparation

Plasma samples (80 µl) were diluted with acetonitrile, (ACN, 20µl) and vortexed. Samples were passed via either 10 kDa or 30 kDa MWCO filters and centrifuged at 7500 rpm for 30 min. Each filter was washed separately with 20% ACN: H_2O in 0.1% TFA (50 µl), centrifuged at the settings mentioned above, then the first and the corresponding second filtrates of the same samples were combined. The combined filtrates were then divided into two portions of which one set of aliquots was directly subjected to MALDI-TOF analysis. The other set of identical aliquots (60 µl) were subjected to clean-up using Vivapure® C18 micro spin cartridges (Vivascience, Hannover, Germany) after evaporation to 20 µl to remove any ACN. These cartridges were then washed with 50 µl of acidified deionized water (0.1% TFA) and then eluted with 50 µl of 30% ACN (0.1% TFA) followed by 50 µl of 60% ACN (0.1% TFA). Both eluates of the same sample were combined and evaporated to dryness and reconstituted with 50% ACN in 0.1% TFA (10 µl). These samples were then subjected to MALDI-TOF-MS analysis. There were four types of samples that were generated: Procedure 1. 10 kDa, direct; Procedure 2. 10 kDa, VP clean-up; Procedure 3. 30 kDa, direct; Procedure 4. 30 kDa, VP clean-up. All sample preparations were carried out in duplicates.

Saturated solution of α-cyano-4-hydroxy cinnamic acid (dissolved in 50% ACN:0.1%TFA in H_2O) was used as matrix. All samples were spotted according to the dried-droplet method (16) where 1µl matrix solution was spotted on the AnchorChip target plate (600/384F, Bruker Daltonics) followed by placing of 1µl of the sample on top of the matrix solution and mixed on the target plate by gentle up/down motion of the pipette tip and allowed it to dry. On-target plate wash was then performed to the dried sample prior to MALDI-TOF analysis according to the procedure described by Kumarathasan *et al* (3). In brief, the sample/matrix spots were washed on target with 1µl of cold acidified deionized water (0.1% TFA), left for 5s, followed by removal of solvent and dried in order to remove any salt.

MALDI-TOF-MS analysis

Mass spectra were obtained on an Autoflex MALDI-TOF mass spectrometer (Bruker Daltonics), equipped with a pulsed nitrogen laser (337 nm) and FlexControl software for data collection. Detection mode was linear positive. Operating conditions were as follows; lens voltage=7.30 kV, ion source 1=20.00 kV, ion source 2=17.80 kV, pulsed ion extraction time=550 ns, matrix suppression=1000 Da, detector gain voltage=820 V. Four spectra were collected from four random points per sample, where each spectrum was obtained with 80 laser shots per point. The mass spectrometer was calibrated using a mixture of peptide calibration standard II and protein calibration standard I every time prior to sample analysis.

Data-mining

Mass spectra derived from analysis of plasma samples from Fischer rats exposed to clean air (controls) or ozone (0.8 ppm) were data-mined using the bioinformatics software ClinProTools (version 1.0; Bruker Daltonics) for potential biomarker candidates. This software allowed building of two-class (e.g. air versus ozone) fitting models. A model is a set of peaks selected across the spectra by the program, which allowed differentiation of the two treatment groups compared, leading to the identification of potential biomarkers. Initially, a training data set consisting of spectra of a set of samples derived from clean air or ozone treated animals was used to generate a best-fit model by ClinProTools software. This software automatically normalized imported spectral data to the total ion count of individual spectra, adjusting for any variations in spectral intensities. During data pre-treatment, each spectrum was re-calibrated based on observed baseline shifts, and peak areas were normalized (to obtain an average of 0 and standard deviation of 1 for each peak, over all spectra analyzed) to assign equal significance to both small and large peaks, for the purposes of inclusion in the models during model generation. Models with high fitness values approaching 1 were further validated by using a blind test data set. This blind test data set consisted of spectra from another set of samples that were not used in the generation of training data set, but were still from animals exposed to either clean air or ozone. The best-fit model that classified the blind test spectra into their respective treatment groups was then obtained. Peaks contributing to this model with high predictive capacity were chosen as candidate biomarkers. Also, during separate semi-quantitative analysis of the candidate biomarkers, statistical analysis was done using

Sigma Stat software (Jandel Scientific) by t-test.

Results and Discussion

Plasma samples from the air control animals were used initially to assess analytical performances of the four procedures, while final biomarker analysis employed both treatment groups. Figure 1 illustrates a comparison of mass spectral information on plasma proteins/peptides from samples obtained by procedures 1 (10 kDa, direct) and 3 (30 kDa, direct). Even though 30 kDa clarification exhibited masses up to 12 kDa, the number of peaks in mass region <6 kDa was comparably less to that in mass spectra of samples obtained using 10 kDa clarification.

Results shown in Table 1, are the averaged data from assessment of N=4 air control animals, and four randomly picked spectra across procedures to give a realistic scenario of the effect of procedures on mass spectral information. Procedure 1 (10 kDa, direct) gave the highest number of observed peaks in this mass region (<6 kDa) among all four sample preparations (Table 1). Number of common peaks between procedures 1&2 were greater than the number of common peaks among procedures 1&3, and common peaks between procedures 3&4 were ≥ the number of peaks that were common among all procedures (Table 1). These results indicate that samples derived by 10 kDa preparations were behaving similarly compared to the differences seen between 30 kDa preparations irrespective of the additional clean-up. The observation of less mass spectral peaks with procedure 3&4 compared to 1&2 in the common mass region (<6 kDa) can be attributed to a comparably enhanced competition in protonation process during ionization due to the presence of protein/peptide species in the m/z region > 6 kDa in the former procedures as opposed to the latter (Table 1). This is in line with the findings of Knochenmuss *et al.*(17) Observation of consistently reduced number of mass spectral peaks with C18 Vivapure clean-up, in contrast to procedures (1 & 3) that did not include this sample clean-up step (Table 1) irrespective of pre-clarification using 10 or 30 kDa filters, indicated selective loss of some protein/peptide species, due to C18 clean-up. Similar observations of analyte loss with C18 clean-up have been reported previously (18).

Assessment of analytical reproducibility of MALDI sample preparation expressed as percent coefficient of variance (%CV) for duplicate samples, was better in general for samples clarified with MWCO filters alone as compared to samples that underwent further clean-up as demonstrated by the comparison of intensity values

for procedures 1&2 (Table 2). Comparison of intensity values also suggested that while selected protein/peptide species were decreased or lost, the others were concentrated with C18 clean up in procedure 2 (Table 2). Results in Table 2 also indicated that with procedure 2, the %CV decreased with increasing m/z value. The overall decrease in analytical precision of procedure 2 can be due to a combination of factors such as non-reproducible recoveries, and concentration-dependent solubility characteristics of these species during final sample reconstitution.

Similarly, the evaluation of analytical precision values expressed as %RSD that reflects the inter-animal variations (N=6) exhibited an overall adverse impact of additional VP clean-up procedure as shown in Table 3. This was also the case for 30 kDa MWCO pre-fractionation (data not shown). These observations are consistent with the previous notion that additional sample clean-up by VP filtration can negatively impact on sample integrity (18). In general, the overall analytical precision values were better for procedure 1 (10 kDa, direct) compared to the other three sample preparation procedures.

As the most number of peaks were obtained with sample preparation procedure 1 along with optimal reproducibility, mass spectral data from analysis of plasma samples from both air controls and ozone exposed animals, prepared by this method, in duplicates (N=8-12 spectra) were used as training data for model generation. Model building was done by selection of a subset of relevant peaks and establishing clusters using the areas of these peaks. This approach was taken to increase the power of the training data set in order to generate reliable models.(19) Figure 2, illustrates the best-fit model generated using this training data set. This model was validated against blind independent test data generated from another set of samples from air control and ozone exposed animals, prepared using the different procedures by comparing the true classification efficiency of this model in classifying spectra into their respective exposure groups. Classification into the appropriate exposure groups was done using k nearest neighbour clustering criterion. These results (Table 4) showed that the best-fit model gave good classification of the test data truly into the two treatment groups (air and ozone-exposed), for samples prepared by both procedures 1 and 2, of which the latter gave better true classification results.

The best-fit model consisted of 5 potential markers (m/z 1070.3, 1144.5, 1570.2, 1738.3 and 2095.8 Da) of ozone effect (Figure 2). These marker peaks were checked to verify if they corresponded to matrix cluster
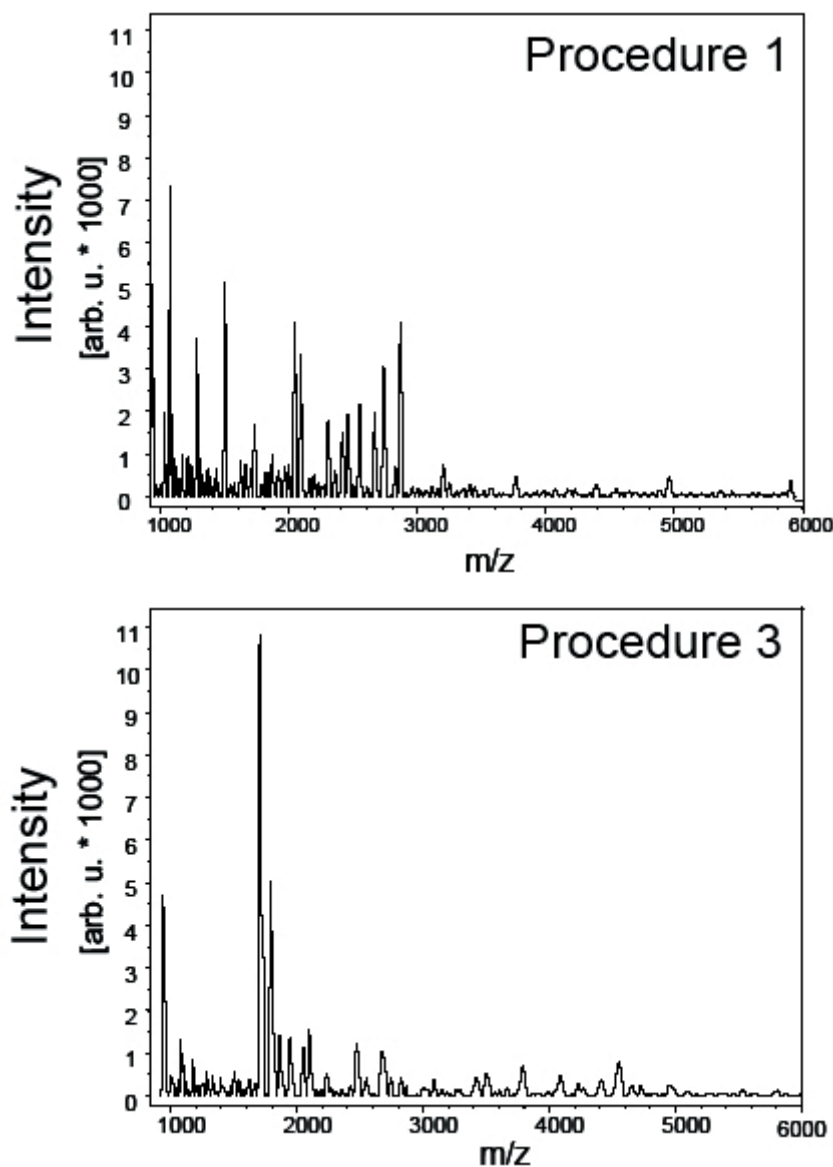
Figure 1: Comparison of mass spectra of rat plasma samples obtained by procedures 1 (10 kDa, direct) and 3 (30 kDa, direct).

Table 1: Mass spectral peak profiles of plasma samples clarified by the four sample preparation procedures.

Procedure	Numbers of peaks common between procedures			Number of peaks common across all procedures	Total number of peaks obtained with each procedure
	2	3	4		
1	56 ± 5	47 ± 5	31 ± 3		115 ± 14
2		43 ± 6	28 ± 8		101 ± 7
3			20 ± 6	15 ± 3	93 ± 9
4					62 ± 9

Table 2: Assessment of variability in MALDI-TOF-MS analysis of duplicate samples.

m/z	Procedure 1			Procedure 2		
	Intensity 1	Intensity 2	%CV	Intensity 1	Intensity 2	%CV
1502.0	6362	6175	2.11	11192	15865	24.42
1735.8	2117	2461	10.63	5306	7642	25.51
1975.6	718	871	13.62	3164	2463	17.62
2666.0	2491	2464	0.77	1321	1079	14.26
3199.0	933	905	2.15	3607	3397	4.24
4397.8	387	349	7.30	908	926	1.39
4553.3	239	214	7.80	1522	1554	1.47

Figure 2: The five candidate protein/peptide markers of ozone exposure in rat plasma as determined by the best fit model.

Figure 3: Relative intensity profiles of the five candidate markers of ozone exposure (* significance, p<0.05)

adducts, and they were confirmed as peaks other than matrix cluster adducts. A separate semi-quantitative analysis of these potential marker peaks were carrie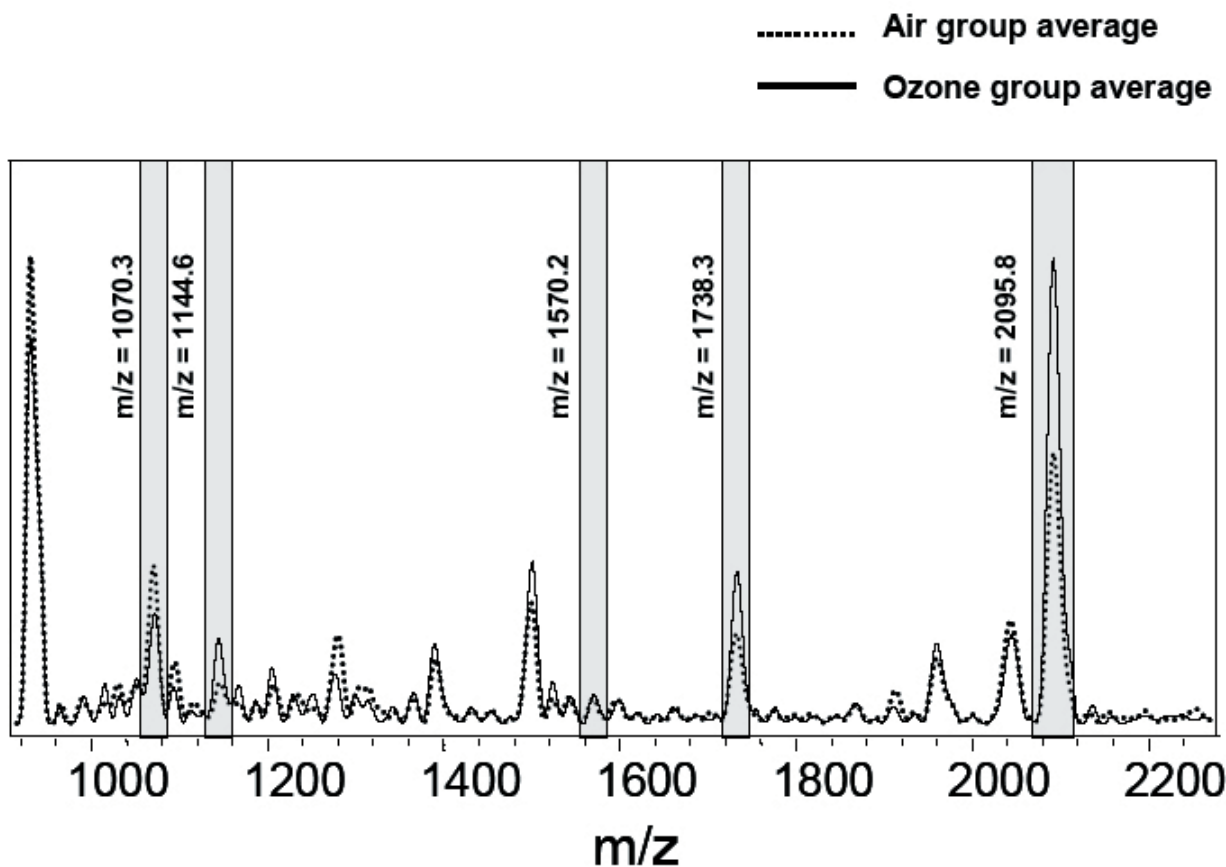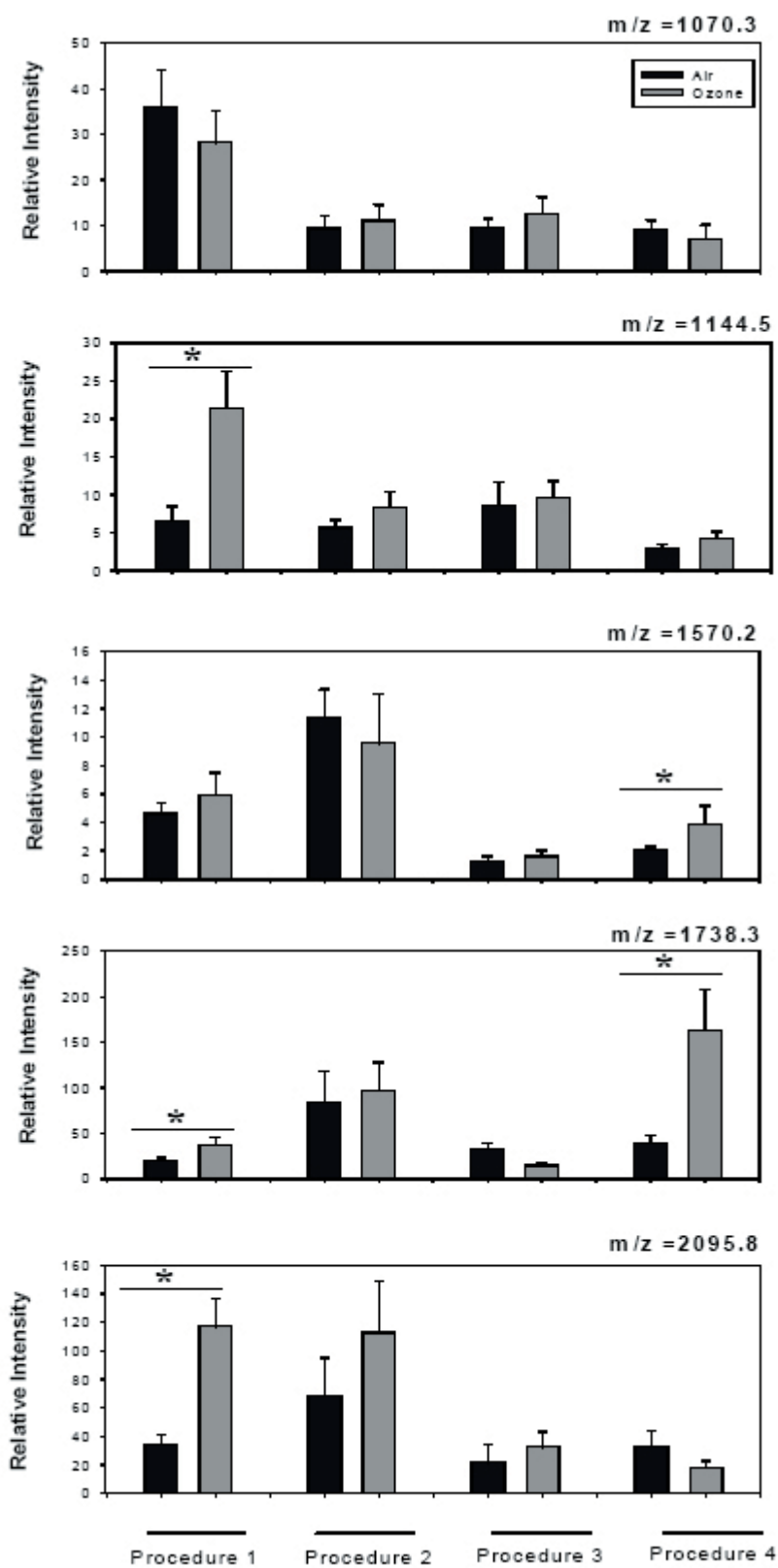d out by determining relative intensities that were calculated relative to the matrix ion peaks for each individual spectrum. The relative intensity profiles for each candidate marker reflecting the effect of exposure and the effect of sample preparation procedures are illustrated in Figure 3. All five of these candidate marker profiles for air vs ozone exposure groups in Figure 3 are similar to the relative changes in these markers seen with ClinProTools generated profile in Figure 2, only for Procedure 1. Although the peaks at m/z 1144.5 and 2095.8 exhibited similar increasing trends with ozone exposure, compared to air controls for procedures 1, 2 and 3, peaks at m/z 1738.3 and 1570.2 show similar ozone exposure effects for at least three of the four sample preparation procedures in which procedure 1 is always one of them.(Figure 3) The marker peak at m/z 1070.3 shows ozone exposure related decreasing trend compared to air controls for procedures 1&4, while an increasing trend for procedures 2&4 making this a questionable one.(Figure 3)

These observations suggest that sample preparation can have a major impact on identification of true biomarkers. For instance, the fact that procedures 1&2 which yielded better true classification results (Table 4) consistently show increasing trends for markers at m/z 1144.5, 1738.3 and 2095.8 with ozone exposure (Figure 3) and notably significant increases ($p < 0.05$) for procedure 1, enhance confidence in these markers. It appears that enhancement of inter-animal variations by variation due to the procedure (Table 3) had adversely impacted on detection of ozone-induced changes as seen by these markers not reaching significance with procedure 2. It is important to note that although procedure 2 classified the two exposure groups better than procedure 1, yet the latter procedure classified the ozone exposure groups to the same extent as procedure 2.

These results suggest that signal suppression in MALDI-TOF-MS analysis along with loss of sample integrity by additional C18 clean-up can introduce serious experimental artefacts and lead to erroneous results in biomarker identification. As the five candidate markers of ozone exposure gave true classification of ozone exposed group, with three of these markers significantly increased by ozone exposure following procedure 1, this method is determined to be superior to the other three methods, and emphasizes the critical role that sample processing methods play in reliable biomarker analyses.

Conclusions

In essence, shot-gun protein/peptide analysis methods can be useful in fast screening for markers of treatment effects in rat plasma. Nevertheless, it is crucial

Table 3: Effect of sample preparation process on inter-animal variabilities.

m/z	Procedure 1		Procedure 2	
	Average intensity (N = 6)	%RSD	Average intensity (N = 6)	%RSD
1502.8	3981	44.10	6988	164.52
2047.6	2913	51.87	10052	63.65
2096.1	5329	45.66	5875	158.28
4388.7	230	48.35	512	71.36
5914.1	618	34.81	705	41.78

Table 4: Predictive capacity of the best-fit model in classifying the blind test data generated by different sample preparation methods.

	Percent true classification of test data into respective groups	
	% True, Air	% True, O$_3$
Procedure 1	66.7	87.5
Procedure 2	83.3	87.5
Procedure 3	100	0
Procedure 4	100	0

that sample preparation procedures employed in such analyses are critically assessed for generation of potential experimental artifacts that can negatively impact on the integrity of biomarker investigations. In this study, we conclude that procedure 1 is better suited for fast screening of effects of ozone exposure compared to the rest of the three plasma preparation procedures.

Acknowledgements

References

1. A.C. Bergman, T. Benjamin, A. Alaiya, M. Waltham, K. Sakaguchi, B. Franzen, S. Linder, T. Bergman, G. Auer, E. Appella, P.J. Wirth and H. Jornvall, *Electrophoresis*, **21**, 679 (2000).

2. X. Tan, D. Cai, Y. Wu, B. Liu, L. Rong, Z. Chen and Q. Zhao, *Transl. Res.*, **148**, 114 (2006).

3. P. Kumarathasan, S. Mohottalage, P. Goegan and R. Vincent, *Anal. Biochem.*, **346**, 85 (2005).

4. J.A. Burgess, P. Lescuyer, A. Hainard, P.R. Burkhard, N. Turck, P. Michel, J.S. Rossier, F. Reymond, D.F. Hochstrasser and J.C. Sanchez. *J. Proteome. Res.*, **5**, 1674 (2006).

5. M. Jemal, S. Khan, D.S. Teitz, J.A. McCafferty and D.J. Hawthorne, *Anal. Chem.*, **73**, 5450 (2001).

6. N.I. Govorukhina, A. Keizer-Gunnink, A.G. van der Zee, S. de Jong and H.W. de Bruijn, *J. Chromatogr. A.*, **1009**, 171 (2003).

7. N.V. Neuhoff, T. Kaiser, S. Wittke, R. Krebs, A. Pitt, A. Burchard, A. Sundmacher, B. Schlegelberger, W. Kolch and H. Mischak, *Rapid Commun. Mass Spectrom.*, **18**, 149 (2004).

8. E.M. Weissinger, S. Wittke, T. Kaiser, H. Haller, S. Bartel, R. Krebs, I. Golovko, H.D. Rupprecht, M. Haubitz, H. Hecker, H. Mischak and D. Fliser, *Kidney Int.*, **265**, 2426 (2004).

9. H. Mischak, T. Kaiser, M. Walden, M. Hillmann, S. Wittke, A. Herrmann, S. Knueppel and H. Haller, D. Fliser, *Clin. Sci.*, **107**, 485 (2004).

10. T.W. Hutchens and T.T. Yip, *Rapid Commun. Mass Spectrom.*, **7**, 576 (1993).

11. M. Merchant and S.R Weinberger, *Electrophoresis*, **21**, 1164 (2000).

12. Z. Wang, L. Russon, L. Li, D.C. Roser and S.R. Long, *Rapid Commun. Mass Spectrom.*, **12**, 456 (1998).

13. T.L. Williams, D. Andrzejewski, J.O. Lay and S.M. Musser, *Am. Soc. Mass Spectrom.*, **14**, 342 (2003).

14. P. Kumarathasan, R. Vincent, P. Goegan, S. Bjarnason and J. Guenette, *Toxicol. Mech. Methods.*, **12**, 195 (2002).

15. P. Kumarathasan, R. Vincent, P. Goegan, M. Potvin, and J. Guenette, *Biochem. Cell Biol.*, **79**, 33 (2001).

16. M. Karas and F. Hillenkamp, *Anal. Chem.*, **60**, 2299 (1988).

17. R. Knochenmuss, A. Stortelder, K. Breuker and R. Zenobi, *J. Mass Spectrom.*, **35**, 1237 (2000).

18. N.S. Tannu, J. Wu, V.K. Rao, H.S. Gadgil, M.J. Pabst, I.C. Gerling and R. Raghow, *Anal. Biochem.*, **327**, 222 (2004).

19. X. Zhang, S. Leung,C.R. Morris and M.K. Shigenaga, *J Biomol. Tech.*, 15, 167 (2004).

Conformational properties and vibrational analyses of monomeric pentafluoropropionic acid CF$_3$CF$_2$COOH and pentafluoropropionamide CF$_3$CF$_2$CONH$_2$

H. M. Badawi*, M. A. A. Al-Khaldi[1], Z. H. A. Al- Sunaidi[1], S. S. A. Al-Abbad[1]

Department of Chemistry, King Fahd University of Petroleum & Minerals, Dhahran 31261, Saudi Arabia
[1]Girls College of Sciences at Dammam, Saudi Arabia

Abstract

The structural stability of pentafluoropropionic acid and pentafluoropropion-amide was investigated by DFT-B3LYP/6-311+G** and ab initio MP2/6-311+G** calculations. The calculated potential energy curves of the acid were consistent with two distinct minima that correspond to cis (C=O eclipses the C-C bond) and gauche conformers, with the latter being the lower energy form at ambient temperature. The equilibrium constant for the conformational interconversion of pentafluoropropionic acid were calculated at both levels of theory and found to correspond to an equilibrium mixture of about 76 % gauche and 24% cis conformations at 298.15 K. From the calculations, pentafluoroproionamide was predicted to exist only in the gauche conformation. The vibrational frequencies of pentafluoropropionic acid in the cis and the gauche conformers and pentafluoropropionamide in the gauche structure were computed at B3LYP level and complete vibrational assignments were made based on normal coordinate calculations and comparison with experimental infrared data of the molecules.

Résumé

Nous avons étudié la stabilité structurale de l'acide pentafluoropropionique et du pentafluoropropionamide avec des calculs DFT-B3LYP/6-311+G** et MP2/6-311+G** ab initio. Les courbes calculées d'énergie potentielle de l'acide étaient consistantes avec deux minimums distincts qui correspondent aux conformères cis (C=O éclipsant le lien C-C) et gauche, ce dernier étant à la plus basse énergie à température ambiante. La constante d'équilibre de l'interconversion conformationelle de l'acide pentafluoropropionique a été calculée aux deux niveaux théoriques et elle correspond à un équilibre d'une mélange des conformations d'environ 76 % gauche et 24% cis à 298.15 K. À partir de ces calculs, il est prédit que le pentafluoroproionamide existe seulement sous la conformation gauche. Nous avons calculé les fréquences de vibration de l'acide pentafluoropropionique sous les conformères cis et gauche et celle du pentafluoropropionamide dans sa structure gauche au niveau B3LYP et nous avons complété les attributions vibrationnelles en se basant sur des calculs de coordonnées normales et des comparaisons avec des données infrarouges expérimentales de ces molécules.

Introduction

Recently the investigation of the conformational stability of a series of halopropanals of the general formula R-CHO, where, R is CX$_3$CH$_2$, CHX$_2$CH$_2$, or CH$_2$XCH$_2$ and X is F or Cl were reported [1-4]. We investigated the structures of 3,3,3-trifluoropropanal [1], 3,3-difluoropropanal [2], 3-fluoropropanal [3] and 2,2,3,3,3-pentafluoropropanal [4] to study the effect of coupling between the carbonyl -CHO and the fluoromethyl rotors on the conformational stability of these molecules. The

calculation of the potential energy scans for the two rotor internal rotations in these molecules provided a clear idea about their conformational behavior and helped in the analysis of their complex vibrational spectra. In most of these molecules, the non-planar *gauche* conformations were predicted to be the lowest energy forms at ambient temperature. The calculated fluorine-oxygen equilibrium distance was found to be long enough for dipolar interactions that controlled predominantly the conformational equilibrium in these molecules [1-4].

In 3,3,3-trifluropropanal and 2,2,3,3,3-pentafluoro-propanal the *gauche* form was predicted to be thermo-dynamically more stable than the planar *cis* form [1, 4]. However, in 2,2,3,3,3-pentafluoropropanal the two conformers were calculated to have a very close relative stability [4]. In an earlier study of of 3,3-difluoropropanal the situation was more complex and the molecules were found to exist in a more complex mixture of *gauche* conformers at ambient temperature [2]. In the case of the mono derivative, 3-fluoropropanal [3] was determined to have the *trans-cis* form (FCCC = 180º and CCCO = 0º) as the lowest energy conformer [3]. The higher energy conformers were predicted to be the *gauche* conformations again with minimum fluorine-oxygen interaction in 3-fluoropropanal [3].

The corresponding acids R-COOH and amides R-CONH$_2$ are of greater structural and chemical interest, where the presence of the hydrogen bonding significantly influences the conformational behavior in these molecules. The structural properties of pentafluoropropionic acid [5-10] and pentafluoropropionamide [11-16] have been of interest for sometime. Crowder has investigated the infrared and Raman spectra of pentafluoropropionic acid in particular and reported that the acid is completely associated in the liquid state at room temperature [5]. In the liquid-state infrared spectrum only one carbonyl C=O stretching band and a broad O-H stretching band indicative of hydrogen bonding were observed, whereas there were two carbonyl bands and two O-H stretching bands were present in the vapor-state spectra [5]. Only the vibrational frequenceis that are associated with the carboxyl group were found to differ in the associated and monomeric forms [5]. The author also reported that the stronger hydrogen bonding in pentafluoropropionic acid as compared to trifluoroacetic acid indicates group electronegativities in the order CF$_3$ > CF$_2$CF$_3$ [5].

We optimized the energies and the structures of pentafluoropropinic acid and pentafluoropropionamide in the present study as the first molecules in a series of fluoronated propionac acids and amides at DFT-B3LYP

and *ab initio* MP2 levels using the extended 6-311+G** basis set. The vibrational wavenumbers of the low energy forms of pentafluoropropionic acid and pentafluoropro-pionamide were calculated and complete assignments were made for the normal modes by normal coordinate calculations and experimental mid-infrared data. The results of this work are presented herein.

Ab initio calculations

The GAUSSIAN 98 program [17] running on an IBM RS/6000 Model S85 Unix Server, was used to optimize the structures, predict the energies and dipole moments, and calculate vibrational frequencies of pentafluoro-propionic acid and pentafluoropropionamide in their possible stable forms (Tables 1-3). The 6-311G** and the 6-311+G** basis set were employed to carry out the calculations at the DFT-B3LYP and the *ab initio* MP2 levels of theory. The possible conformers of the com-pounds are determined by the rotation of the fluoromethyl CF$_3$ (FCCC dihedral angle is φ_1), the carbonyl (CCCO dihedral angle is φ_2) and the hydroxyl OH in the acid or the amino -NH in the amide (OCOH or OCNH dihedral angle is φ_3) groups around single bonds (see Figure 1).

The symmetric CF$_3$ potential energy scans
At first we calculated the symmetric CF$_3$ scans by varying the FCCC dihedral angle (φ_1) from 0º to 60º when the CCCO dihedral angle was kept constant at 180º (φ_2) and the OCOH or the OCNH (φ_3) dihedral angles were kept at 0º. Full geometry optimizations at the fixed dihe-dral angles φ_1 between 0 and 60º with an increment of 15 degrees were carried out at the DFT-B3LYP/6-311+G** level of calculation as shown in Figure 2.

The asymmetric CCCO and OCOH (or OCNH) poten-tial energy scans
The potential energy scans of the internal rotations about the C-C and the C-O (in the acids) or the C-N (in the amides) single bonds were similarly obtained by al-lowing the CCCO (φ_2) or the OCOH (φ_3) of the acid (or the OCNH of the amide) dihedral angles to vary from 0º (*cis* position) to 180º (*trans* position) as shown in Figures 3 and 4. The CCCO torsional potential was represented as a Fourier cosine series in the dihedral angle *(φ): V(φ) = V$_0$* + $\sum(V_n/2)[1-\cos(n\varphi)]$, where V_0 is the relative energy of the *cis* conformation and the potential coefficients from V_1 to V_6 are considered adequate to describe the potential function. The results of the energy optimizations were used to calculate the six coefficients by least-squares

Table 1. Calculated structural parameters, total dipole moment, and rotational constants of *cis* and *gauche* conformers of pentafluropropionic acid at DFT-B3LYP/6-311+G** and MP2/6-311+G** levels of theory.

| Parameter	B3LYP		MP2	
	Cis	*Gauche*	*Cis*	*Gauche*
Bond length (Å)				
$r\,(C_2\text{-}C_1)$	1.556	1.558	1.541	1.542
$r\,(C_3\text{-}C_1)$	1.551	1.5551	1.539	1.543
$r\,(O_4\text{=}C_3)$	1.196	1.194	1.205	1.203
$r\,(O_5\text{-}C_3)$	1.336	1.337	1.338	1.339
$r\,(F_6\text{-}C_2)$	1.340	1.335	1.335	1.330
$r\,(F_7\text{-}C_2)$	1.336	1.343	1.331	1.336
$r\,(F_8\text{-}C_2)$	1.336	1.336	1.331	1.333
$r\,(F_9\text{-}C_1)$	1.356	1.345	1.351	1.344
$r\,(F_{10}\text{-}C_1)$	1.356	1.358	1.351	1.350
$r\,(H_{11}\text{-}O_5)$	0.970	0.970	0.969	0.970
Bond angle (degree)				
$(C_3C_1C_2)$	114.0	114.0	113.5	112.7
$(O_4C_3C_1)$	124.1	123.1	124.0	122.8
$(O_5C_3C_1)$	109.6	110.4	109.3	110.3
$(F_6C_2C_1)$	109.1	110.2	109.0	110.2
$(F_7C_2C_1)$	110.7	109.5	110.4	109.4
$(F_8C_2C_1)$	110.7	111.1	110.4	110.4
$(F_9C_1C_2)$	107.9	107.7	107.9	107.7
$(F_{10}C_1C_2)$	107.9	108.2	107.9	108.0
$(H_{11}O_5C_3)$	108.3	108.4	106.9	106.8
$(F_6C_2C_1C_3)$	180.0	189.2	180.0	184.6
$(F_7C_2C_1F_6)$	119.3	119.5	119.3	119.9
$(F_8C_2C_1F_6)$	-119.3	-120.5	-119.3	-120.4
$(F_9C_1C_2C_3)$	121.6	120.5	121.4	120.2
$(F_{10}C_1C_2C_3)$	-121.6	-122.3	-121.4	-122.5
$(O_4C_3C_1C_2)$	0.0	112.4	0.0	99.6
$(H_{11}O_5C_3O_4)$	0.0	0.2	0.0	-1.2
Dipole moment (debye)				
μ_t	2.49	2.44	2.52	2.46
Rotational constants (MHz)				
A	2010	1885	2018	1883
B	1173	1167	1194	1178
C	1011	1089	1026	1129

Table 2: Calculated structural parameters, total dipole moment, and rotational constants of gauche conformer of pentafluoropropionamide at DFT-B3LYP/6-311+G** and MP2/6-311+G** levels of theory.

Parameter	B3LYP	MP2
Bond length (Å)		
r (C$_1$-C$_2$)	1.555	1.539
r (C$_1$-C$_3$)	1.558	1.546
r (C$_3$=O$_4$)	1.209	1.216
r (C$_3$-N$_5$)	1.351	1.355
r (C$_2$-F$_6$)	1.339	1.333
r (C$_2$-F$_7$)	1.331	1.328
r (C$_2$-F$_8$)	1.346	1.340
r (C$_1$-F$_9$)	1.350	1.344
r (C$_1$-F$_{10}$)	1.370	1.364
r (N$_5$-H$_{11}$)	1.009	1.009
r (N$_5$-H$_{12}$)	1.007	1.007
Bond angle (Degree)		
(C$_2$C$_1$C$_3$)	113.4	112.7
(C$_1$C$_3$O$_4$)	119.4	119.4
(C$_1$C$_3$N$_5$)	114.3	114.2
(C$_1$C$_2$F$_6$)	110.2	110.3
(C$_1$C$_2$F$_7$)	111.4	110.9
(C$_1$C$_2$F$_8$)	109.3	109.1
(C$_2$C$_1$F$_9$)	108.5	108.3
(C$_2$C$_1$F$_{10}$)	106.8	106.9
(C$_3$N$_5$H$_{11}$)	118.2	117.7
(C$_3$N$_5$H$_{12}$)	122.2	121.7
(F$_6$C$_1$C$_2$F$_7$)	120.7	120.8
(F$_6$C$_1$C$_2$F$_8$)	-118.9	-119.2
(C$_3$C$_2$C$_1$F$_9$)	121.6	121.2
(C$_3$C$_2$C$_1$F$_{10}$)	-122.5	-122.3
(C$_3$C$_1$C$_2$F$_6$)	173.6	176.9
(O$_4$C$_3$N$_5$H$_{11}$)	0.5	3.7
(O$_4$C$_3$N$_5$H$_{12}$)	178.4	171.8
(C$_2$C$_1$C$_3$O$_4$)	65.0	75.3
Dipole moment (debye)		
μ$_t$	4.00	4.14
Rotational constants (MHz)		
A	1885	1879
B	1157	1165
C	1083	1120

Table 3. DFT and ab initio MP2 energiesa E (Hartree) and energy differences ΔE (kcal/mol) between cis, gauche and trans structures of pentafluoropropionic acid and its amide.

Molecule/ Level	Energy E gauche	Energy differences[a], ΔE		
		cis	trans	(φ)[b]
Pentafluoropropionic acid				
B3LYP/6-311G**	-764.798902	0.479	1.296	(112.51)
MP2/6-311G**	-763.126033	0.685	1.601	(105.89)
B3LYP/6-311+G**	-764.823278	0.390	1.094	(112.37)
MP2/6-311+G**	-763.161923	0.344	1.145	(99.60)
Pentafluoropropionamide				
B3LYP/6-311G**	-744.932747	1.387	3.855	(63.8)
MP2/6-311G**	-743.276467	1.500	4.254	(69.1)
B3LYP/6-311+G**	-744.956923	1.331	3.476	(65.0)
MP2/6-311+G**	-743.312243	1.242	3.651	(74.4)

[a]Difference is relative to the *gauche* conformer.
[b]φ is the optimized CCCO torsional angle.
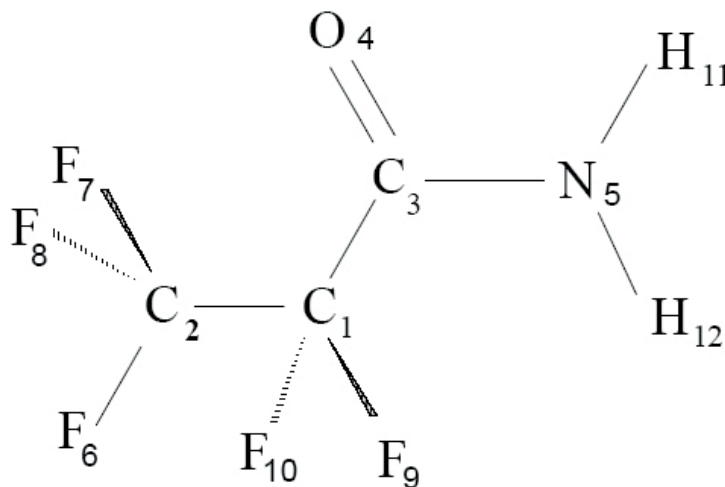
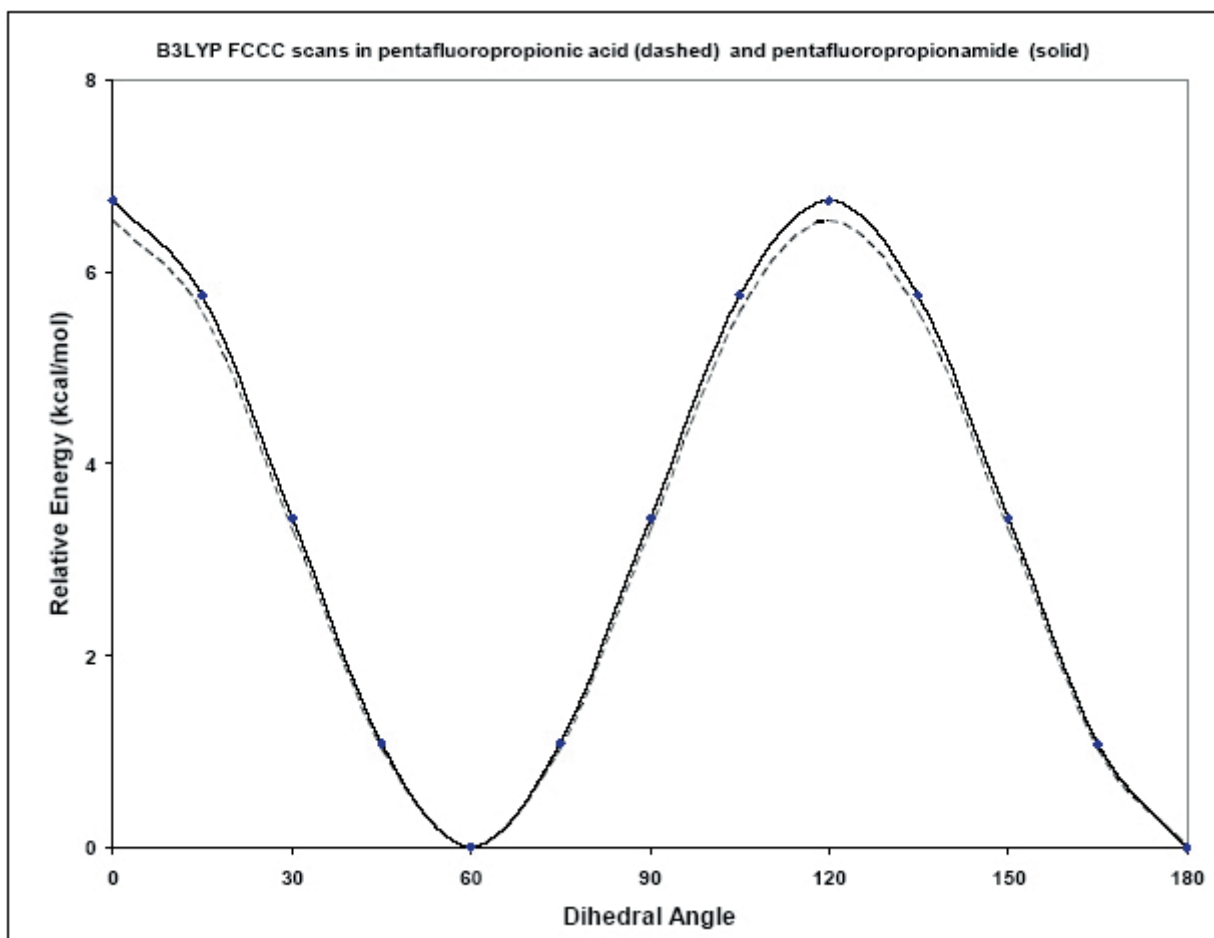
Figure 1. Atom numbering of *cis*-pentafluoropropionamide.

Figure 2. Calculated potential curves for the symmetric three-fold CF$_3$ torsions with CCCO and OCOH dihedral angles equal 180º degrees of pentafluoropropionic acid (dashed) and pentafluoropropionamide (solid) at B3LYP/6-311+G** level of theory.

fitting (Table 4).

Vibrational wavenumbers and normal coordinate analyses

The optimized structural parameters of penafluoropropionic acid and its amide were used to calculate the vibrational frequencies of their stable forms at the DFT-B3LYP/6-311+G** level of calculation. Normal coordinate analyses were carried out for the stable conformers of each molecule as described previously [18, 19]. The internal and symmetry coordinates of the molecules are listed in Tables 5-7. The potential energy distributions (PEDs) among the symmetry coordinates of each normal mode of the molecules were calculated and given in Tables 8-10. Reliable assignments of the fundamentals were proposed on the basis of the calculated PED values, infrared band intensities, Raman line activities, depolarization ratios and experimental mid-infrared spectra obtained from the link: http://www.aist.

go.jp/RIODB/SDBS (Figures 5 and 6). The data of the vibrational assignments are listed in Tables 8-10.

The vibrational infrared and calculated as described previously [20, 21]. The frequencies v_j and the infrared intensities of pentafluoropropionic acid and its amide were obtained from DFT-B3LYP/6-311+G** calculation. The observed and the calculated vibrational infrared spectra of the molecules in their ground state *gauche* conformation are shown in Figures 5 and 6.

Discussion

In the present study we investigated the structural stability of monomeric pentafluoropropionic acid as well as pentafluoropropionamide and tried to provide comprehensive analysis for the vibrational spectra of the two molecules on the basis of normal coordinate calculations. We calculated the potential energy scans for the CF$_3$, the CCCO and the OCOH (or OCNH) in-
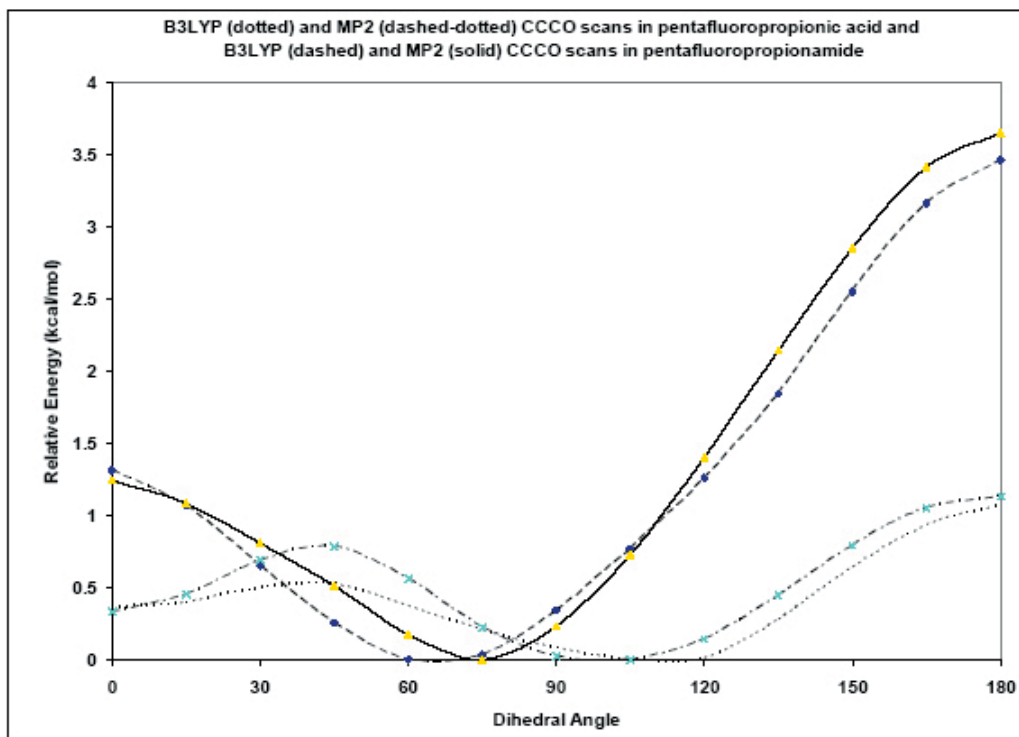
Figure 3. Calculated potential curves for the CCCO torsion with FCCC = 180 and OCOH (or OCNH) = 0 degree of pentafluoropropionic acid at B3LYP/6-311+G** (dotted) and MP2/6-311+G** (dashed-dotted) and pentafluoropropionamide at B3LYP/6-311+G** (dashed) and MP2/6-311+G** (solid) levels of theory.
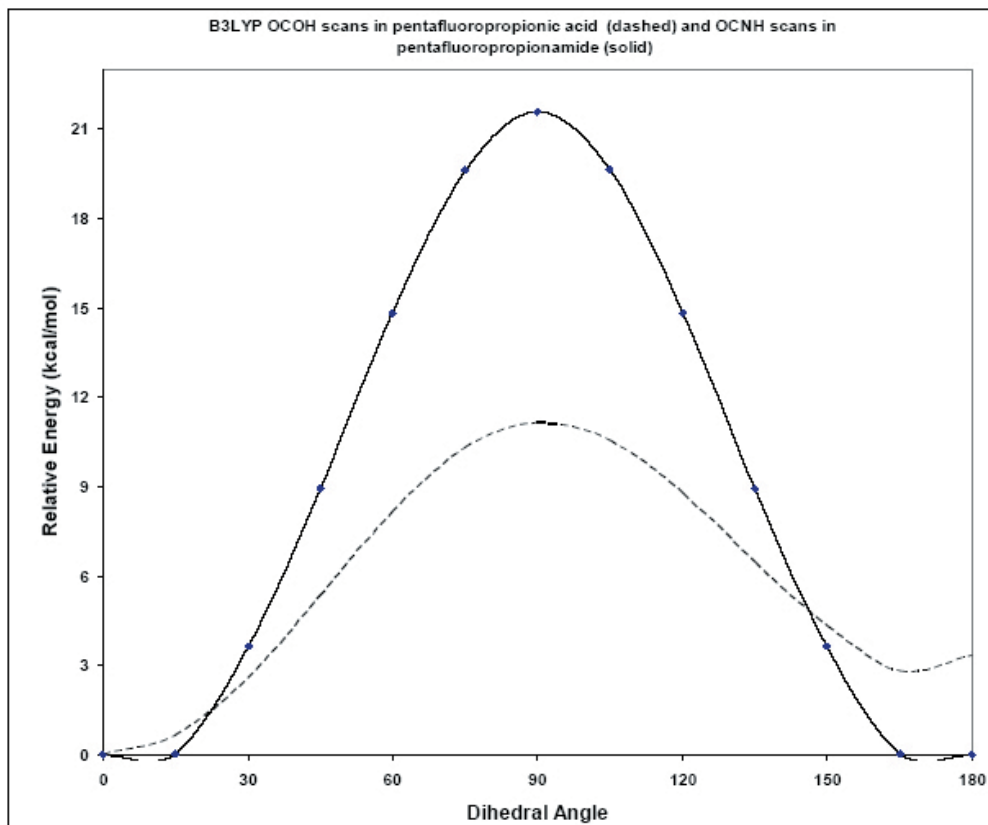

Figure 4. Calculated potential curves for the OCOH or OCNH torsions with FCCC = 180 and CCCO = 0 degrees of pentafluoropropionic acid (dshed) and pentafluoropropionamide (solid) at B3LYP/6-311+G** level of theory.

ternal rotations in each molecule. The symmetric CF3 torsional barrier in both molecules was predicted to be about 7 kcal/mol (Figure 2). The CCCO potential energy curve for pentafluoropropionic acid was consistent with two clear minima that correspond to the planar *cis* and the non-planar *gauche* conformations of the molecule (Figure 3). The *trans* (C=O is *trans* to C-C bond) form was predicted at the DFT and the MP2 levels of theory to have a negative frequency as a maximum in the potential energy curve of the acid (Figure 3). For pentafluoropropionamide only the *gauche* conformer was predicted to have a real frequency as the only true minimum in the potential energy curve of the amide (Figure 3). Furthermore, the OCOH and the OCNH barriers were predicted to be about 11 and 21 kcal/mol in the acid and the amide, respectively (Figure 4).

From the theoretical study, a decrease in the total dipole moment of about 0.05 Debye was calculated as going from the low energy *gauche* conformer to the high energy *cis* form of pentafluoropropionic acid (Table 1). Such a negligeable change in the dipole moment was a clear indication that steric forces play more important role than dipolar interactions as one would expect in governing the conformational equilibria of the acid. The equilibrium constant for the *Cis ↔ Gauche* conformational interconversion in pentafluoropropionic acid was estimated from the change in the Gibb's free-energy as follows:

$$K^o = \frac{g_P}{g_R} e^{-\frac{\Delta G^o}{RT}}$$

where, the *g*-s are symmetry weights and *P* and *R* are the low and the high energy conformers. The degeneracy *g* equals 1 and 2 in the case of the planar and the non-planar forms, respectively, RT at 298.15 K is 592.488 cal/mol and $\Delta G^o = G^o(P) - G^o(R)$. Two conformers were predicted to have noticeable stabilty at ambient tepmerature, namely *cis* and *gauche* as shown in Table 3. From the calculations at the B3LYP/6-311+G** level of theory the G_{cis} is -764.807779 H and the G_{trans} is -764.808188 H, that gives rise to a calculated Gibb's free energy difference, ΔG, of 0.257 kcal/mol (1.075 kJ/mol) and an equilibrium constant *k* of 0.324 at 298.15 K that corresponds to an equilibrium mixture of about 24% *cis* and 76% *gauche* of pentafluoropropionic acid at 298.15 K.

We calculated the vibrational wavenumbers for the stable conformers of pentafluoropropionic acid and its amide at the DFT-B3LYP/6-311+G** level and then computed the potential energy distribution PED among the symmetry coordinates of the normal modes of the molecule (Tables 8-10). We tried to provide reliable vibrational assignments for the normal modes on the basis of the calculated PED values, infrared line intensity, Raman activities and comparison with mid-infrared spectra of the molecules obtained from (Link: http://www.aist. go.jp/RIODB/SDBS). Additionally, the infrared and Raman spectra of pentafluoropropionic acid were compared to the previously reported experimental data by Crowder [8]. As shown from Tables 6 and 7, many modes especially bending ones were predicted to mix extensively with other vibrations. Hence, in the following discussion, we will concentrate only on the assignments of the intense spectral features that characterize the molecules in their low energy conformations.

Pentafluoropropionic acid in its *cis* conformation has C_s symmetry and the 27 vibrational modes span the irreducible representations: 17 A′ and 10 A″. The A′ modes should be polarized whereas the A″ modes are depolarized in the Raman spectra of the liquid. The *gauche* conformer of the acid has C_1 symmetry and the vibrational modes span the irreducible representation: 27 A and all the modes should be polarized in the Raman spectra of the liquid. For pentafluoropropionamide in its *gauche* conformation the 30 vibrational modes span the A irreducible representation.

A sharp band observed band at 3579 cm⁻¹ (100% PED) in the gaseous-phase IR spectrum that was completely absent in the spectrum of the liquid-phase was idenfied as the O-H stretch of the free pentafluoropropionic acid [8]. The broad and intense band centered at 3180 cm⁻¹ in the same spectrum is the corresponding stretching mode as a result of the hydrogen bonding in the dimmer (Figure 5). The C-O, the five C-F and the two C-C stretching modes and many of the skeletal bending modes were all calculated to have a noticeable degree of mixing with other vibrations as shown in Table 8. However, the C=O stretching mode was calculated to have 89% PED value and can be assigned with confidence to the observed very intense band at 1778 cm⁻¹ in the infrared spectrum of liquid pentafluoropropionnic acid (Figure 5 and Table 8). The two CF₃ antisymmetric stretching modes were predicted to have about 50% PED values and can be assigned to the observed bands at 1200 and 1165 cm⁻¹ in the same spectrum. The CF₃ deformation with 59% S_{10} in the Raman spectrum of the acid can be assigned to observed line at 540 cm⁻¹ (Table 8). In the low frequency spectral region of pentafluoropropionic acid the CF₃ (77% S_{27}) and the OCO (78% S_{26}) torsions were

Table 4. Calculated potential constants (kcal/mol) for the asymmetric CCCO torsion in pentafluoropropionic acid and its amide at B3LYP/6-311+G** and MP2/6-311+G**levels of theory.

Potential constants	Pentafluoropropionic acid		Pentafluoropropionamide	
	B3LYP	**MP2**	**B3LYP**	**MP2**
V_0	0.363	0.333	1.134	1.241
V_1	0.188	0.180	2.218	2.384
V_2	-0.672	-0.740	-2.009	-2.187
V_3	0.462	0.540	-0.127	-0.026
V_4	-0.009	0.230	-0.319	-0.014
V_5	0.048	0.088	0.047	0.063
V_6	0.035	0.019	-0.048	-0.056

Table 5. Internal coordinate definitions[a] for pentafluoropropionamide.

No.	Coordinate	Definition	No.	Coordinate	Definition
1	C_1-C_2 stretch	R_1	18	$C_3C_1F_9$ bend	γ_1
2	C_1-C_3 stretch	R_2	19	$C_3C_1F_{10}$ bend	γ_2
3	C_3-O_4 stretch	S	20	$F_9C_1F_{10}$ bend	δ
4	C_3-N_5 stretch	P	21	$C_1C_2F_6$ bend	α_1
5	C_2-F_6 stretch	Q_1	22	$C_1C_2F_7$ bend	α_2
6	C_2-F_7 stretch	Q_2	23	$C_1C_2F_8$ bend	α_3
7	C_2-F_8 stretch	Q_3	24	$F_7C_2F_8$ bend	β_1
8	C_1-F_9 stretch	A_1	25	$F_6C_2F_7$ bend	β_2
9	C_1-F_{10} stretch	A_2	26	$F_6C_2F_8$ bend	β_3
10	N_5-H_{11} stretch	T_1	27	$H_{11}N_5H_{12}$ bend	κ_1
11	N_5-H_{12} stretch	T_2	28	$C_3N_5H_{11}$ bend	κ_2
12	$C_2C_1C_3$ bend	ε	29	$C_3N_5H_{12}$ bend	κ_3
13	$C_1C_3O_4$ bend	θ	30	$N_5C_3C_1O_4$ wag	η
14	$C_1C_3N_5$ bend	φ	31	$(O_4C_3N_5H_{11} + O_4C_3N_5H_{12})$ torsion	χ_1
15	$N_5C_3O_4$ bend	ω	32	$(O_4C_3N_5H_{11} - O_4C_3N_5H_{12})$ torsion	χ_2
16	$C_2C_1F_9$ bend	σ_1	33	$C_2C_1C_3O_4$ (OCN) torsion $C_2C_1C_3N_5$ $F_7C_2C_1C_3$ $F_8C_2C_1C_3$	τ_1
17	$C_2C_1F_{10}$ bend	σ_2	34	$F_6C_2C_1C_3$ (CF$_3$) torsion	τ_2

[a] For atom denotation see Figure 1.

Table 6. Symmetry coordinates for pentafluoropropionic acid.

Species	Description	Symmetry coordinate[a]
A′	OH stretch	$S_1 = T$
	C-O stretch	$S_2 = P$
	CCC antisymmetric stretch	$S_3 = R_1 - R_2$
	CCC symmetric stretch	$S_4 = R_1 + R_2$
	C=O stretch	$S_5 = S$
	CF₂ symmetric stretch	$S_6 = A_1 + A_2$
	CF₃ antisymmetric stretch	$S_7 = 2Q_1 - Q_2 - Q_3$
	CF₃ symmetric stretch	$S_8 = Q_1 + Q_2 + Q_3$
	CF₂ deformation (scissor)	$S_9 = [(6)^{1/2}+2]\delta - [(6)^{1/2}-2]\varepsilon - \sigma_1 - \sigma_2 - \gamma_1 - \gamma_2$
	CF₃ antisymmetric deformation	$S_{10} = 2\beta_1 - \beta_2 - \beta_3$
	CF₃ symmetric deformation	$S_{11} = \beta_1 + \beta_2 + \beta_3 - \alpha_1 - \alpha_2 - \alpha_3$
	CF₂ wag	$S_{12} = \sigma_1 + \sigma_2 - \gamma_1 - \gamma_2$
	CF₃ rock	$S_{13} = 2\alpha_1 - \alpha_2 - \alpha_3$
	CCC bend	$S_{14} = [(6)^{1/2}-2]\delta - [(6)^{1/2}+2]\varepsilon + \sigma_1 + \sigma_2 + \gamma_1 + \gamma_2$
	CFO deformation	$S_{15} = \theta + \varphi - 2\omega$
	CFO rock	$S_{16} = \theta - \varphi$
	COH bend	$S_{17} = \kappa$
A″	CF₂ antisymmetric stretch	$S_{18} = A_1 - A_2$
	CF₃ antisymmetric stretch	$S_{19} = Q_2 - Q_3$
	CF₃ antisymmetric deformation	$S_{20} = \beta_2 - \beta_3$
	CF₂ twist	$S_{21} = \sigma_1 - \sigma_2 - \gamma_1 + \gamma_2$
	CF₂ rock	$S_{22} = \sigma_1 - \sigma_2 + \gamma_1 - \gamma_2$
	CF₃ rock	$S_{23} = \alpha_2 - \alpha_3$
	CFO wag	$S_{24} = \eta$
	COH bend	$S_{25} = \chi$
	CFO torsion	$S_{26} = \tau_1$
	CF₃ torsion	$S_{27} = \tau_2$

[a] Not normalized

Table 7. Symmetry coordinates for *gauche* pentafluoropropionamide.

Species	Description	Symmetry coordinate[a]
A	NH$_2$ antisymmetric stretch	$S_1 = T_1 - T_2$
	NH$_2$ symmetric stretch	$S_2 = T_1 + T_2$
	C-N stretch	$S_3 = P$
	CCC antisymmetric stretch	$S_4 = R_1 - R_2$
	CCC symmetric stretch	$S_5 = R_1 + R_2$
	C = O stretch	$S_6 = S$
	CF$_2$ symmetric stretch	$S_7 = A_1 + A_2$
	CF$_3$ antisymmetric stretch	$S_8 = 2Q_1 - Q_2 + Q_3$
	CF$_3$ symmetric stretch	$S_9 = Q_1 + Q_2 + Q_3$
	CF$_2$ deformation (scissor)	$S_{10} = [(6)^{1/2}+2]\delta - [(6)^{1/2}-2]\varepsilon - \sigma_1 - \sigma_2 - \gamma_1 - \gamma_2$
	CF$_3$ antisymmetric deformation	$S_{11} = 2\beta_1 - \beta_2 - \beta_3$
	CF$_3$ symmetric deformation	$S_{12} = \beta_1 + \beta_2 + \beta_3 - \alpha_1 - \alpha_2 - \alpha_3$
	CF$_2$ wag	$S_{13} = \sigma_1 + \sigma_2 - \gamma_1 - \gamma_2$
	CF$_3$ rock	$S_{14} = 2\alpha_1 - \alpha_2 - \alpha_3$
	CCC bend	$S_{15} = [(6)^{1/2}-2]\delta - [(6)^{1/2}+2]\varepsilon + \sigma_1 + \sigma_2 + \gamma_1 + \gamma_2$
	OCN deformation	$S_{16} = \theta + \varphi - 2\omega$
	OCN rock	$S_{17} = \theta - \varphi$
	NH$_2$ deformation	$S_{18} = 2\kappa_1 - \kappa_2 - \kappa_3$
	NH$_2$ rock	$S_{19} = \kappa_2 - \kappa_3$
	CF$_2$ antisymmetric stretch	$S_{20} = A_1 - A_2$
	CF$_3$ antisymmetric stretch	$S_{21} = Q_2 - Q_3$
	CF$_3$ antisymmetric deformation	$S_{22} = \beta_2 - \beta_3$
	CF$_2$ twist	$S_{23} = \sigma_1 - \sigma_2 - \gamma_1 + \gamma_2$
	CF$_2$ rock	$S_{24} = \sigma_1 - \sigma_2 + \gamma_1 - \gamma_2$
	CF$_3$ rock	$S_{25} = \alpha_2 - \alpha_3$
	OCN wag	$S_{26} = \eta$
	NH$_2$ wag	$S_{27} = \chi_1$
	NH$_2$ twist	$S_{28} = \chi_2$
	OCN torsion	$S_{29} = \tau_1$
	CF$_3$ torsion	$S_{30} = \tau_2$

[a] Not normalized

Table 8. Calculated vibrational frequencies (cm^{-1}) at B3LYP/6-311+G** level of theory of *gauche* pentafluropropionic acid.

Sym.	No.	Freq.	IR Int.	Raman act.	Depol. ratio	Obs^b IR	Obs^b Raman	Obs/Calc	PED
A	ν_1	3750	107.44	103.06	0.24	3579		0.9	100% S$_1$ (OH str.)
	ν_2	1860	329.49	13.19	0.22	1778		0.96	89% S$_5$ (C=O str.)
	ν_3	1379	42.18	3.42	0.69	1337	1343	0.97	30% S$_{17}$ (COH bend), 28% S$_2$ (C-O str.), 16% S$_{15}$ (OCO def.), 12% S$_4$ (CCC sym. str.)
	ν_4	1304	94.74	2.80	0.50	1270		0.97	23% S$_3$ (CCC antisym. str.), 19% S$_8$ (CF$_3$ sym. str.), 17% S$_{11}$ (CF$_3$ sym. def.), 13% S$_4$ (CCC sym. str.), 10% S$_6$ (CF$_2$ sym. str.)
	ν_5	1221	90.51	3.34	0.75	1228	1223	1.01	24% S$_{17}$ (COH bend), 21% S$_7$ (CF$_3$ antisym. str.), 10% S$_{18}$ (CF$_2$ antisym. str.)
	ν_6	1198	355.14	0.32	0.71	1200		1.00	48% S$_{19}$ (CF$_3$ antisym. str.), 20% S$_7$ (CF$_3$ antisym. str.), 12% S$_{18}$ (CF$_2$ antisym. str.)
	ν_7	1183	168.24	1.59	0.65	1176		0.99	31% S$_7$ (CF$_3$ antisym. str.), 27% S$_{19}$ (CF$_3$ antisym. str.)
	ν_8	1155	218.45	2.47	0.59	1165		1.01	49% S$_{18}$ (CF$_2$ antisym. str.), 18% S$_{17}$ (COH bend), 14% S$_2$ (C-O str.),
	ν_9	1138	247.88	0.39	0.44	1135		1.00	36% S$_6$ (CF$_2$ sym. str.), 26% S$_2$ (C-O str.)
	ν_{10}	1020	133.66	0.65	0.73	1034	1034	1.01	28% S$_{12}$ (CF$_2$ wag), 26% S$_8$ (CF$_3$ sym. str.), 17% S$_3$ (CCC antisym. str.)
	ν_{11}	774	25.51	2.40	0.09	800		1.02	40% S$_{24}$ (OCO wag), 16% S$_6$ (CF$_2$ sym. str.), 13% S$_{25}$ (COH bend), 10% S$_{14}$ (CCC bend)
	ν_{12}	759	3.29	8.69	0.03	782	780	1.03	42% S$_8$ (CF$_3$ sym. str.), 26% S$_{11}$ (CF$_3$ sym. def.),13% S$_4$ (CCC sym. str.)
	ν_{13}	680	99.34	2.51	0.38	705	698	1.03	37% S$_{15}$ (OCO def.), 11% S$_{11}$ (CF$_3$ sym. def.), 10% S$_2$ (C-O str.), 10% S$_{12}$ (CF$_2$ wag)
	ν_{14}	629	76.56	0.90	0.70	620		0.99	36% S$_{25}$ (COH bend), 19% S$_9$ (CF$_2$ scissor), 11% S$_6$ (CF$_2$ sym. str.)
	ν_{15}	597	15.23	1.80	0.70	582		0.97	23% S$_{20}$ (CF$_3$ antisym. def.), 17% S$_{22}$ (CF$_2$ wag), 15% S$_{19}$ (CF$_3$ antisym. str.), 13% S$_{23}$ (CF3 rock), 12% S$_{23}$ (COH bend), 11% S$_{18}$ (CF$_2$ antisym. str.)

Table 8 continued.   Calculated vibrational frequencies (cm⁻¹) at B3LYP/6-311+G** level of theory of *gauche* pentafluropropionic acid.

Sym.	No.	Freq.	IR Int.	Raman act.	Depol. ratio	Obs[b]		Obs/Calc	PED
						IR	Raman		
A	ν_{16}	547	24.14	0.82	0.64				29% S_{25} (COH bend), 17% S_{20} (CF$_3$ antisym. def.), 13% S_9 (CF$_2$ scissor)
	ν_{17}	535	7.81	0.85	0.64	543	540	1.01	59% S_{10} (CF$_3$ antisym. def.), 14% S_9 (CF$_2$ scissor), 11% S_7 (CF$_3$ antisym. str.)
	ν_{18}	484	4.58	0.64	0.55				23% S_{20} (CF$_3$ antisym. def.), 19% S_{16} (CFO rock), 14% S_{22} (CF$_2$ rock), 10% S_{10} (CF$_3$ antisym. def.)
	ν_{19}	377	0.41	1.49	0.57	388		1.03	22% S_{21} (CF$_2$ twist), 16% S_{23} (CF$_3$ rock), 15% S_9 (CF$_2$ scissor), 15% S_{20} (CF$_3$ antisym. def.)
	ν_{20}	367	0.98	2.54	0.39		379	1.03	29% S_4 (CCC sym. str.), 14% S_{15} (OCO def.), 12% S_{12} (CF$_2$ wag), 10% S_{16} (OCO rock)
	ν_{21}	349	0.13	1.28	0.59		354	1.01	20% S_3 (CCC antisym. str.), 14% S_{13} (CF$_3$ rock), 14% S_{11} (CF$_3$ sym. def.), 13% S_{12} (CF$_2$ wag), 13% S_9 (CF$_2$ scissor)
	ν_{22}	284	1.11	0.82	0.54	292	290	1.02	46% S_{13} (CF$_3$ rock), 23% S_{12} (CF$_2$ wag)
	ν_{23}	245	1.43	0.25	0.75				45% S_{21} (CF$_2$ twist), 32% S_{16} (OCO rock), 13% S_{22} (CF$_2$ rock)
	ν_{24}	215	1.56	0.01	0.72				49% S_{23} (CF$_3$ rock), 36% S_{22} (CF$_2$ rock), 12% S_{21} (CF$_2$ twist)
	ν_{25}	144	1.30	0.38	0.66				68% S_{14} (CCC bend), 15% S_{13} (CF$_3$ rock)
	ν_{26}	59	0.24	0.23	0.75				77% S_{27} (CF$_3$ torsion), 23% S_{26} (OCO torsion)
	ν_{27}	28	1.44	0.90	0.75				78% S_{26} (OCO torsion), 23% S_{27} (CF$_3$ torsion)

[a] IR intensities and Raman activities are calculated in km mol⁻¹ and Å⁴ amu⁻¹ respectively.

[b] Observed wavenumbers are taken from infrared data of the liquid in reference [5]. Italic denotes observed infrared wavenumbers of the gas obtained from reference [5].

Table 9. Calculated vibrational frequencies (cm^{-1}) at B3LYP/6-311+G** level of theory of *cis* pentafluropropionic acid.

Sym.	No.	Freq.	IR Int.	Raman act.	Depol. ratio	PED
A′	v_1	3750	108.82	110.05	0.25	100% S_1 (OH str.)
	v_2	1851	310.13	10.60	0.24	89% S_5 (C=O str.)
	v_3	1385	61.30	3.06	0.68	29% S_2 (C-O str.), 28% S_{17} (COH bend), 17% S_{15} (CFO def.), 11% S_3 (CCC antisym. str.)
	v_4	1332	69.58	2.58	0.56	27% S_3 (CCC antisym. str.), 19% S_8 (CF₃ sym. str), 17% S_{11} (CF₃ sym. def.), 14% S_4 (CCC sym. str.)
	v_5	1200	71.58	5.00	0.74	37% S_{17} (COH bend), 14% S_6 (CF₂ sym. str.), 13% S_7 (CF₃ antisym. str.)
	v_6	1193	236.85	1.67	0.26	52% S_7 (CF₃ antisym. str.), 18% S_{17} (COH bend), 10% S_2 (C-O str.)
	v_7	1144	142.25	0.33	0.41	34% S_6 (CF₂ sym. str.), 17% S_2 (C-O str.), 11% S_7 (CF₃ antisym. str.), 10% S_8 (CF₃ sym. str.)
	v_8	1017	286.45	0.38	0.28	25% S_2 (C-O str.), 24% S_8 (CF₃ sym. str.), 19% S_{12} (CF₂ wag), 14% S_3 (CCC antisym. str.)
	v_9	760	1.77	9.90	0.00	40% S_8 (CF₃ sym. str.), 24% S_{11} (CF₃ sym. def.), 15% S_4 (CCC sym. str.)
	v_{10}	678	123.71	2.96	0.20	37% S_{15} (CFO def.), 18% S_{11} (CF₃ sym. def.), 11% S_{12} (CF₂ wag)
	v_{11}	651	7.49	1.36	0.62	23% S_6 (CF₂ sym. str.), 17% S_9 (CF₂ scissor), 13% S_{15} (CFO def.), 10% S_{14} (CCC bend)
	v_{12}	529	8.14	0.93	0.70	66% S_{10} (CF₃ antisym. def.), 12% S_7 (CF₃ antisym. str.), 12% S_9 (CF₂ scissor)
	v_{13}	412	0.41	1.96	0.66	45% S_9 (CF₂ scissor), 26% S_{16} (CFO rock)
	v_{14}	353	0.43	1.65	0.66	24% S_{12} (CF₂ wag), 23% S_3 (CCC antisym. Str.), 15% S_{13} (CF₃ rock), 12% S_{10} (CF₃ antisym. def.)
	v_{15}	329	0.28	1.66	0.25	43% S_4 (CCC sym. str.), 22% S_{11} (CF₃ sym. def.), 12% S_{16} (CFO rock)
	v_{16}	278	5.52	0.04	0.47	36% S_{16} (C-C str.), 26% S_{15} (C-O str.), 19% S_4 (C-C sym. str.), 13% S_{14} (OCO def.)
	v_{17}	150	0.16	0.02	0.21	68% S_{14} (CCC bend), 17% S_{13} (CF₃ rock), 14% S_{16} (CFO rock)
A″	v_{18}	1206	329.35	0.64	0.75	79% S_{19} (CF₃ antisym. str.), 10% S_{20} (CF₃ antisym. def.)
	v_{19}	1131	167.43	1.88	0.75	81% S_{18} (CF₂ antisym. str.)
	v_{20}	784	38.11	0.08	0.75	60% S_{24} (CFO wag), 14% S_{25} (COH bend), 11% S_{22} (CF₂ rock)
	v_{21}	593	47.18	1.36	0.75	47% S_{25} (COH bend), 20% S_{20} (CF₃ antisym.def.), 11% S_{19} (CF₃ antisym. str.)
	v_{22}	561	57.77	1.65	0.75	39% S_{25} (COH bend), 32% S_{20} (CF₃ antisym. def), 10% S_{19} (CF₃ antisym. str.)
	v_{23}	411	0.04	0.59	0.75	38% S_{20} (CF₃ antisym. def.), 23% S_{23} (CF₃ rock), 17% S_{22} (CF₂ rock), 12% S_{21} (CF₂ twist)
	v_{24}	248	0.23	1.08	0.75	68% S_{21} (CF₂ twist), 21% S_{24} (CFO wag)
	v_{25}	212	1.53	0.25	0.75	50% S_{23} (CF₃ rock), 41% S_{22} (CF₂ rock)
	v_{26}	79	0.01	0.14	0.75	96% S_{27} (CF₃ torsion)
	v_{27}	19	1.69	0.95	0.75	93% S_{26} (CFO torsion)

[a]IR intensities and Raman activities are calculated in km mol^{-1} and Å^4 amu^{-1} respectively.

Table 10. Calculated vibrational frequencies (cm^{-1}) at B3LYP/6-311+G** level of theory of *gauche* pentafluropropionamide.

Sym.	No.	Freq.	IR Int.	Raman act.	Depol. ratio	Obs[b] IR	Obs/ Calc	PED
A	ν_1	3719	84.57	39.66	0.75	3385	0.91	99% S_1 (NH$_2$ antisym. str.)
	ν_2	3589	70.50	122.00	0.11	3228	0.90	99% S_2 (NH$_2$ sym. str.)
	ν_3	1809	395.14	12.31	0.32	1707	0.94	81% S_6 (C=O str.), 10% S_3 (C-N str.)
	ν_4	1619	92.67	2.10	0.60	1630	1.01	89% S_{18} (NH$_2$ def.)
	ν_5	1376	56.11	8.24	0.35	1436	1.04	38% S_3 (C-N str.), 15% S_{16} (ONC def.), 12% S_{19} (NH$_2$ rock), 11% S_5 (CCC sym. str.)
	ν_6	1306	112.82	2.58	0.71	1226	1.02	26% S_4 (CCC antisym. str.), 22% S_9 (CF$_3$ sym. str.), 19% S_{12} (CF$_3$ sym. def.), 14% S_5 (CCC sym. str.)
	ν_7	1211	254.35	1.47	0.54	1219	1.01	38% S_8 (CF$_3$ antisym. str.), 36% S_{21} (CF$_3$ antisym. str.)
	ν_8	1185	65.82	1.54	0.70	1211	1.02	34% S_{21} (CF$_3$ antisym. str.), 17% S_8 (CF$_3$ antisym. str.), 10% S_7 (CF$_2$ sym. str.)
	ν_9	1164	372.75	0.25	0.38	1178	1.01	34% S_{20} (CF$_2$ antisym. str.), 18% S_7 (CF$_2$ sym. str.), 18% S_8 (CF$_3$ antisym. str.)
	ν_{10}	1120	1500.74	1.06	0.50	1163	1.04	34% S_{20} (CF$_2$ antisym. str.), 20% S_7 (CF$_2$ sym. str.)
	ν_{11}	1097	13.32	7.81	0.24	1111	1.01	60% S_{19} (NH$_2$ rock), 18% S_3 (C-N str.), 10% S_6 (C=O str.)
	ν_{12}	1016	158.14	0.36	0.73	1036	1.02	26% S_9 (CF$_3$ sym. str.), 25% S_{13} (CF$_2$ wag), 17% S_4 (CCC antisym. str.)
	ν_{13}	765	3.69	0.46	0.29	798	1.04	45% S_{26} (OCN wag), 17% S_{27} (NH$_2$ wag), 10% S_7 (CF$_2$ sym. str.)
	ν_{14}	753	8.81	7.99	0.02	769	1.02	42% S_9 (CF$_3$ sym. str.), 28% S_{12} (CF$_3$ sym. def.), 13% S_5 (CCC sym. str.)
	ν_{15}	638	43.29	2.00	0.26	672	1.05	37% S_{16} (ONC def.), 11% S_{19} (NH$_2$ rock), 10% S_{13} (CF$_2$ wag)
	ν_{16}	625	16.98	0.86	0.24	~620	0.99	34% S_{27} (NH$_2$ wag), 17% S_{10} (CF$_2$ def. (scissor)),16% S_7 (CF$_2$ sym. str.)
	ν_{17}	592	1.26	1.84	0.69			26% S_{22} (CF$_3$ antisym. def.), 16% S_{21} (CF$_3$ antisym. str.), 12% S_{24} (CF$_2$ rock.), 12% S_{27} (NH$_2$ wag), 11% S_{20} (CF$_2$ antisym. str.), 11% S_{25} (CF$_3$ rock)
	ν_{18}	549	1.66	0.43	0.27	557	1.01	27% S_{27} (NH$_2$ wag), 18% S_{26} (OCN wag), 17% S_{22} (CF$_3$ antisym. def.), 14% S_{10} (CF$_2$ def. (scissor))
	ν_{19}	527	7.34	0.78	0.75			65% S_{11} (CF$_3$ antisym. def.), 10% S_8 (CF$_3$ antisym. str.)
	ν_{20}	480	3.62	0.95	0.75			24% S_{22} (CF$_3$ antisym. def.), 18% S_{17} (ONC rock), 14% S_{10} (CF$_2$ def. (scissor)), 14% S_{24} (CF$_2$ rock)
	ν_{21}	384	1.06	2.09	0.48			18% S_{23} (CF$_2$ twist), 17% S_{10} (CF$_2$ def. (scissor)), 14% S_5 (CCC sym. str.), 13% S_{22} (CF$_3$ antisym. def.), 12% S_{25} (CF$_3$ rock)
	ν_{22}	362	89.02	1.04	0.47			40% S_{28} (NH$_2$ twist), 11% S_{16} (ONC def.),10% S_{13} (CF$_2$ wag)

Table 10 continued.

v_{23}	359	105.37	0.89	0.47	53% S$_{28}$ (NH$_2$ twist), 10% S$_5$ (CCC sym. str.), 10% S$_{17}$ (ONC rock)
v_{24}	347	12.98	1.23	0.53	16% S$_4$ (CCC antisym. str.), 15% S$_{10}$ (CF$_2$ def. (scissor)), 13% S$_{14}$ (CF$_3$ rock), 12% S$_{12}$ (CF$_3$ sym. def.), 10% S$_{13}$ (CF$_2$ wag)
v_{25}	289	5.77	0.69	0.48	45% S$_{14}$ (CF$_3$ rock), 18% S$_{13}$ (CF$_2$ wag), 10% S$_5$ (CCC sym. str.),10%S$_{17}$ (ONC rock)
v_{26}	260	2.82	0.44	0.70	45% S$_{23}$ (CF$_2$ twist), 22% S$_{17}$ (ONC rock), 16% S$_{24}$ (CF2 rock)
v_{27}	213	2.73	0.04	0.68	49% S$_{25}$ (CF$_3$ rock), 34% S$_{24}$ (CF$_2$ rock), 14% S$_{23}$ (CF$_2$ twist)
v_{28}	145	0.12	0.37	0.66	70% S$_{15}$ (CCC bend), 15% S$_{14}$ (CF$_3$ rock), 8% S$_{26}$ (OCN wag)
v_{29}	62	1.90	0.22	0.75	83% S$_{30}$ (CF$_3$ torsion), 16% S$_{29}$ (CFO torsion)
v_{30}	35	7.95	1.73	0.75	84% S$_{29}$ (CFO torsion), 16% S$_{30}$ (CF$_3$ torsion)

[a] IR intensities and Raman activities are calculated in km mol^{-1} and Å^4 amu^{-1} respectively.
[b] Observed wavenumbers are taken from link: http://www.aist.go.jp/RIODB/SDBS.
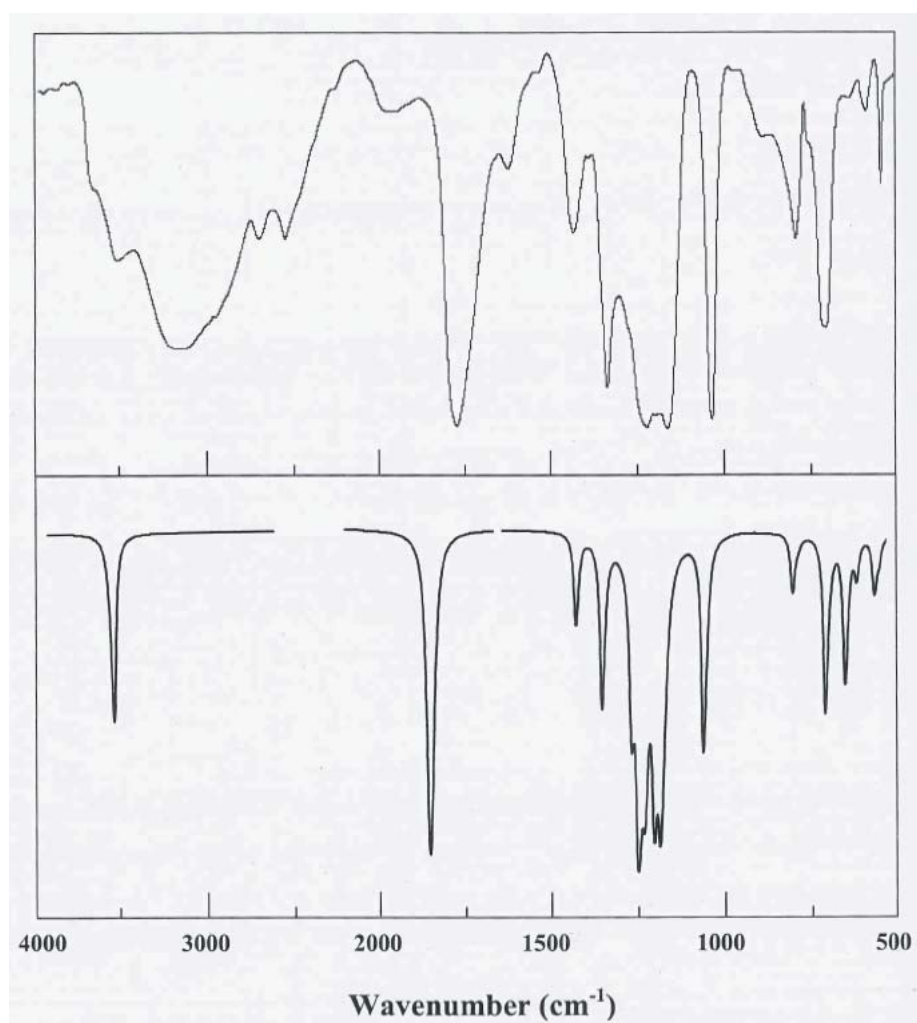

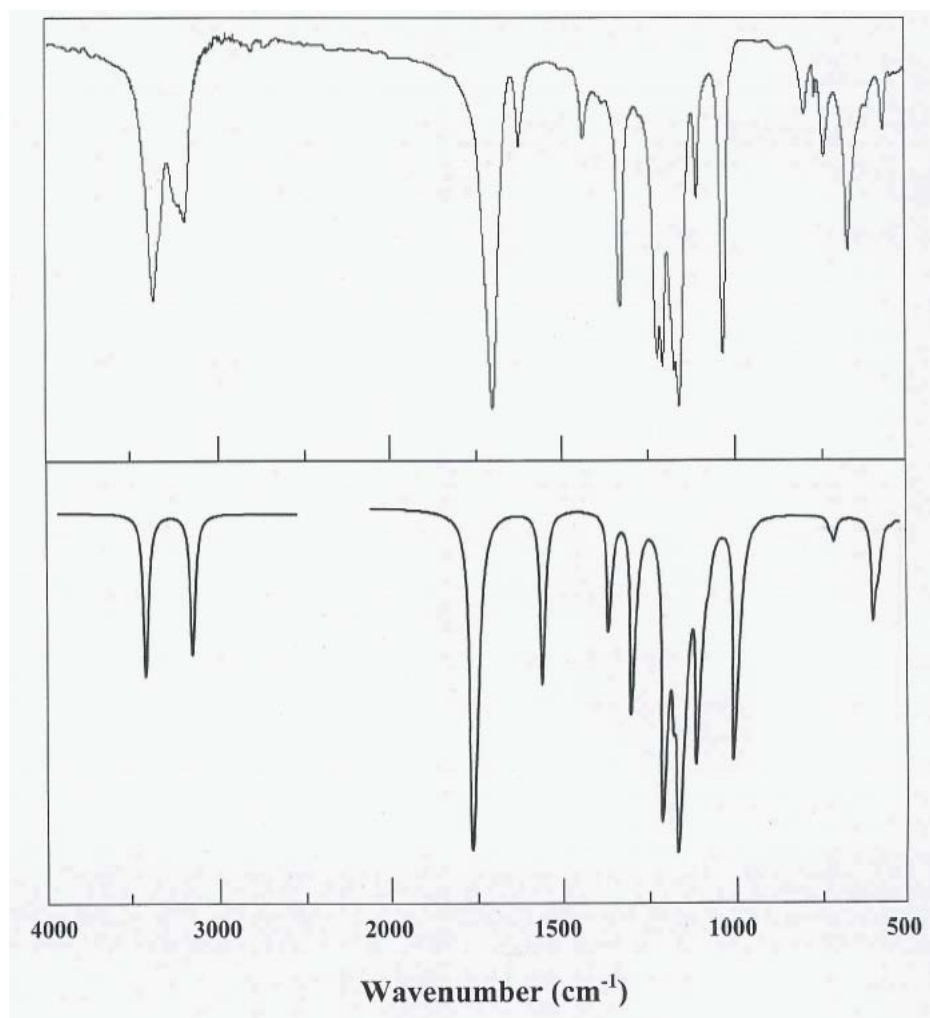Figure 5: Observed (upper) and calculated (lower) infrared spectra of 2,2,3,3,3-pentafluoropropionic acid.

Figure 6: Observed (upper) and calculated (lower) infrared spectra of 2,2,3,3,3-pentafluoropropionamide.

predicted at 59 and 28 cm^{-1} as shown in Table 8.

For pentafluoroproionamide, the two observed intense bands at 3385 cm^{-1} (99% PED) and 3228 cm^{-1} (99% PED) in the IR spectrum are assigned to the two NH_2 stretching modes (Figure 6 and Table 10). The C=O stretching mode was calculated to have 81% PED value and can be assigned with confidence to the observed the intense band at 1707 cm^{-1} in the infrared spectrum of liquid pentafluoropropionamide (Figure 5 and Table 8). Six characteristic intense bands were observed at 1436, 1226, 1211, 1178, 1163 and 1036 cm^{-1} in the infrared spectrum of the pentafluororopionamide that correspond to the CCC and the C-F stretching modes and all were calculated to have a noticeable degree of mixing with other vibrations as shown in Table 10. The lowest modes in the spectra of pentafluoropropionamide are the CF_3 (83% S_{30}) and OCN (84% S_{29}) torsions. These two torsions were predicted at 62 and 35 cm^{-1} in the spectrum

of the amide as shown in Table 10.

Conclusions

The conformational equilibria of pentafluoropropionic acid and pentafluoropropionamide were investigated by DFT-B3LYP/6-311+G** and *ab initio* MP2/6-311+G** levels of theory. The acid was predicted at both levels of theory to exist in an equilibrium mixture of about 76 % *gauche* and 24% *cis* conformations at 298.15 K, while the amide to exist only in the *gauche* conformation. Reliable vibrational assignments for the normal modes of each molecule in its low energy conformation were provided on the basis of normal coordinate calculations and comparison between theoretical and experimental infrared and Raman spectra of the molecules.

Acknowledgements

References

1. W. Forner and H. M. Badawi, *J. Mol. Model.*, **6**, 99 (2000).
2. W. Forner and H. M. Badawi, *J. Mol. Struct.*, **550**, 43 (2000).
3. H. M. Badawi and W. Forner, *J. Mol. Struct.*, **595**, 147 (2001).
4. H. M. Badawi and W. Forner, *J. Mol. Struct.(Theochem)*, **545**, 137 (2001).
5. G. A. Crowder, J. Fluorine Chem., **1**, 385 (1972).
6. C. Legrand, B. Dousset, H. Tronel, F. Belleville, P. Nabet, *J. Chromatogr., B: Biomed.*, **663**, 187 (1995).
7. H. Hori, Y. Takano, K. Koike, S. Kutsuna, H. Einaga, T. Ibusuki, *Appl. Catal., B: Environ.*, **46**, 333 (2003).
8. A. Marand, D. Karlsson, M. Dalene, G. Skarping, *Analyst*, **129**, 522 (2004).
9. D. A. Ellis, K. A. Denkenberger, T. E. Burrow, S. A. Mabury, *J. Phys. Chem. A*, **108**, 10099 (2004).
10. A. Rohde, W. Urland, *Inorg. Chim Acta*, **359**, 2448 (2006).
11. R. J. Lontz, *J. Chem. Phys.*, **45**, 1339 (1966).
12. G. R. Wilkinson, *Anal. Lett.*, **3**, 289 (1970).
13. M. S. Bryant, P. L. Skipper, S. R. Tannenbaum, M. Maclure, *Cancer Res.*, **47**, 602 (1987).
14. S. A. Best, J. M. Midgley, W. Huang, D. G. Wat-son, *J. Pharmaceut. Biomed.*, **11**, 323 (1993).
15. S. D. Robinson, A. Sahajpal, D. A. Tocher, *J. Chem. Soc., Dalton Transactions: Inorg. Chem.*, **21**, 3497 (1995).
16. W. G. Stillwell, M. S. Bryant, J. S. Wishnok, *Biomed. Environ. Mass Spectrom.*, **14**, 221 (1987).
17. M. J. Frisch, G. W. Trucks, H. B. Schlegel, G. E. Scuseria, M. A. Robb, J. R. Cheeseman, V. G. Zakrzewski, J. A. Montgomery Jr., R. E. Strat-mann, J. C. Burant, S. Dapprich, J. M. Millam, A. D. Daniels, K. N. Kudin, M. C. Strain, O. Fara-kas, J. Tomasi, V. Barone, M. Cossi, R. Cammi, B. Mennucci, C. Pomelli, C. Adamo, S. Clifford, J. Ochterski, G. A. Petersson, P. Y. Ayala, Q. Cui, K. Morokuma, D. K. Malick, A. D. Rabuck, K. Raghavachari, J. B. Foresman, J. Cioslowski, J. V. Ortiz, A. G. Baboul, B. B. Stefanov, G. Liu, A. Liashenko, P. Piskorz, I. Komaromi, R. Gomperts, R. L. Martin, D. J. Fox, T. Keith, M. A. Al-Laham, C. Y. Peng, A. Nanayakkara, C. Gonzalez, M. Challacombe, P. M. W. Gill, B. Johnson, W. Chen, M. W. Wong, J. L. Andres, M. Head-Gordon, E. S. Replogle, and J. A. Pople, Gaussian 98, Revision A7, Gaussian, Inc., Pitts-burgh PA, 1998. A7, Gaussian, Inc., Pittsburgh PA, 1998.
18. E. B. Wilson, J. C. Decius, and P. C. Cross, Molecular vibrations. McGraw-Hill, New York, 1955.
19. W. Forner, H. M. Badawi, *J. Mol. Model.*, **7**, 288 (2001).
20. G. W. Chantry, in: Anderson A (ed) The Raman Effect, Vol. 1. Mercel Dekker, New York, Chapter 2, (1971).
21. J. R. Durig, G. A. Guirgis and K. A. Krutules, *J. Mol. Struct.*, 328, 97 (1994).

Comparative quantative analysis of sodium, magnesium, potassium and calcium in healthy cuttlefish backbone and non-pathological human elbow bone

Ömer Selim Yıldırım[1], Zafer Okumuş[2], Mehmet Kizilkaya[3], Yüksel Özdemir*[4], Rıdvan Durak[4], Ali Okur[1]

[1]*Atatürk University, Faculty of Medicine, Department of Orthopaedics, 25700, Erzurum-Turkey*
[2]*Atatürk University, Faculty of Veterinary Medicine, Department of Surgery, 25700, Erzurum-Turkey*
[3]*Atatürk University,   Faculty of Medicine, Department o f Anaesthesiology, 25700, Erzurum-Turkey*
[4]*Atatürk University, Faculty o f Arts and Sciences, Department of Physics, 25240, Erzurum-Turkey*

Abstract

Energy dispersive X-ray fluorescence techniques were used to analyze cuttlefish backbone. The standard addition method was used to determine the concentration of Na, Mg, K and Ca. The experimental setup consisted of a Si(Li) detector with resolution of 160 eV at 5.9 keV and angular ^{55}Fe sources. The data were compared with our previous literature work and discussed in this study.

Keywords*: Trace elements; XRF analysis of biological sample; cuttlefish; orthopaedic*

Résumé

Nous avons utilisé les techniques de fluorescence des rayons X à énergie dispersive pour analyser l'arête principale de la seiche. La méthode de l'ajout dosé a servi à mesurer la concentration de Na, Mg, K et Ca. Le montage expérimental comportait un détecteur Si (Li) avec résolution de 160 eV à 5.9 keV et des sources angulaires de ^{55}Fe. Les données obtenues ont été comparées avec nos données précédentes de la littérature et elles sont discutées dans cette étude.

Introduction

Metallic elements have important roles in various common orthopaedic surgery. Metallic ions, metallo-

proteins such as heme-protein and suoperoxide dismutase (SOD) have a close relationship with knitting bone. It has been of great interest to understand how the fluctuation of the density of Na, Mg, K and Ca can be related to the process of progression of knitting bone. Energy-dispersive X-ray fluorescence (EDXRF) can probably be considered as one of the most useful non-destructive analytical technique for ancient valuable object of archaeological, historical or artistic interest. A major goal for research in biomedical sciences over the last few decades has been the determination of concentrations of various elements in human tissues.

Cuttlefish (*Sepia officinalis L.*) is abundant in the Aegean Sea [1] and its unique backbone provides rigidity to the body whilst doubling as an efficient buoyancy regulation mechanism in the water [2]. In recent years, a large increase in research work related to bio-medical field such as blood, human hair, kidney stones, human teeth and bones have made it desirable to improve the application of EDXRF analysis [3-5]. Several attempts have been made to measure bio-medical samples and ecological samples. Trace elements were measured experimentally [6-9]. Al-Kofahi and Hallak [10] have measured analysis of kidney stones by particle induced x-ray emission (PIXE) and Rutherford backscattering spectroscopy (RBS) techniques. Hua and Yap [11] have reported energy-dispersive XRF analysis of pure element intensities from their oxides using a Cd-109 source. Budak and Karabulut [12] have analyzed malachite or concentrates in the Narman region using x-ray fluorescence. Karabulut *et al.* [13] have analyzed margulpyrite ore concentrates by EDXRF. Ekinci *et al.* [14] have

*Author to whom correspondence should be addressed:
Fax: +90-442-236-09-48
e-mail address: yozdemir25@yahoo.com

analyzed cataract concentrates using EDXRF. Carvalho *et al.* [3] have analyzed human teeth and bones from the chalcolithic period by X-ray spectrometry. Ekinci *et al.* [15] have determined calcium and iodine in gall bladder stone using EDXRF. Okur *et al.* [16, 17] have determined qualitative and quantitative analysis of pathological and non-pathological human bone using radioistope X-ray fluorescence technique.

To our knowledge, the backbone of common cuttlefish as a xenograft has not been tested. In our preliminary experiment [16], the feasibility of the Cuttlefish backbone as a new bone xenograft was investigated, but its compatibility for human with respect to bone mineral composition was not elucidated. EDXRF technique combined with simple procedures of sample preparation such as drying of a few droplets of liquid on filter paper allow measurement of calcium, potassium chlorine, sulfur and phosphorus in blood serum and in cell fluids. EDXRF is ten times more accurate and considerably faster than other analytical methods. Ashes of tissue, serum and bones may be analyzed for heavy elements such as Fe, Zn, Cu, Sr. EDXRF technique further allows detection of electrophoretically separated protein fractions of the serum and pathologic changes.

EDXRF analysis is suitable especially for trace elemental analysis in biomedical science and biological, chemical, geological materials. The most important advantages of the use of EDXRF for the quantitative analysis of bone samples are:

- Simple and fast preparation
- Simultaneous determination of many elements
- The possibility of determination in a wide concentration range from about 1 ppm to 100 %
- The equipment cost is much lower for a conventional wavelength X-ray fluorescence spectrometer, especially when a radioisotope is used instead of X-ray tube.

Bone grafts are extensively used for orthopaedic applications including treatment of fractures and non-unions, replenishment of bone loss resulting from tumor or infection, and cases requiring reconstructive procedures such as fusion or joint replacement [18]. Various bone graft substitutes including auto grafts, allograft, xenografts, polymers, ceramics and some metals have been employed in promotion of the bone union [19-22]. Although utilization of auto graft results in significant success in the bone healing process, there are some disadvantages associated with requiring the patient to undergo a second surgery and increasing therapeutic

costs due to prolonged hospital stay and medicated period [1]. Therefore, use of allograft and xenograft as an alternative to the auto graft has become common practice in orthopedic surgery [23-25]. There are numerous studies dealing with comparison of the biopotency of allograft such as intramembranous bone graft and demineralized bone graft [21-24] and xenografts such as coralline and bovine grafts [26-28] with the auto graft available.

The preliminary data support that the cuttlefish backbone is easy to obtain and mold and has considerable osteoconductive capacity. Cuttlefish backbone graft may be clinically applicable to enhance osteogenesis and osteoconduction. To validate our previous work, we conducted this experiment to determine the feasibility of the backbone of common cuttlefish (*Sepia officinalis L.*), evaluating its compatibility with respect to mineral composition with healthy humans. The results of the present study on similar mineral contents convinced us to pursue the examination of cuttlefish backbone as a new alternative xenograft for longer term studies in rabbits and sheep.

In continuation of our previous study, the objective in the present study was to determine trace element content of the cuttlefish backbone using x-ray fluorescence analysis. This information would be invaluable for evaluating its use in the human orthopaedic use field, particularly cases associated with depletion of bone mass.

Experimental

The geometry of the experimental set-up employed in the present study is as shown in Fig.1. Cuttlefish backbones taken in Aegean Sea were dried at 100 ºC, ground, sieved to mesh size of 400, and then mixed with cellulose which acts as a binding material. The mixing time was 30 min. A twenty ton hydraulic press has been used to compress the cuttlefish backbone powder into solid circular thin pellet of 13 mm. This circular thin pellet weighed about 200 mg each. The spectra were recorded by the Si (Li) detector having an active area of 12.5 mm² and a sensitive crystal depth of 3 mm and Be window of 0.025 mm thickness. The measured energy resolution of the detector system was 188 eV FWHM for the Mn Kα line at 5.96 keV. To obtain the standard addition curve used for the evaluation of the concentration of each elements cuttlefish backbone samples, a series of individual standards weighing 5, 10, 15, 20 mg have been added. Thus, spectroscopically pure powders of Na_2SO_4 (99.99 %), $MgCl_2$ (99.99 %) , KCl (99.90 %) and $CaCl_2$ (99.99 %) have been used for additions.

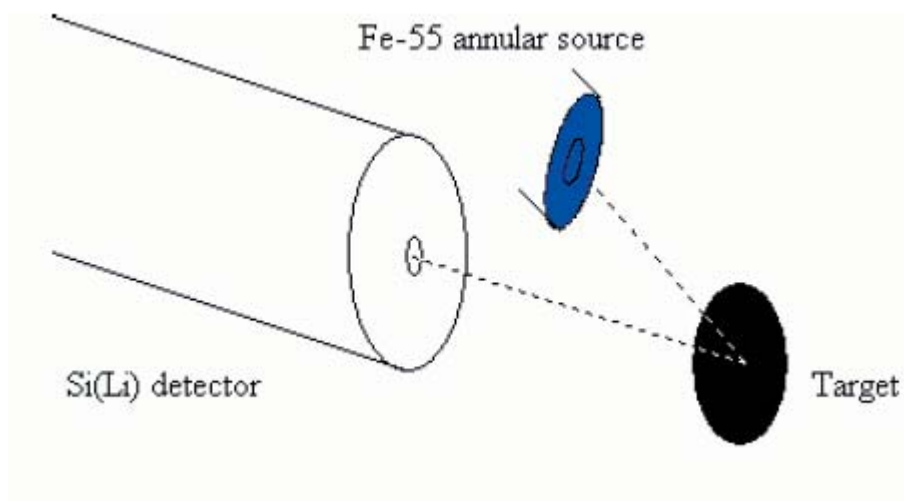Fig. 1. Experimental setup used for measurement of concentrations.

Photons of 5.96 keV energy from ^{55}Fe annular source were used for excitation of the samples. The spectra were collected in about 10800 counts in order to obtain sufficient statistical accuracy.

Experimental method

Standard addition method has been used for the analysis of the elements present Na, Mg, K, and Ca in the cuttlefish backbone samples. The principle of the method is as follows [29]: adding a known amount ΔC_i of analyte i to the unknown sample gives an increased intensity of $I_i + \Delta I_i$. Supposing a linear calibration, the following equations were applied:

$I_i = M_i C_i$ (1) is for the original sample, and
$I_i + \Delta I_i = M_i(C_i + \Delta C_i)$ (2) is for the sample with the standard additions. From Eqs. (1) and (2), C_i can be determined by elimination of the calibration factor M_i. C_i can be obtained by plotting the intensity measured versus concentration of the addition.

Results and Discussion

The spectrum obtained from cuttlefish backbone samples excited by the Fe-55 annular source is shown in Fig. 2. From these spectra, it is clear that cuttlefish backbone sample contains Na, Mg, K and Ca. To measure concentration of Na, Mg, K and Ca in the cuttlefish backbone, intensity versus standard concentration for the elements have been plotted and an example for calcium is shown in Fig. 3. Na, Mg, K and Ca concentration in the cuttlefish backbone samples are almost the same as pathological and non-pathological human elbow bone samples concentration. The concentrations in the cuttle-

fish backbone samples in this work and in our previously study [16] reported pathological and non-pathological human elbow bone samples using X- ray fluorescence technique have been given in Table 1.

Comparisons of the elemental concentrations for cuttlefish backbone and non-pathological human elbow bone samples are depicted in Fig. 4. The coefficient variation in the measurements was 3.11%. The errors arising from uncertainties in the various parameters used to calculate the concentrations of cuttlefish backbone samples include errors due to peak area evaluation (2.2%) and target thickness measurements (2.0%). All the errors were compounded according to the classical rules of the propagation of errors and the resultant error is quoted in the measured cuttlefish backbone sample concentrations. The uncertainties in the parameters are listed in Table 2.
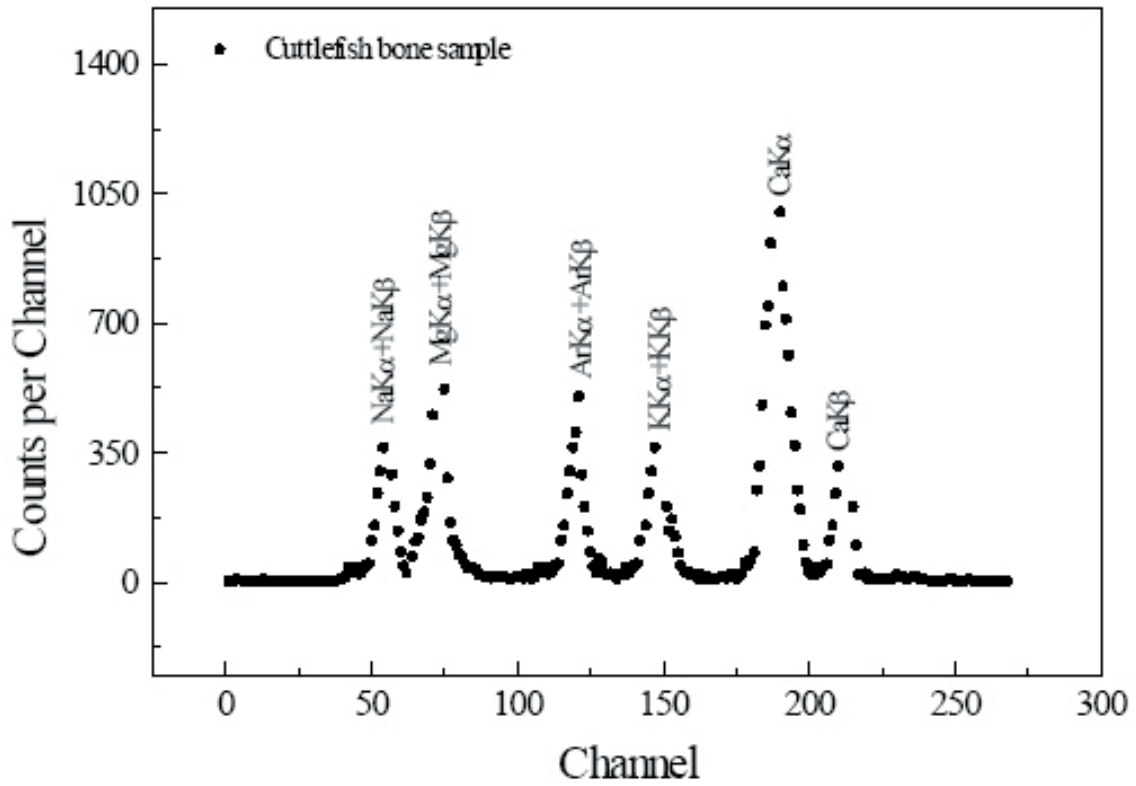
Fig. 2. Typical spectra for cuttlef ish backbone.samples irradiated with 5.96 keV gamma rays from [55]Fe.
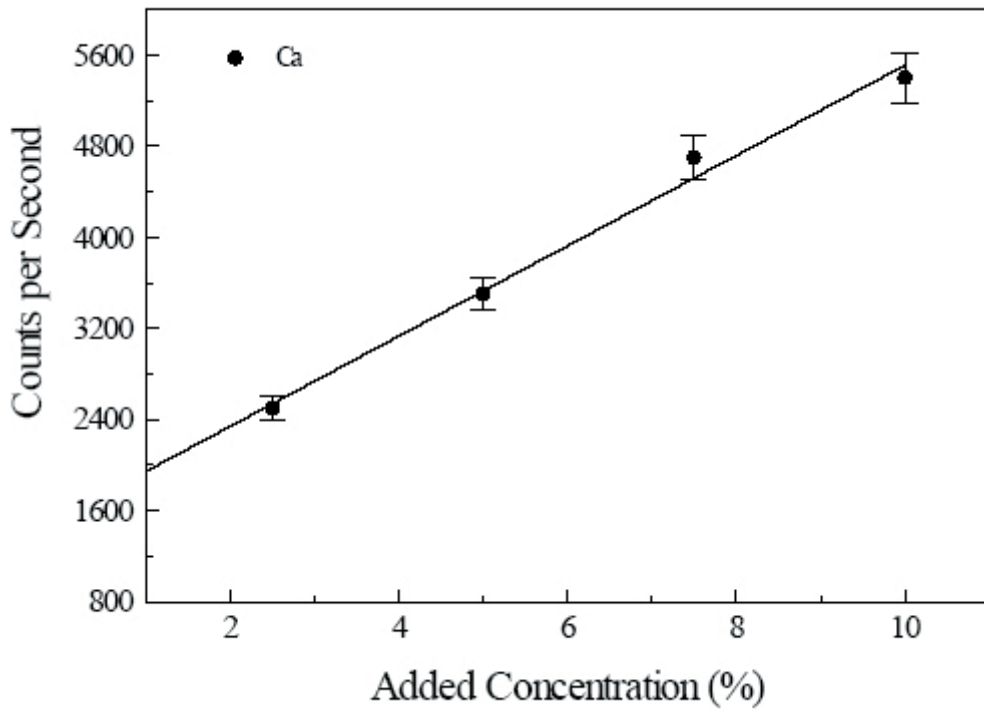

Fig. 3. Calibration curve for calcium in the cuttlefish backbone samples .

Table 1.   Concentrations of cuttlefish backbone and non-pathological human elbow bone [16] (%).

Element	Cuttlefish backbone	Non-pathologigcal human elbow bone [16]	
		Male patient	**Female patient**
Na	2.53±0.12	2.59±0.12	2.28±0.11
Mg	3.11±0.10	3.15±0.11	3.17±0.11
K	0.98±0.08	1.05±0.09	1.11±0.08
Ca	5.13±0.15	5.66±0.14	5.61±0.14

Table 2. Uncertainties in the quantities used to determine cuttlefish backbone samples concentrate in eq.1 and 2.

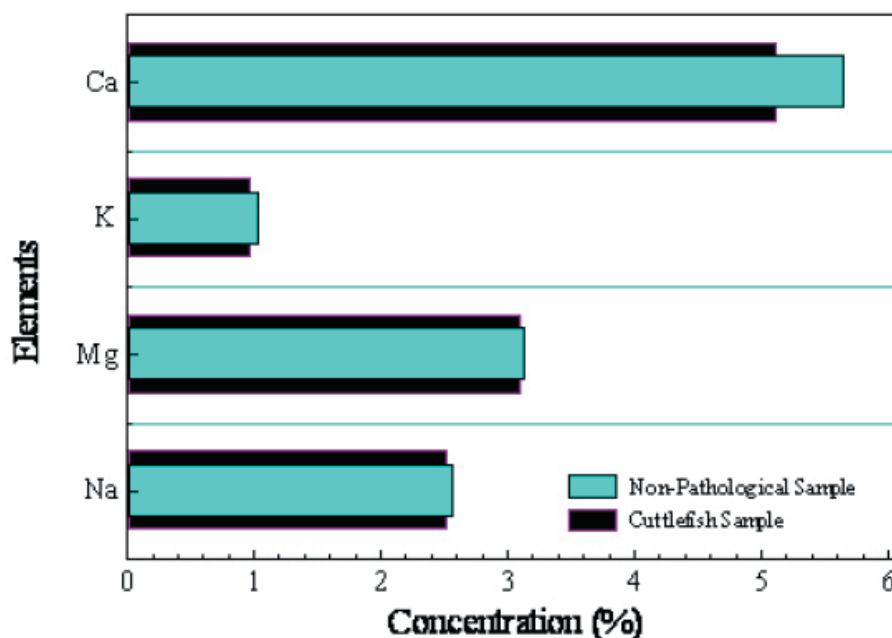| Quantity	Nature of uncertainty	Uncertainty(%)
I_i	Counting statistic	2
ΔI_i	Counting statistic	1
T	Non-uniform thickness	1

Fig. 4. Compar ison of the elemental concentrations for cuttlefish backbone and non-pathological human elbow bone sample for male pa-tient.

Conclusions

In conclusion, energy dispersive X-ray fluorescence technique (EDXRF) is a suitable way to examine ele-ments found in cuttlefish for present work. From our results, we concluded that non-pathological cuttlefish backbone can be used instead of non-pathological hu-man elbow bone in order to knit human elbow bone, particularly cases associated with depletion of human el-low bone. But, because there are no experimental results for the present work in the literature, in order to obtain more definite results, more experimental measurements are needed.

References

1. Laptikhovsky, V., Salman, A., Onsoy, B., Kata-
    gan, T., *Scientia Marina*, **67**, 279 (2003).
2. Webb er, D.M., Aitken, J.P ., O'Dor , R.K.
    Physiol. Biochem. Zool., **73**, 651 (2000).
3. Carvalho, M. L., Casaca, C., Pinheiro, T.,
    Marques, J. P., Chevallier , P. Cunha, A. S., *Nucl.*

Instrum. Meth. B, **168**, 559 (2000).

4. Törük, Sz., Van Dyck, P., and Griken, Van., *X-Ray Spectrom.*, **13**, 27 (1984).

5. Al-Kofahi, M. M., Hallak , A. B., *X-Ray Spectrom.*, **25** 225 (1996).

6. Sulkowski, M., Sulkowski, M., and Hirner A.V., *X-ray Spectrom.*, **25**, 83 (1996).

7. Baman J., Blanck, H., Standzenieks, P., Pettersson, R. P., and Hong, N. T., *X-ray Spectrom.*, **22**, 260 (1993).

8. Holynska, B., Jasion, J., *J. Radionan. Nucl. Ch. Le.*, **105**, 71 (1986).

9. Gil, F. B., Barreira, G., Guerra, M. F., Alves L. C., *X-ray Spectrom.*, **18**, 157 (1989).

10. Al- Kofahi M. M. and Hallak, A. B., *X-ray Spectrom.*, **25**, 225 (1996).

11. Hua, Younan and Yap, C. T., *X-ray Spectrom.*, **23**, 40 (1994).

12. Budak, G., and Karabulut, A., *Spectrochim. Acta B*, **54**, 985 (1999).

13. Karabulut, A., Budak , G., Polat, R., Gürol, A., Levent, M., Şahin, Y., *J. Quant. Spectrosc. Ra.*, **72**, 741 (2002).

14. Neslihan Ekinci, Neslihan Astam, Yusuf Şahin, *J. Quant. Spectrosc. Ra.*, **72**, 783 (2002).

15. Neslihan Ekinci, Yusuf Şahin, *Spectrochim. Acta B*, **57**, 167 (2002).

16. Ali Okur, Yüksel Özdemir and Rıdvan Durak., *J. Quant. Spectrosc. Ra.*, **78**, 55 (2003).

17. Yüksel Özdemir, Ali Okur , Lütfü Tatlı and Rıdvan Durak., *Instrum. Sci. Technol.*, **31**, 77 (2003).

18. Heest, A.V., Swiontkowski, M., *Lancet*, **353**, 28 (1999).

19. Albee, F .H. *Clin. Orthop.*, **324**, 5 (1996).

20. Friedlander, G.E., *J. Bone Joint Surg.*, **69A**, 786 (1987).

21. Lu, M., Rabie, A.B.M., *Arch. Oral Biol.*, **47**, 831 (2002).

22. Inoue, K., Ohgushi, H., Yoshikawa, T., Okumura, M., Sempuku , T., Tamai, S., Dohi, Y., *J. Bone Miner. Res.*, **12**, 989 (1997).

23. Bostrom, M.P., Yang, X., Kennan, M., Sandhu, H., Dicarlo, E., Lane, J.M., *Spine*, **26**, 1425 (2001).

24. Pekler, R.R., Friedlander, G.E., *Orthop. Clin. North Am.*, **18**, 235 (1987).

25. Young, W.F., Rossenwasser, R.H., *Spine*, **18**, 1123 (1993).

26. Kuboki, Y., Takita, T., Kobayashi, D., Tsuruga, E., Inoue, M., Murata, M., Nagai, N., Dohi, Y., *J Biomed. Mater. Res*, **40**, 190 (1998).

27. Oktar , F.N., Göller , G., Heybeli, N., Varol, R., *J Arthropasty Arthroscopic Surgery*, **13**, 99 (2002).

28. Karaismailoğlu, T.N., Tomak, Y., Andaç, A., Ergün, E., *Acta Orthop. Traumatol. Turc*, **36**, 147 (2002).

29. R. E. Van Grieken, A. A. Markowicz, Handbook of X-ray Spectromety, Marcel Dekker Inc., Basel, Hong Kong, New York, 1993.

Detection limit enhancement of Cd, Ni, Pb and Zn determined by flame atomic absorption spectroscopy

A. A. Shaltout and M. A. Ibrahim

Spectroscopy Department, Physics Division, National Research Center, El Behoos Street, Dokki, Cairo, Egypt.

Abstract

In the present work, the optimization of the different parameters including absorbance mode and the measuring time is promising for lowering detection limits for flame atomic absorption spectroscopy. Results indicate that the limit of detection could be enhanced with adapting the absorbance mode as well as the measurement times. The optimum measuring time was 6 sec while using peak height as the absorbance mode for Ni and peak area for the remaining metals. The calculated detection limits were 9.0, 3.0, 9.0 and 3.0 µgL^{-1} for Cd, Ni, Pb and Zn respectively. Therefore, one can extend the concentration of the trace elements to very low values, and some graphite furnace measurements can be replaced by FAAS.

Keywords: Detection Limit, FAAS, Flame parameters.

Résumé

Dans le présent travail, l'optimisation de différents paramètres incluant, le mode d'absorbance et le temps de mesure, se montre prometteuse pour abaisser les limites de détection en spectroscopie d'absorption atomique avec flamme. Les résultats indiquent que la limite de détection peut être améliorée en adaptant le mode d'absorbance mode ainsi que les temps de mesure. Le temps de mesure optimale était de 6 sec alors que le mode d'absorbance mode était la hauteur de pic pour Ni et la surface de pic pour les autres métaux. Les limites de détection calculées ont été de 9.0, 3.0, 9.0 et 3.0 µgL^{-1}

pour Cd, Ni, Pb et Zn, respectivement. Ainsi, on peut mesurer la concentration des éléments traces à de très basses valeurs, en remplaçant de mesures à la fournaise graphite par des mesures à la flamme (FAAS).

Introduction

Flame atomic absorption spectroscopy, FAAS, is a well known quantitative elemental analysis method for a wide range of samples. It is simple, inexpensive, rapid, and applicable to wide range of samples [1-3]. The limits of detection of the different elements with AAS have been tabulated by several workers and the importance of detection limit enhancement for all elements in FAAS becomes clear. This can be done by optimizing the different parameters. Flame atomic absorption spectroscopy (FAAS) is considered as a specific technique with little interference as compared to other techniques [1-5]. The effect of flame parameters upon analytes were carried out by different authors [6-10] and it is shown that the mode of absorbance plays a key role in FAAS. The necessity of a suitable absorbance mode in FAAS was mentioned elsewhere [7-11]. AAS is considered a universal technique for the determination of trace metals in a wide range of samples [12-14].

In the present work, an enhancement of the limits of detection of Cd, Ni, Pb and Zn was carried out by optimizing conditions of the different measuring time (2-8 sec) and different absorbance modes (prompt, peak height, peak area, and integration) and without any chemical treatments such as pre-concentration or extraction which are mentioned elsewhere [15-19]. It was found that the operating conditions play an important role for decreasing the limits of detection.

*Author to whom correspondence should be addressed:
e-mail address: medahmed6@yahoo.com (M. A. Ibrahim)

Experimental

Materials

Synthetic heavy metals of Cd, Ni, Pb and Zn were prepared by diluting standard solutions of 1000 mg/L of each metal. The stock solution is purchased from Merck, Germany.

A sample of 99.99% Cu alloy was used in order to verify our experimental work. The sample was supplied by "El Sewedy Cables Company, Cairo, Egypt". An open acid digestion procedure was used because the Cu sample alloy can be easily dissolved in nitric acid. A 0.5 g of Cu alloy sample was digested by 10 mL of concentrated HNO_3 (68%, BHD, England) in glass beaker and the mixture is heated on a hot plate to evaporate the sample slowly to near dryness. After evaporation, the volume is reduced to about 2 mL. Double-distilled water is then added and the solution is transferred to a 50 mL volumetric flask and filled to volume to give a 1:100 sample dilution.

Tap water was subjected to acid digestion by 10 mL of HNO_3 was then heated gently until the brown fume disappears.

Instrumentations

A Varian Model SpectrAA220 atomic absorption spectrometer with four hollow cathode lamp positions was employed. The light sources of the different elements were hollow-cathode lamps from Cathoden, UK. The light beam through Air-Acetylene was controlled by an aperture for measuring absorbance in a different slit widths depending on the measured element. The oxidant rate was 4.5 L/min and the fuel rate (C_2H_2) was 1.5 L/min [20]. The most sensitive absorption lines of the elements Cd, Ni, Pb and Zn were used as shown in Table 1. Standard solutions were aspired into the flames after the burner had been allowed to operate for 5-10 min. In this way, thermal equilibrium was attained before any final adjustment was made to the absorbance mode, measuring time, burner height, gas flows or amplifier gain. In this case, the maximum sensitivity will

be expected. All absorbance values are the average of ten readings recorded successively from the different absorbance modes.

The background absorption is measured and subtracted from the total absorption in order to determine the actual atomic absorption signal. For this reason, a continuum source of deuterium arc lamp in ultraviolet has been used to measure only the background contribution to the absorption signal which has essentially zero atomic absorption sensitivity at the normal resolution for atomic absorption instruments. In this case, the background correction is carried out automatically by employing a background correction system.

Results and Discussion

According to the literature, several articles explained the determination of minor and trace elements in different types of materials by flame AAS. Therefore, the importance of detection limit enhancement for the elements in order to increase the concentration range of flame AAS becomes clear and this can be done by the optimization of the different parameters.

Absorbance modes and measuring time's optimization

Optimizing the parameters of FAAS is essential in order to obtain a satisfied and real contribution of the real sample as well as a low limit of detection. Therefore, the calibration curves of Cd, Ni, Pb and Zn were demonstrated at different absorbance modes (Prompt, integration, peak height and peak area) and different measuring time (2, 3, 5, 6 and 8 sec). A known concentration of these elements was used as unknown sample in order to find out the optimal working conditions. For Zn measurements, the spectral line was at 231.9 nm, a slit width of 1 nm and a current of 5 mA were used. In the case of Pb, the spectral line was at 217.0 nm, a slit width of 1 nm and a current 5 mA was used. In addition, for Cd measurements, the spectral line was at 228.8 nm, a slit width of 0.5 nm and a current of 4 mA was used. Finally for Ni measurements, the spectral line at 232.0 nm, a slit

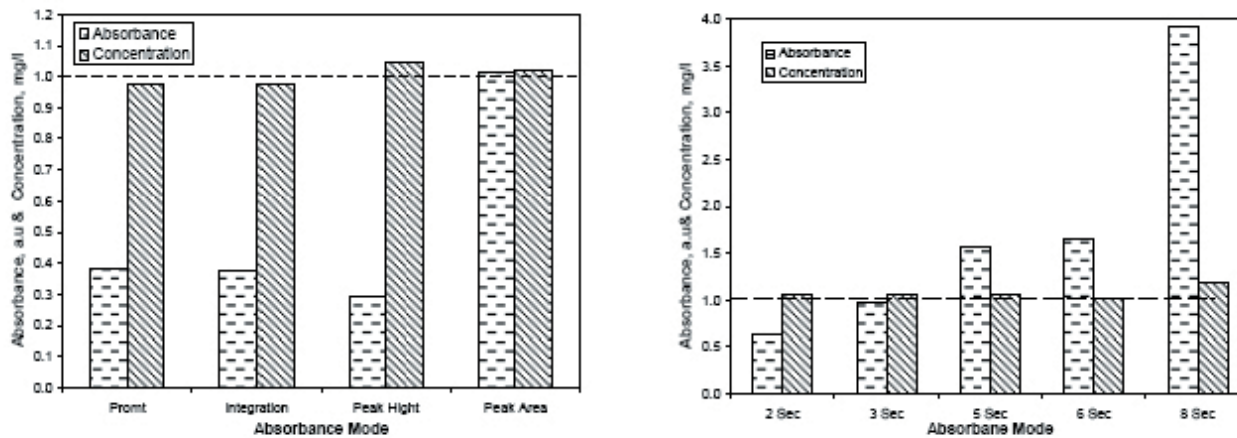Table 1. Summary of the optimal operational conditions for Cd, Ni, Pb and Zn

| Element	Optimal Conditions				
	Absorbance mode	Wavelength, nm	Measuring time, sec	slit width, nm	Current, mA
Cd	Integration	228.8	2, 3, 4, 6 or 8	0.5	4
Ni	Integration	232.0	8	0.2	4
Pb	Peak Area	217.0	8	1.0	5
Zn	Peak Area	231.9	6	1.0	5
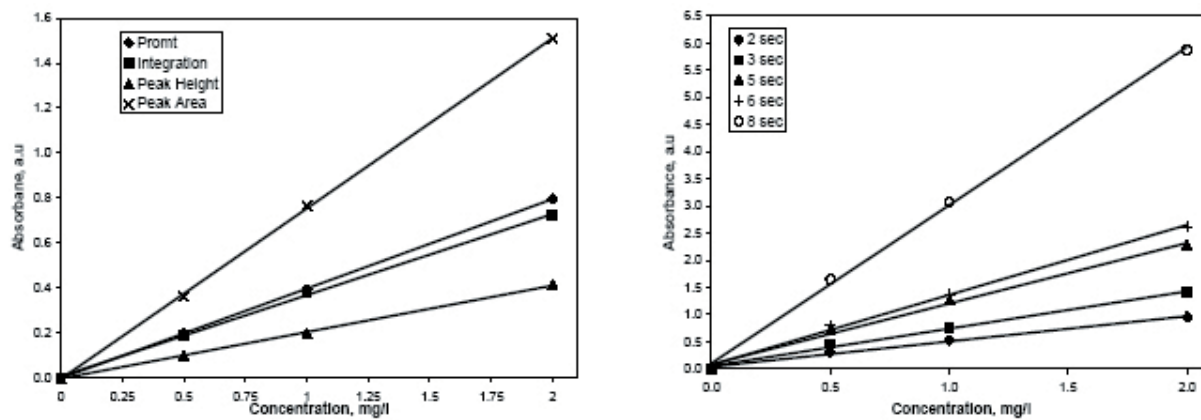
(a) Calibration curves
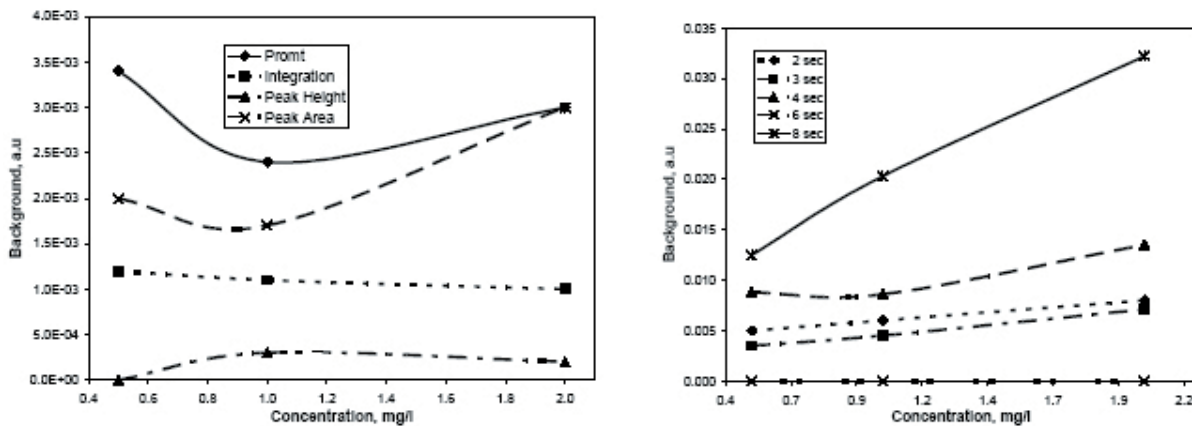
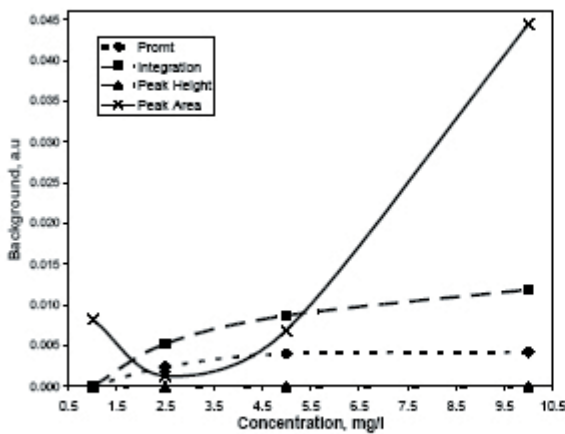(b) Background versus concentration

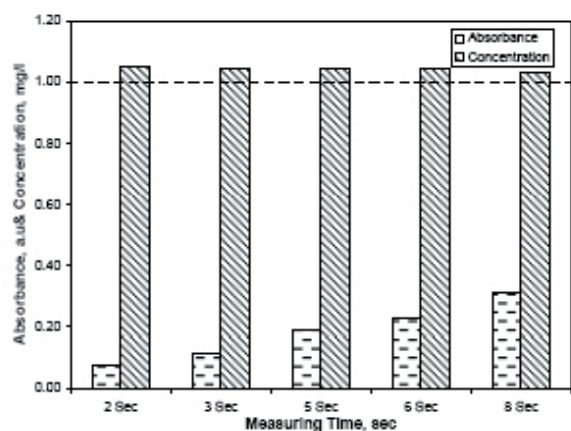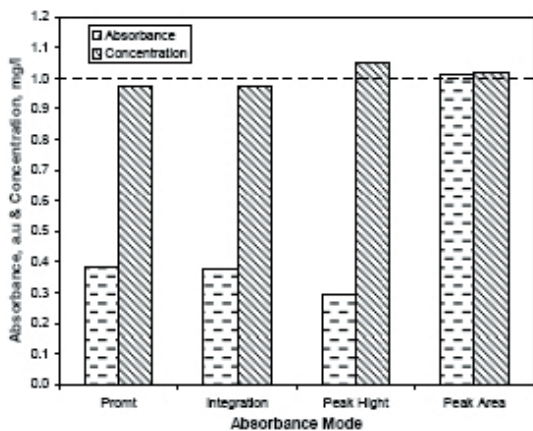(c) Absorbance and concentration versus absorbance modes

Fig. 1 The calibration curves (a), the background versus concentration (b) and the absorbance and concentration versus Absorbance mode (c) of Zn at different time and absorbance modes.
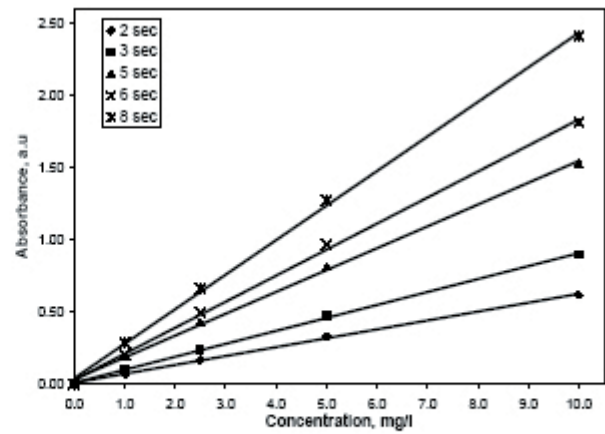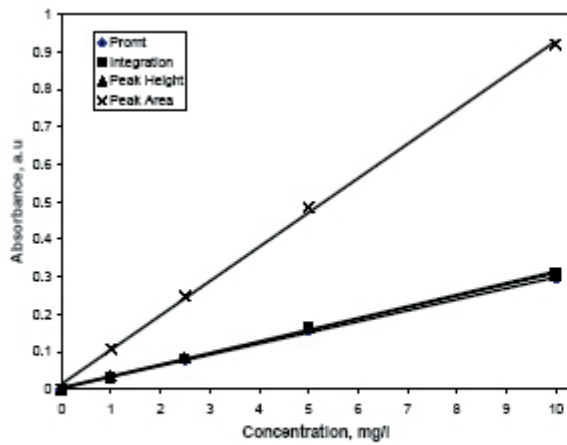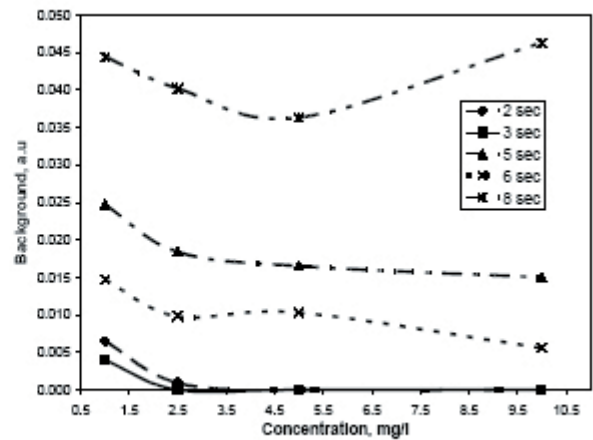
(a) Calibration curves

(b) Background versus concentration

(c) Absorbance and concentration versus absorbance modes

Fig. 2 The calibration curves (a), the background versus concentration (b) and the absorbance and concentration versus Absorbance mode (c) of Pb at different time and absorbance mode.
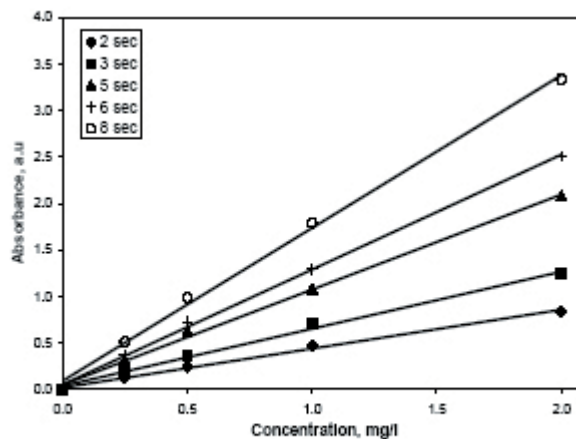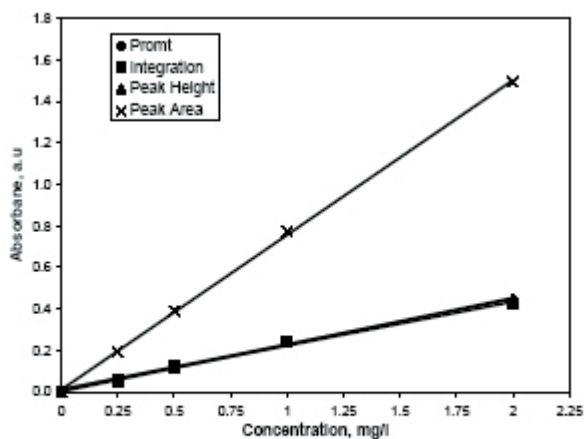
(a) Calibration curves

(b) Background versus concentration

(c) Absorbance and concentration versus absorbance modes

Fig. 3 The calibration curves (a), the background versus concentration (b) and the absorbance and concentration versus absorbance mode (c) of Cd at different time and absorbance modes.

(a) Calibration curves
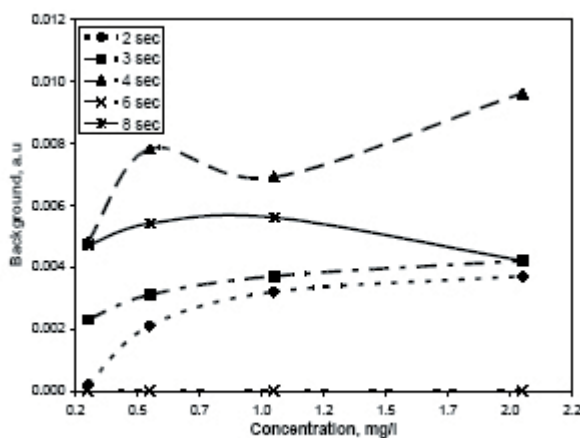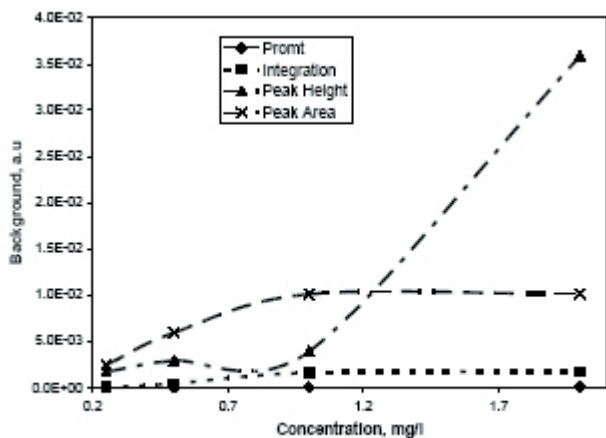

(b) Background versus concentration

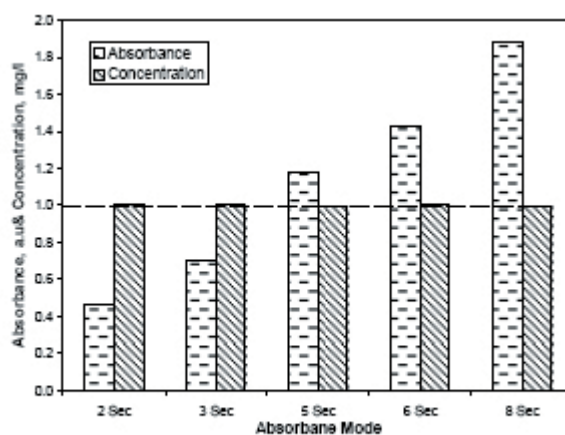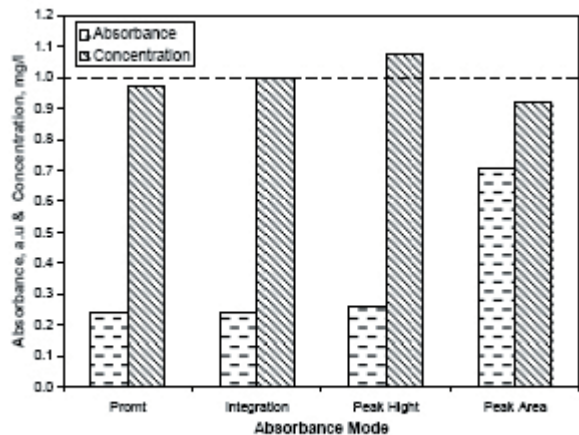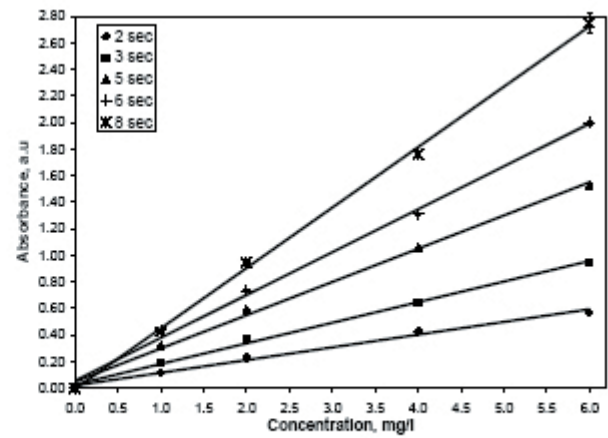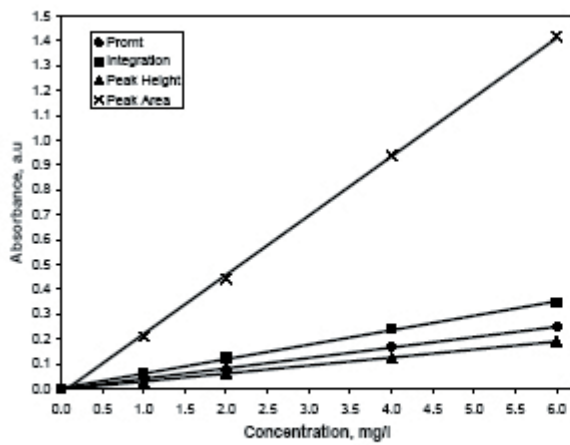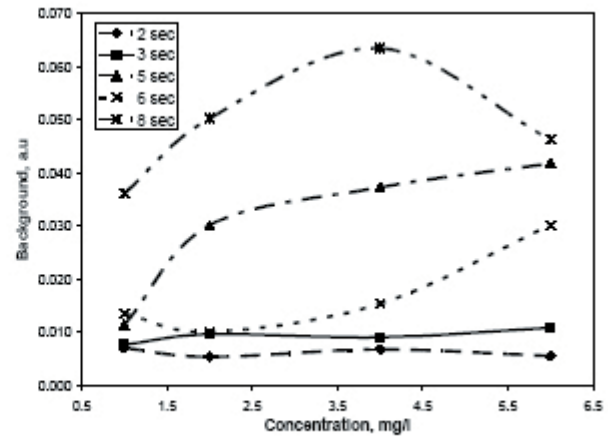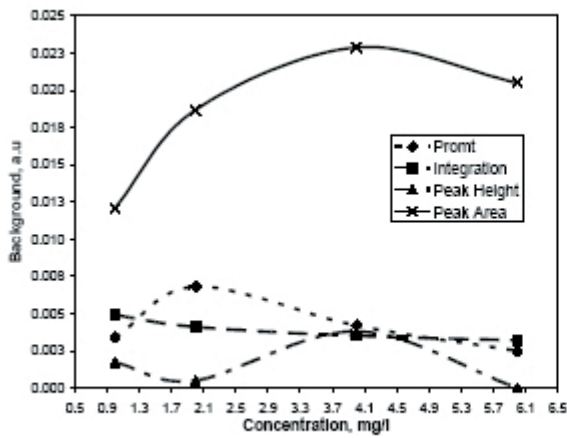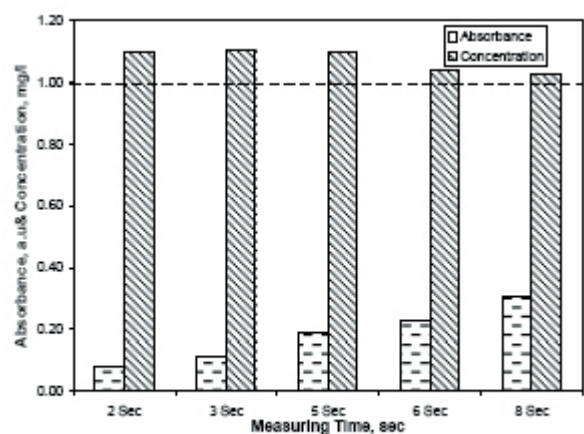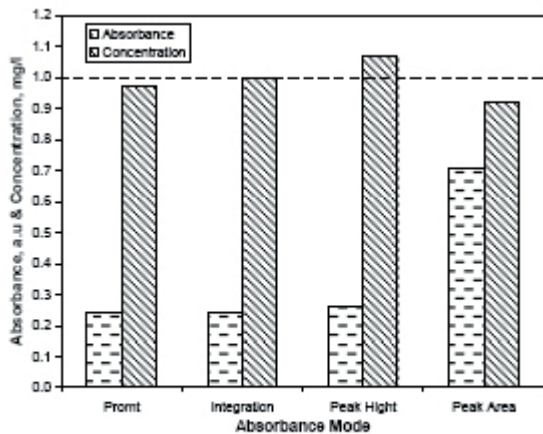(c) Absorbance and Concentration versus Absorbance mode

Fig. 4 The calibration curves (a), the background versus concentration (b) and the absorbance and concentration versus absorbance mode (c) of Ni at different time and absorbance modes.

width of 0.2 nm and a current 4 mA was used.

Figures 1a-4a illustrate the relation between the concentration of Zn, Pb, Cd and Ni versus the absorbance at different absorbance modes and different measuring times. It seems that the absorbance of the peak area mode is higher than the other absorbance modes. In the case of Zn, the measurement of the absorbance by prompt and integration gives approximately the same values. The peak height mode of Zn and Ni gives the lowest absorbance value. In the case of Pb and Cd, the measurement of the absorbance by prompt, integration and peak height gives approximately the same value. In the case of Ni, the measurement of the absorbance integration mode gives approximately the higher value than the prompt mode. At different measuring times as illustrated in Figs. 1a-4a, one can conclude that the absorbance of Zn, Pb, Cd and Ni increases as the measuring time increases. When the measuring time was at 8 sec, one can obtain the maximum absorbance signal.

Figs. 1b-4b show the relation between the absorbance of the background signals versus concentration of Zn, Pb, Cd and Ni, respectively, at the different absorbance modes and at different measuring time. One can easily remark the lowest background value of the peak height mode for Zn, Pb and Ni whereas the prompt mode gives the lowest background in the case of Cd. The highest background values are different from element to another. In the case of Zn, the highest background was found with the prompt mode. Peak area mode gives the highest background with Pb and Ni. In the case of Cd, the peak height gives the highest background. In general, one can easily remark that the background increases as the concentrations of the matrix solution increases. This means that the background value of the diluted samples will be lower as the concentration of the samples decreases. In some cases (integration mode of Ni and Zn and the peak height mode of Cd and Pb), the absorbance of the background does not change with increasing concentration. Generally, one can conclude that the background absorbance of the peak area for the four elements is remarkably of high values and the background correction will be essential. On the other side as given in the left part of Figs. 1b-4b, the background absorbance increases as the measuring time increases. This is not valid for all cases whereas at measuring time of 6 sec, the background absorbance gives the minimum value for Zn and Cd. Furthermore, the absorbance corresponding to background at measuring time of 6 sec is relatively lower than those at measuring times 5 and 8 sec and close to those at measuring times of 2 and 3

sec. At different measuring times, the absorbance of the background increases as the concentration increases. In the case of Pb, the behavior of the absorbance of the background is completely different whereas it decreases as the concentration increases.

In order to evaluate the quality of the different mentioned absorbance modes and the different measuring times, a synthetic sample concentration (1 mg/L of Cd, Ni, Pb, Zn) has been checked. Furthermore, a real Cu alloy sample has been also checked. Figs. 1c-4c illustrates the relation between the absorbance modes as well as measuring times versus the absorbances and the concentrations of the synthetic sample. As shown in Figs. 1c-4c, the absorbance mode of the peak area represents the highest absorbance for all elements. One can easily observe that the absorbance of the peak area is twice or more the absorbance of the other absorbance measurement modes. Furthermore, the peak height mode represents the lowest absorbance for Zn and Pb and the prompt absorbance mode represents the lowest absorbance for Cd and Ni. Furthermore, the final concentration of the peak area is closer to the real concentration in the case Zn and Pb. The final concentration of the integration is the closest to the real concentration of Cd and Ni. According to the experimental results, the peak area mode is the most convenient absorbance mode in order to detect most trace elements and this is in agreement with previous work of Röle [11]. In addition, the absorbance mode of integration is also recommended if the absorbance mode of the peak area appears unreliable. In the present work, we consider the absorbance mode of the peak area as the optimum operating condition.

Therefore, at the absorbance of the peak area and at constant delay time (5 sec), the absorbance and concentration of the synthetic sample was re-measured versus different measuring times (2, 3, 5, 6 and 8 sec). One can see from Figs. 1c-4c that the absorbance of the sample increases as the measuring time increases. This means that the absorbance of the sample at a measuring time of 8 sec is the highest one compared with the absorbance of other measuring times. In the case of measuring times 8 and 6 sec, the concentration of the sample is closest to the real concentration. Meanwhile, in the case of measuring time of 6 sec, the measuring background was very low or close to zero. Therefore, the measuring time of 6 sec has a low background and it is the closest one with the sample as illustrated in figs. 1c-4c. From the present work, we found that the optimum conditions can be attained at the peak area absorbance mode and at a measuring time ranging from 6 to 8 sec.

The detection limits and comparison with the previous work

The detection limit is affected by all parameters. These parameters include the type of nebulizer, the type of sample, absorbance mode and the measuring time. For samples containing high salt content, the limit of detection is usually higher than that for pure aqueous solutions. In the present work, the limit of detection C_L is determined by recording the absorbance and the background of the wavelength of the spectral line of Cd, Ni, Pb and Zn while nebulizing a solution of a relatively low concentration of these elements into the excitation source.

In the present work, we used the limit of detection for comparing the power of detection of the optimized flame AAS with previous published results. To obtain the limit of detection of a specific element, it is necessary to estimate the average value of the background response at a particular wavelength of this element and the related

Z time's standard deviation. The value of Z is related to the statistical interpretation of the limit of detection. Its magnitude is chosen to correspond to the desired confidence level values of accepted value of $3\sqrt{2}$ and $2\sqrt{2}$ [21] which are usually taken as accepted values of Z.

Fig. 5 illustrates the relation between the limits of detection versus absorbance modes. The peak area mode seems to be the most promising for all elements and the lowest limit of detection can be obtained by it. Furthermore, Fig. 6 illustrates the relation between the limits of detection and the measuring time. In this case, the absorbance and the background of each element were re-measured at the optimum absorbance mode (peak area). As shown in Fig. 6, the limit of detection is further decreased and the lowest limits of detection values were obtained at a measuring time of 6 s. At a measuring time of 6 s, the limit of detection ranges from 3 to 9 µg/L.

Table 2 compares the present limits of detection with the published values. It has to be mentioned that, the pres-
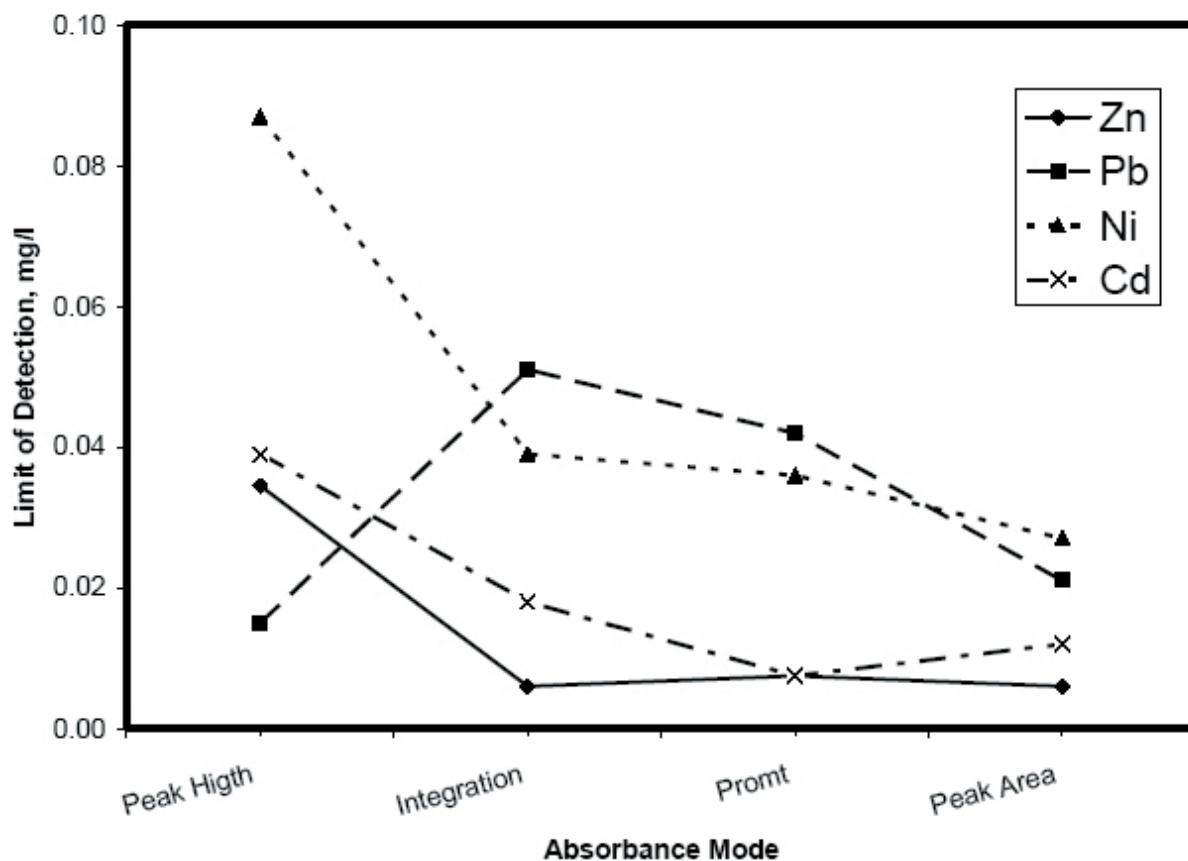
Fig. 5 Relation between the limit of detection versus absorbance modes for Cd, Ni, Pb and Zn.
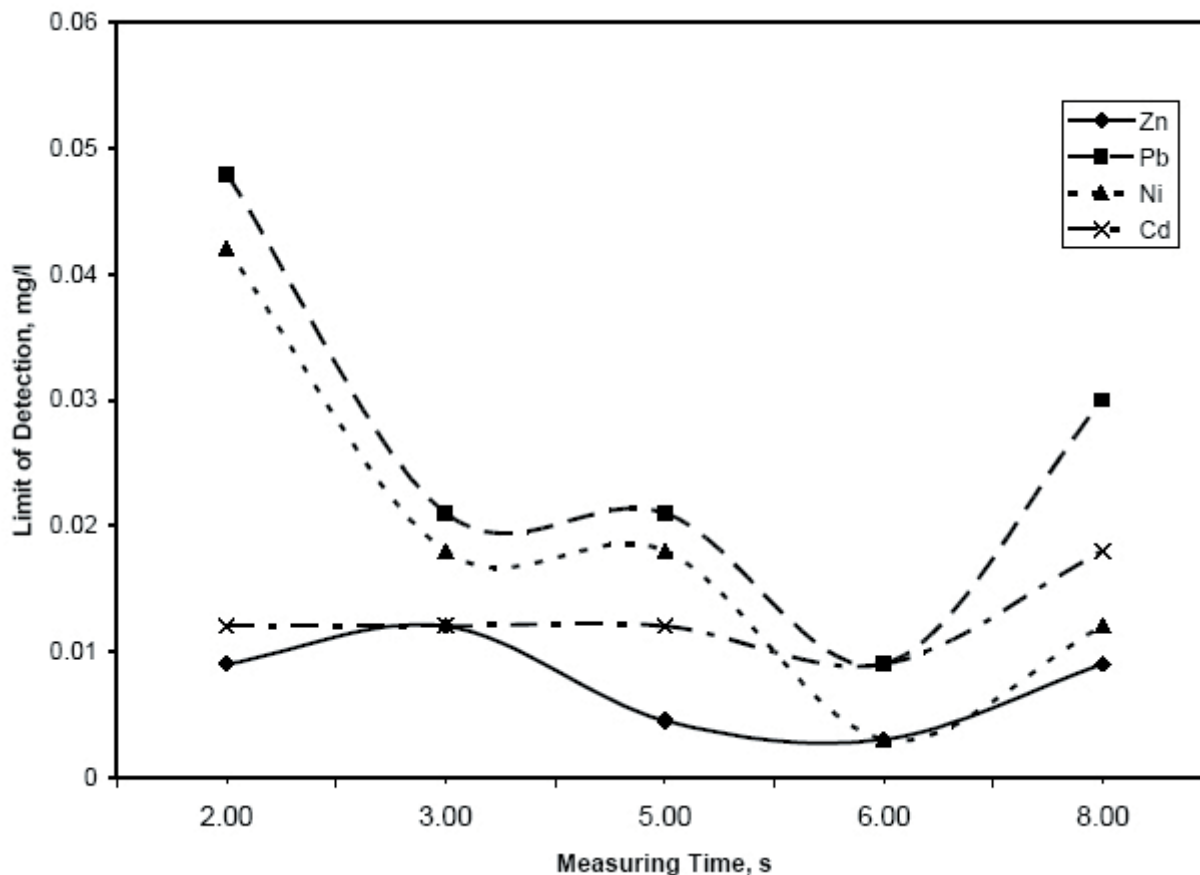
Fig. 6 Relation between the limit of detection versus measuring times for Cd, Ni, Pb and Zn.

Table 2. Comparison between detection limits of the studied elements in this work and that from the literature.

Element	λ, nm	Limit of Detection, μg/L	
		Present work	**Previous work [ref]**
Cd	228.8	9	1.8 [4]
			20.0 [15]
			2.0 [20]
			6.0 [24]
Ni	232.0	3	2.9 [16]
			10.0 [20]
			1.1 [22]
Pb	217.0	9	6.6 [4]
			22.5 [16]
			1.2 [17]
			10.0 [20]
			16.0 [24]
Zn	231.9	3	1.2 [4]
			2.9 [16]
			1.0 [20]
			18.9 [23]

ent limit of detection is obtained through optimization only and without pre-concentration or any other chemical treatments and this is a remarkable difference between the present and the previously published work. Some of the present detection limit values are slightly higher than that of some values of the literature, as pre-concentration or extraction process were used in the previous work. Therefore, the limits of detection were close or even better than these given in this work. As shown in Table 2, the present limits of detection are comparable to the published values which were obtained using pre-concentration and/or chemical processing. Therefore, the new limits of detection will extend the range of quantitative determination of the different elements.

Application of the method

Quantitative analysis in Cu alloy sample

Copper was analyzed two times by independent techniques. As seen in Table 3, there was an agreement between the two previous analytical results. In order to determine Cd, Ni, Pb and Zn, the Cu sample alloy was digested and analyzed by flame AAS.

The concentration of Cd, Pb, Ni and Zn was determined at the obtained optimum condition (peak area mode and 6 sec measuring time) and compared with the previous quantitative analysis results. As it can be seen,

the maximum concentrations of the mentioned heavy elements are less than 0.0368 mgL^{-1} and it is near to the new detection limit. This indicate that the results of flame AAS was in agreement with the previous results as shown in Table 3. Therefore, the quantitative analysis of heavy elements using flame AAS can be extended to lower concentration ranges exceeding the published results.

Quantitative analysis of Tap water

Tap water from our laboratory without any treatment was subjected directly to FAAS analyses. The values of concentration and limits of detection of Cd, Ni, Pb and Zn are given in Table 4.

Quantitative analysis and limits of detection of Cd, Ni, Pb and Zn were carried out. Table 4 indicated that the limits of detection decreased as a result of digestion. Digestion process leads to an increase in concentration of the element within the sample volume and hence its availability is increased to the neublizer. For tap water, the maximum accuracy of measurements could be achieved by performing our optimization in one hand and the detection limit is improved as a result of digestion on the other hand. The detection limit of Cd is improved from 1.494 µg/L to 0.825µg/L. Ni, which was not even detected directly resulted 9.570 µg/L after treatment. Furthermore, Pb is enhanced from 20.760 µg/L to 4.890 µg/L. Finally, 10.827 µg/L of Zn was found, which is slightly enhanced from 14.018 µg/L.

Table 3. Quantitative analysis of Copper sample alloy

Element	Concentration, mg/L		
	Present work	**Previous analysis [1]**	**Previous analysis [2]**
Cd	0.46	0.40	0.32
Ni	0.61	0.20	0.58
Pb	3.45	1.78	3.68
Zn	2.95	1.46	2.63

Table 4. Detection limits of the studied elements which determined in tap water.

Element	Concentration, mg/L	Detection Limit, µg/L	
		Untreated	**Treated**
Cd	4.750	1.494	0.825
Ni	2.950	BDL	9.570
Pb	1.500	20.760	4.890
Zn	862.500	14.018	10.827

BDL: Below the detection limit

Conclusions

Flame AAS shows satisfactory limits of detection as a result of optimizing the flame parameters. Good values of detection limits are observed as compared with those in the literature. The new detection limit values have been obtained for Cd, Ni, Pb and Zn that range from 3 to 9 µg/L. This result is encouraging to carry out quantitative analysis of the different elements in different samples by flame AAS at very low concentrations. For the determination of the studied metals in tap water, it is recommended to improve the detection limit with a digestion of samples prior to analyses. Furthermore, better detection limits of tap water could be obtained with the help of sample extraction which is beyond the scope of our work because this kind of treatment affects the flame parameters [4].

Acknowledgements

References

1. L. M. Voth, Varian Techtron Publication No. 35 (1983).
2. S. L. Ellison, M. Rosslein, A. Williams, "Eurochem/Citac guide- Quantifying Uncertainty in Analytical Measurements", 2nd Ed., page 70 (2000).
3. C. Vandecasteele and C. B. Block, Modern Methods for Trace Elements determinations, John Willey & Sons Ltd., Baffin's Lane, Chichster, West, Sussex, England. (1993).
4. M. A. Ibrahim, Ph.D. thesis, Faculty of Science Cairo University, Egypt. (2000).
5. G. S. El-Bahy, H.I. Abdel-Shafy, M.A. Ahmed and M.A.A. Ibrahim, *Bull. NRC, Egypt*, **29**, 301 (2004).
6. M. A. Ibrahim and Kh. E. Elnagar, 1st annual Measurement Science Symposium; 26– 29 September 2001, National Institute for Standards, Cairo, Egypt, 2001.
7. H.E. Piepmeier, L. de Galan, *Spectrochim. Acta B*, **31**, 163 (1976).
8. P. Scharmel, *Anal. Chim. Acta*, **72**, 414 (1974).
9. R.E. Sturgeon, C.L. Chakrabarti, I.S. Maines, P.C. Bertels, *Anal. Chem.*, **47**, 1240 (1975).
10. R. D. Beaty, "Concepts, Instrumentation and Techniques in Atomic Absorption Spectrometry", Perkin-Elmer Corporation, p 29-31, USA, (1978).
11. R. Röle, *Anal. Chem.*, **58**, 13, 2891 (1986).
12. M. Tüzen, M. Soylak, *B. Environ. Contam. Tox.*, **74**, 968 (2005).
13. M. Tüzen, M. Soylak, *J. Food Drug Anal.*, **13**, 343 (2005).
14. M. Soylak, H. Çolak, M. Tüzen, O. Türkoğlu, L. Elçi, *J. Food Drug Anal.*, **14**, 62 (2006).
15. N. Pourreza and H. Z. Mousavi, *Anal. Chim. Acta*, **503**, 279 (2004).
16. G. Doner and A. Ege, *Anal. Chim. Acta*, **547**, 14 (2005).
17. R. L. Dutra, H. F. Maltez and E. Carasek, *Talanta*, **69**, 488 (2006).
18. W. N.L. dos Santos, J. L.O. Costa, R. G.O. Araujo, D. S. de Jesus and A. C.S. Costa, *J. Hazard. Mater.*, **137**, 1357 (2006).
19. W. Ngeontae, W. Aeungmaitrepirom and T. Tuntulani, *Talanta*, In Press.
20. Flame Atomic Absorption Spectrometry, Analytical methods, Varian manual book, Australia, 1989.
21. P.W.J.M. Boumans, J.J.A.M. Vrakking, *Spectrochim. Acta*, **42B**, 819 (1987).
22. A.R. Maurí-Aucejo, T. Arnandis-Chover, R. Marín-Sáez and M. Llobat-Estellés, *Anal. Chim. Acta*, In Press.
23. M. S. Hosseini, H. Raissi and S. Madarshahian, Reactive and Functional Polymers, In Press,
24. S. L. C. Ferreira, W. N. L. dos Santos and V. A. Lemos, *Anal. Chim. Acta*, **445**, 145, (2001).

Analytical characterization of Baltic amber by FTIR, XRD and SEM

I. Pakutinskiene[a], J. Kiuberis[a,c], P. Bezdicka[b], J. Senvaitiene[c] and A. Kareiva[c]*

[a]Department of Analytical and Environmental Chemistry, Vilnius University, Naugarduko 24, LT-03225 Vilnius, Lithuania
[b]Institute of Inorganic Chemistry, Academy of Sciences of the Czech Republic, CZ-25068 Rez, Czech Republic
[c]Department of General and Inorganic Chemistry, Vilnius University, Naugarduko 24, LT-03225 Vilnius, Lithuania

Abstract

Systematic investigation of different amber samples collected in Lithuania was performed using FTIR spectroscopy, X-ray diffraction analysis (XRD) and scanning electron microscopy (SEM). For the characterization, amber samples having different physical appearance (milky, dark, opaque and transparent) found in 2005 at the Baltic Coast, archaeological amber samples excavated in different archaeological complexes and historical "unknown" amber sample found in the old town of Vilnius have been chosen. All amber samples were characterized by FTIR spectroscopy, which revealed characteristic features of the Baltic amber, thus identifying the type of amber. The XRD results revealed that in some samples, a small amount of quartz is trapped inside amber. Almost identical microstructure was observed for all seven amber samples irrespective of their origin. Finally, an aqueous sol-gel processing method has been suggested for the fabrication of coatings for the protection of degradation of amber.

Keywords: Baltic amber, FTIR spectra, XRD analysis, SEM, protective coatings

Résumé

Nous avons effectué une étude systématique sur différents échantillons d'ambre recueillis en Lituanie, en utilisant la spectroscopie FTIR, l'analyse de diffraction (XRD) et la microscopie électronique à balayage (SEM). Pour leur caractérisation, nous avons choisi des échantillons d'ambre possédant des apparences physiques différentes (laiteuse, foncée, opaque et transparente), retrouvés en 2005 sur la côte Baltique, des échantillons archéologiques d'ambre excavés de différents complexes archéologiques et un échantillon historique "inconnu" retrouvé dans la vieille ville de Vilnius. La caractérisation par spectroscopie FTIR de tous les échantillons a révélé les traits caractéristiques de l'ambre de la Baltique en fournissant une possibilité de déterminer leur identité. Les résultats XRD ont révélé que certains échantillons contenaient une petite quantité de quartz. Une microstructure quasi-identique a été observée dans tous les sept échantillons d'ambre quelque soit leur origine. Finalement, une méthode aqueuse sol-gel a été suggérée pour fabriquer des revêtements qui empêchent la dégradation de l'ambre.

Introduction

Amber is a wide group of historical finds and its analysis reveals important information about the daily life and the ethnic and cultural aspects of the society of the period (1-3). To date, the literature on amber deals predominantly with its botanical significance, identification and provenance of different inclusions (insects, plant species and so on) (4-8). However, the literature data are sparse on the prevention of amber deterioration, especially by environmental control. The National Museums located all over the world contain thousands pieces

*Author to whom correspondence should be addressed: e-mail address: Tel.: 370-5-2336214; Fax: 370-5-2330987: E-mail: aivaras.kareiva@chf.vu.lt (Prof. Aivaras Kareiva)

of amber in their collections. These important historical amber objects in museums and archives sometimes suffer very serious damage (9-11). The reasons for this destruction are not fully understood yet. It is believed that the deterioration of amber samples, manifested by surface cracking, darkening, crazing, powdering and discolouration appears primarily as a result of the destructive effects by oxidation in air. Therefore, careful characterization of historical amber is a very important task not only for collectors and naturalists but for people working in the field of conservation chemistry as well (12).

Several analytical techniques such as ^{13}C nuclear magnetic resonance spectrometry (13-16), UV-fluorescence spectroscopy (16), size exclusion chromatography (16), thin-layer chromatography (17, 18), atomic absorption spectrometry (19), gas chromatography coupled with mass spectrometry (20-22), and capillary electrophoresis (22) have been applied for determining the constituents of amber. The recently published results demonstrated clearly that FTIR and Raman spectroscopy are indispensable tools for the characterization and examination of works of art and archaeological materials (23-29) and amber as well (12, 22, 30-33).

It is well known that the famous Baltic amber is the largest group of fossil resins from Europe (34-36). However, no references about analysis of amber samples from different localities of Lithuania have been found in the bibliography. Therefore, in the present study, attention has been focused on the characterization of different amber samples found in Lithuania using FTIR spectroscopy, X-ray diffraction analysis (XRD) and scanning electron microscopy (SEM). The amber samples of the present investigation were collected at the Baltic Coast in Nida district and in two archaeological complexes (Turlojiškės and Benaičiai) located in different regions of Lithuania. A historical amber sample of unknown origin was found in Vilnius (Lithuania). The main aim of this study is to explore the potential of the above mentioned methods to assess the chemical, mineralogical and microstructural composition of different amber samples found in Lithuania. Secondly, in the present study, attention has also been focused on the preliminary development of sol-gel procedure for the preparation of protective coating to isolate amber from the air.

Experimental

Seven different amber samples collected in Lithuania were chosen for the characterization: (a) four amber samples having different physical appearance (milky

Fig. 1. Pictures of historical "unknown" amber sample.

(sample I), dark (sample II), opaque (sample III) and transparent (sample IV)) found in 2005 at the Baltic Coast in Nida, (b) two archaeological amber samples excavated in different archaeological complexes (villages Benaičiai (sample V) and Turlojiškės (sample VI)) and (c) historical unknown amber sample (Fig. 1) whose origin is not clear was provided by Lithuanian P. Gudynas Restoration Centre (Vilnius). This sample (sample VII) was found many years ago along with other valuable findings in old town of Vilnius.

The infrared (FTIR) spectra were recorded on a Perkin Elmer Spectrum BX FTIR spectrometer (USA). The amber samples were powdered in an agate mortar and mixed (~1.0 %) with dried KBr (Merck, Germany) and pressed into pellets. The following instrumental settings were used: transmission (%), range from 3700 to 500 cm^{-1}, 20 scans, resolution ±4 cm^{-1}, gain 1, scan speed 0.3 cm/s, temperature 25ºC. The press ENERPAC (Germany) was used to prepare the pellets. The amber samples were characterized by powder X-ray diffraction analysis (XRD) performed with a PANalytical X'Pert PRO powder diffractometer (The Netherlands) equipped with a conventional X-ray tube (CuKα$_1$ radiation, 40 kV, 30 mA) using Fe filter/monochromator and multichannel detector X'Celerator with an anti-scatter shield. The XRD patterns were measured in the range of 4 to 80 º 2θ with the step of 0.016711º and 30 s counting per step. The morphology and microstructure of amber samples (un-

coated and covered with sol-gel coatings) were examined by scanning electron microscopy (SEM) on JOEL 820 scanning electron microscope (Japan). To avoid charging, samples were lightly coated with Au/Pd.

Small pieces of transparent amber sample used in this study were coated by Y-Cu-O acetate-tartrate sol-gel coatings. The amber was crushed in an agate mortar (Carl Roth GmbH & Co, Germany) prior to the experiment. The sol solution was prepared by an acetate-tartrate sol-gel method (37). As starting compounds, stoichiometric amounts of Y_2O_3 (Aldrich Chemicals, Germany) and $Cu(CH_3COO)2 \times H_2O$ (Aldrich Chemicals, Germany) (molar ratio Y:Cu = 1:1), both of them analytical grade, were used. In the sol-gel process Y_2O_3 first was dissolved in 0.2 M acetic acid (Lachema, Czech Republic) at 55-60°C. Next, $Cu(CH_3COO)_2 \cdot H_2O$ dissolved in a small amount of distilled water was added with continuous stirring at the same temperature. The heating magnetic stirrer Monotherm Variomag (Germany) was used. The obtained solution was concentrated for about 8 hours at 60-65°C in an open beaker (SIMAX, Czech Republic). Under continuous stirring, the transparent blue Y-Cu-O acetate-tartrate gel was formed. The pieces of amber were treated in Y-Cu-O acetate-tartrate gel for several hours at room temperature. After further drying in an oven (Uteno Elektrotechnika Co, Lithuania) at 80°C, fine grained blue coatings on the surface of amber were obtained.

Results and Discussion

The FTIR spectra of four amber samples collected in 2005 at the coast of Baltic Sea in Nida are presented in Fig. 2. It is interesting to note that the spectra of all milky, dark, opaque and transparent amber samples were nearly the same, irrespective of the physical appearance of the sample. The spectra show the characteristic absorption bands of vibrations in a number of functional groups, such as OH, CH_2, CH_3, C=C, and –CO-O (12, 38, 39). These absorption bands are summarized in Table 1. A broad absorption in the spectra at around 3450 cm^{-1} indicates the presence of adsorbed water vapour during formation of amber (40-43). In the 1245-1175 cm^{-1} region, the FTIR spectra of the ambers from Baltic Coast contain broad and almost horizontal shoulder which is highly characteristic feature of the Baltic amber. Moreover, this shoulder is followed by a sharp absorption peak which reaches maximum intensity around 1160 cm^{-1}, attributed to the C-O stretch vibrations. The similarity of distinctive features observed in these FTIR spectra let us to conclude that the chemical composition of amber samples I-IV is very similar despite their physical appearance is different.

The FTIR spectra of two archaeological amber samples are presented in Fig. 3. The FTIR spectra of samples V and VI are very similar to previous ones, showing the definitive Baltic shoulder area. This fact let
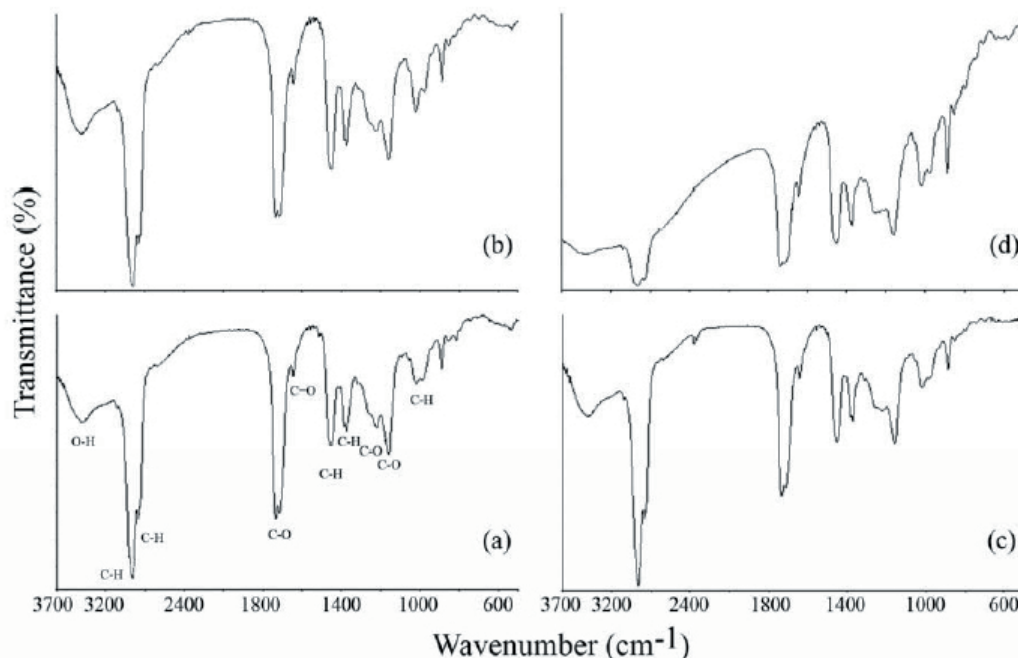

Fig. 2. FTIR spectra of milky (a), dark (b), opaque (c) and transparent (d) amber samples from Baltic Coast in Nida.
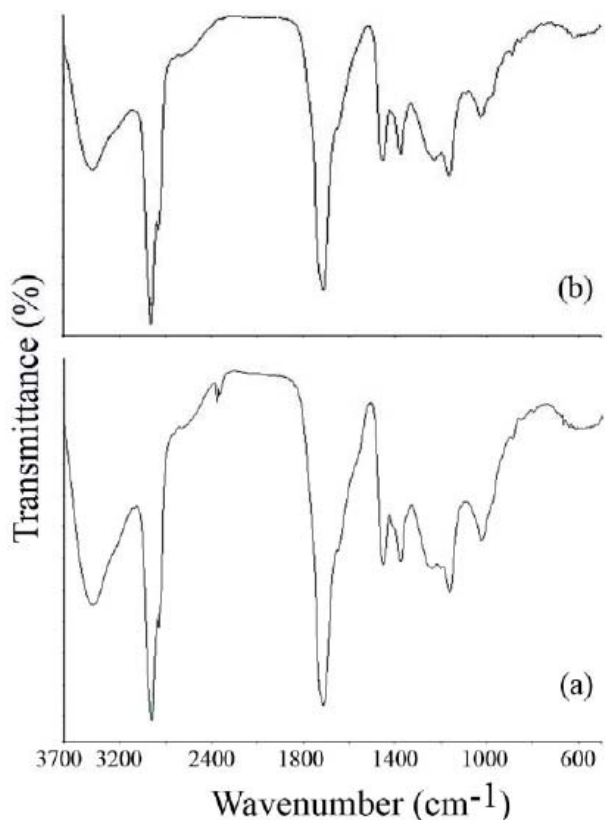
Fig. 3. FTIR spectra of archaeological amber samples from villages Benaičiai (a) and Turlojiškės (b).

us to predict that these amber samples also belong to the Baltic amber group. Especially well resolved horizontal shoulder could be detected in the FTIR spectrum of the amber from the archaeological complex of Benaičiai (see Fig. 3, a). A negligible change in the slope of the shoulder between 1245 and 1175 cm⁻¹ can be seen in the FTIR spectrum of the amber from the archaeological complex of Turlojiškės (see Fig. 3, b). This could be associated with the oxidative degradation of amber (10). According to the origin of FTIR spectra of amber samples presented in Figs. 2 and 3, it is possible to state that the archaeological amber samples are "domestic(ally)" formed near the Baltic Sea, but not shipped from somewhere. It is necessary to note that the methodology of characterization can not be used if the historic samples contain other materials with FTIR interfering substances.

The main characteristic Baltic amber features are also evident in the FTIR spectrum of historical "unknown" amber sample found in old town of Vilnius (Fig. 4). The positions of all peaks observed in this FTIR spectrum fit exactly with the results presented in Table 1. Therefore, once again we can draw a similar conclusion that sample VII also belongs to the same Baltic amber group.

Buchberger *et al.* (22) used capillary electrophoresis to determine that Baltic amber inclusion droplets contain water in which a variety of inorganic cations (Na^+, K^+, Ca^{2+}, Mg^{2+}) and anions (Cl^-, Br^-, NO_3^-, SO_4^{2-}) may be dissolved. Accordingly, the crystallization of inorganic salts during formation of amber can also occur. Therefore, all seven amber samples were examined by powder XRD analysis. The XRD patterns of amber samples I-IV are presented in Fig. 5. As was expected, the X-ray diffraction patterns of amber specimens exhibited amorphous character. All four XRD patterns indicate an unidentified amorphous humps between $2\theta = 10$–$25°$, reaching maximum height at around 18°. No peak corresponding to what would have been characteristic of metal salts crystallization could be detected in any of the XRD patterns. On the other hand, the XRD pattern of milky amber (sample I) (see Fig. 5, a) contains rather sharp and intensive peak at around $2\theta \approx 32.0°$. Surprisingly, this diffraction peak is the most intensive diffraction line for the quartz (SiO_2) phase [PDF 46-1045]. These results suggest that during formation of amber the small amount of silica is trapped inside amber.

The XRD patterns of two archaeological amber samples are shown in Fig. 6. As seen, these samples are essentially amorphous as well. Again, no peaks attributable to the metal salts or unknown contaminating phase in the XRD patterns of the samples V and VI could be identified. Both XRD patterns contain the same diffraction line at $2\theta \approx 32.0°$. Apparently, the sample VI contains a higher amount of SiO_2 phase.

The presence of large amount of quartz phase in the sample VII was determined as well. The X-ray diffraction pattern for the amber sample VII is shown in Fig. 7. The three most intensive peaks of quartz phase at 2θ values of 32.0°, 24.3° and 49.9° are present in the XRD pattern of analyzed amber sample. From XRD analysis, we concluded for the first time that during the formation process, the Baltic amber in some cases can accumulate the SiO_2 phase.

The main absorptions (1160, 1082 and 512 cm⁻¹) from the quartz phase (Si-O) could be also easily identified by FTIR spectroscopy (26, 44). However, in the FTIR spectra of amber samples, namely in this region there are very well resolved several bands characteristic for succinates (12). Consequently, the absorptions from the quartz phase (Si-O) are overlapped with absorption peaks originating from C-O vibrations. Thus, FTIR spectroscopy can be effectively employed for the characterization of amber, and very useful additional information was obtained by only using the results from the XRD measurements.

Table 1. The main absorption frequencies of the milky, dark, opaque and transparent amber samples from Baltic Coast (Lithuania) in the 3700-500 cm-1 range.

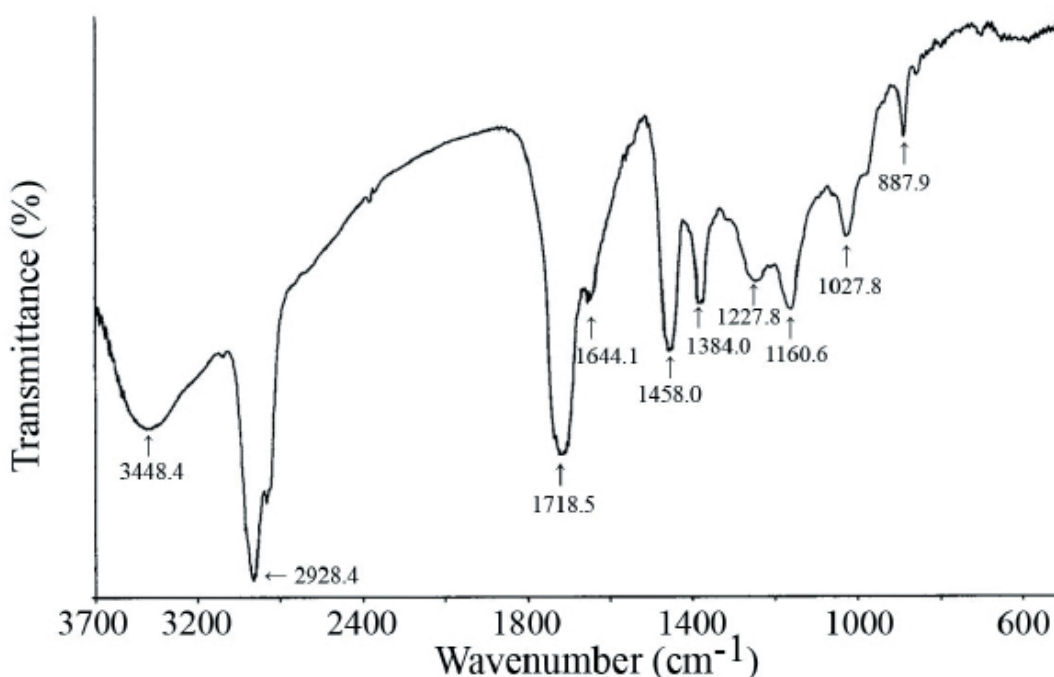| Group	Band, cm^{-1}	Remarks
-O-H	3500-3400	O-H stretching, broad
>CH$_2$, –CH$_3$ and -CH$_2$-	2940-2840	C–H stretching, strong
	1460-1445	C–H deformations, medium
	1380-1370	C–H bending, medium
	889-887	C–H out of plane bending of H atoms, medium
-CO-O-	1740-1700	C=O, strong
	1245-1010	C-O bonds, characteristic for succinate, medium
C=C	1650-1640	C=C stretch, weak

Fig. 4. FTIR spectrum of historical "unknown" amber sample found in old town of Vilnius.

The textural properties of the amber samples were investigated by SEM, from which the typical morphologies were obtained. It is interesting to note that almost identical microstructure was observed for all seven amber samples irrespective of their origin. Scanning electron micrograph of the representative historical amber sample is shown in Fig. 8. Evidently, the surface of amber is exceptionally smooth, however, it contains many prolonged cracks. The inclusion spherical and ellipsoidal droplets 1-3 μm in size can also be clearly seen.

As was already mentioned, it is very important that the amber collections be preserved for future study and enjoyment (12). In this study, a sol-gel method has been suggested for the fabrication of coatings for the protec-

tion of degradation of amber. The amber sample IV has been chosen for the preliminary investigations. This transparent amber was crushed in an agate mortar prior experiment. The obtained small pieces of amber were coated by dipping with Y-Cu-O acetate-tartrate gels. Both amber samples, untreated and sol-gel coated were examined by SEM. Fig. 9 shows the surface features of the powdered amber sample before sol-gel processing. As seen after crushing the monolithic surface, it is composed of individual particles with no regular shape. It can be seen from Fig. 9 that the amber solids are composed of volumetric plate-like grains coexisting with spherically shaped particles. Two scanning electron micrographs from the different areas of the sol-gel treated and dried
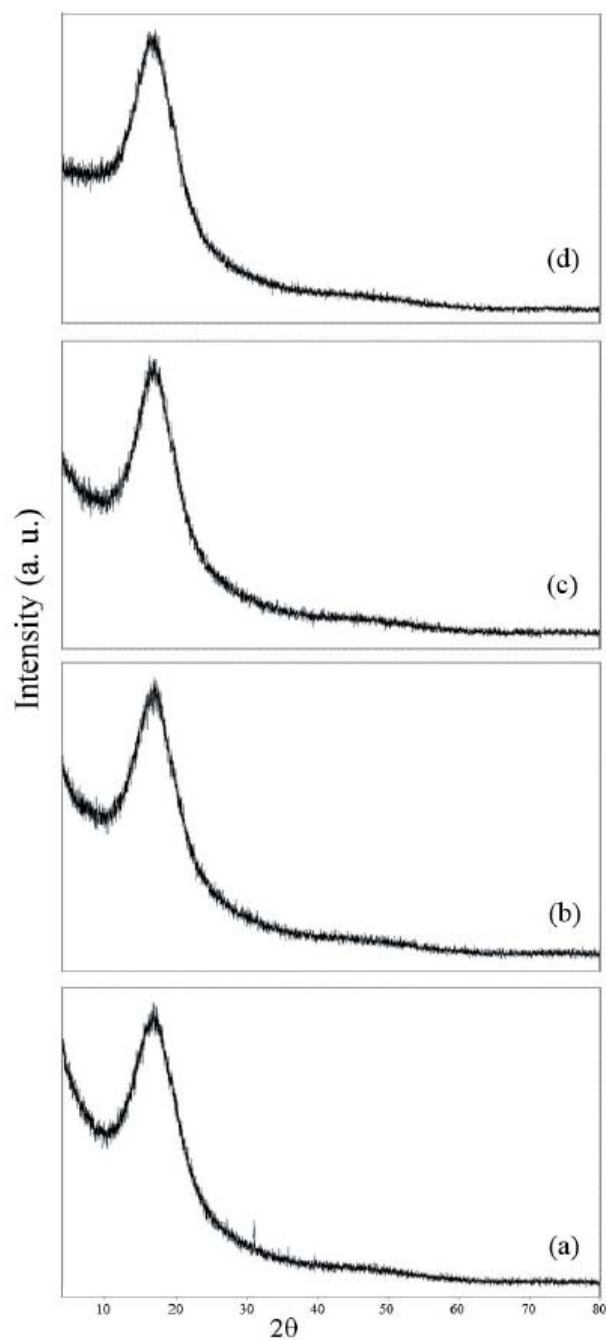
Fig. 5. XRD patterns of milky (a), dark (b), opaque (c) and transparent (d) amber samples from Baltic Coast in Nida.
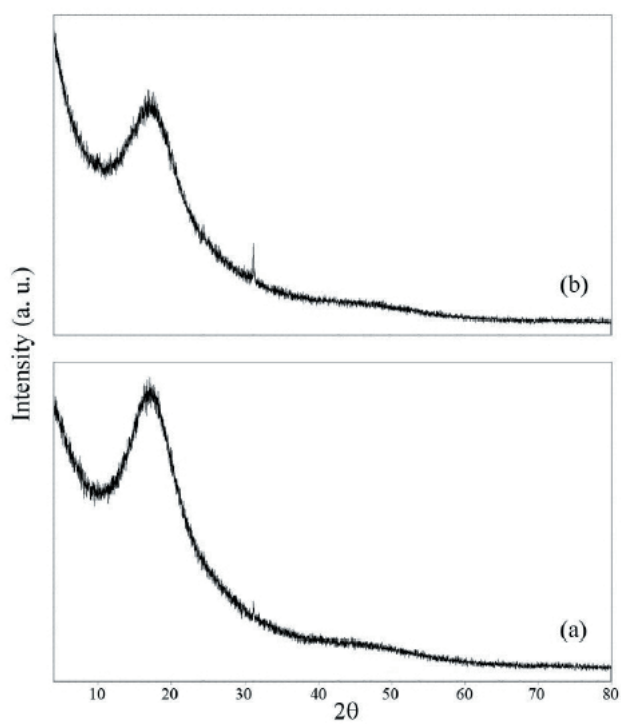

Fig. 6. XRD patterns of archaeological amber samples from villages Benaičiai (a) and Turlojiškės (b).
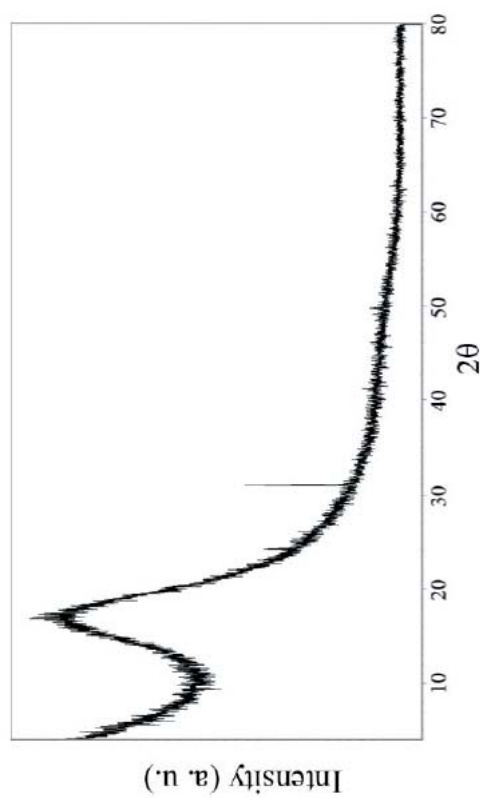

Fig. 7. XRD pattern of historical "unknown" amber sample found in old town of Vilnius.
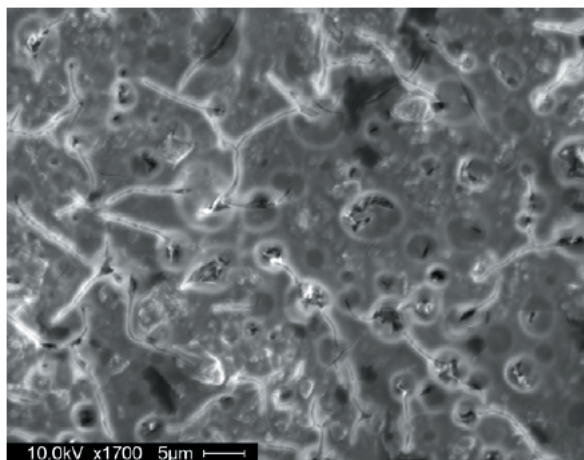
Fig. 8. SEM micrograph of historical "unknown" amber. Magnification 1700×.

amber samples are also shown in Fig. 9. A progressive change in morphology after sol-gel treatment is evident. It is apparent that dense Y-Ba-O gel networks are formed on the surface of amber, giving it a glassy-like envelope with no internal porosity. The micrographs presented in Fig. 9 also show that the formation led to uniform and smooth surfaces which are composed of highly agglomerated polymeric gel particles. Therefore, the proposed sol-gel technique appears to be very attractive way to make high density and homogeneous protective coatings on the surface of amber. However, to answer whether or not the proposed sol-gel treatment is suitable for the conservation of amber, the answer will be given in future after more detailed investigations.

Conclusions

For the first time the amber samples from different localities of Lithuania were investigated and characterized by FTIR, XRD and SEM techniques. The amber samples of the present investigation were collected at the Baltic Coast in Nida district, in two archaeological complexes located in different regions of Lithuania, and obtained at the Lithuanian P. Gudynas Restoration Centre. The FTIR results showed that all the ambers analyzed here fall into a common class of fossil resin, Baltic ambers, independent of the sample location in Lithuania. The XRD results revealed that in some samples the small amount of quartz is trapped inside amber. Such observation has not been previously reported in the bibliography. The textural properties of the amber samples were investigated by SEM, from which the typical morphologies were obtained. The surface of amber was found to be exceptionally smooth, however,
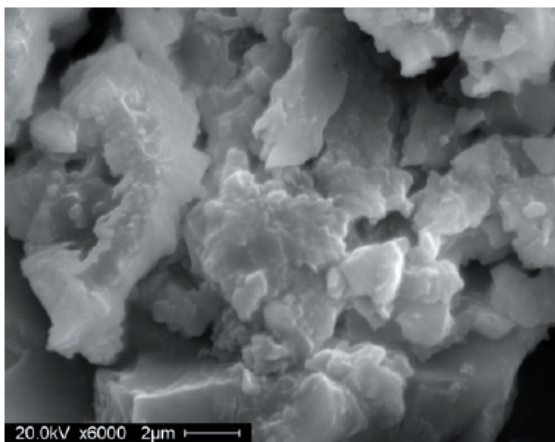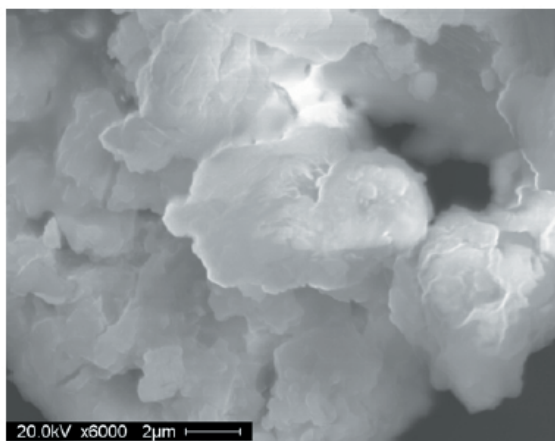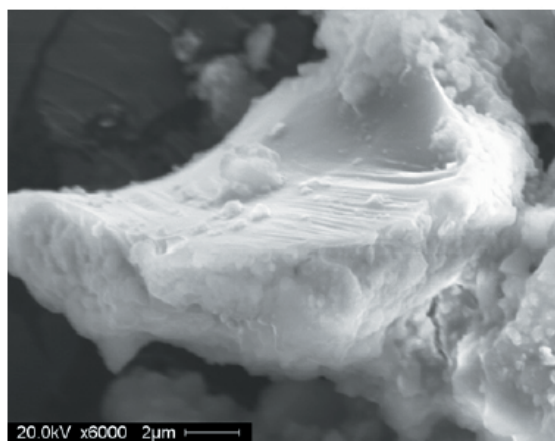

Fig. 9. SEM micrograph of crushed transparent amber sample from Baltic Coast in Nida (at bottom) and different SEM areas of sol-gel coated amber sample (at middle and top). Magnification 6000×.

contained many prolonged cracks. Additionally, we proposed a novel aqueous sol-gel technique which appears to be very attractive way to make protective coatings on the surface of amber.

References

1. K. Kaiserling, *Pathologe*, **22**, 285 (2001).
2. G. Cadier-Rey, *Historia*, **673**, 87 (2003).
3. O. Zompro, *Deutsche Entomolog. Zeits.*, **52**, 251 (2005).
4. G. O. Poinar, *Experientia*, **50**, 536 (1994).
5. H. Choe, M. Farzan, *Nature Biotech.*, **24**, 1361 (2006).
6. J. Wunderlich, *Zootaxa*, **1325**, 313 (2006).
7. C. O. Coleman, *Organisms Divers. Evol.*, **6**, 103 (2006).
8. H. Dorfelt, A. R. Schmidt, *Palaeontology*, **49**, 1013 (2006).
9. J. Waddington, J. Fenn, *Collec. Forum*, **4**, 25 (1988).
10. R. S. Williams, J. B. Waddington, J. Fenn, *Collec. Forum*, **6**, 65 (1990).
11. D. Thickett, P. Cruickshank, C. Ward, *Stud. Conserv.*, **40**, 217 (1995).
12. Y. Shashoua, M. B. L. D. Berthelsen, O. F. Nielsen, *J. Raman Spectr.*, **37**, 1221 (2006).
13. F. Czechowski, B. R. T. Simoneit, M. Sachanbinski, J. Chojcan, S. Wolowiec, *Appl. Geochem.*, **11**, 811 (1996).
14. A. Martinez-Richa, R. Vera-Graziano, A. Rivera, P. Joseph-Nathan, *Polymer*, **41**, 743 (2000).
15. J. B. Lambert, G. O. Poinar, *Accounts Chem. Res.*, **35**, 628 (2002).
16. C. A. Islas, I. Suelves, J. F. Carter, A. A. Herod, R. Kandyoti, *Rapid Comm. Mass Spectr.*, **15**, 845 (2001).
17. A. Matuszewska, L. Krawowski, *J. Planar Chromatogr.*, **13**, 140 (2000).
18. A. Matuszewska, A. John, *Acta Chromat.*, **14**, 82 (2004).
19. S. Z. Chen, D. B. Lu, *Spectrosc. Spectr. Anal.*, **26**, 1928 (2006).
20. A. M. Shedrinsky, D. A. Grimaldi, J. J. Boon, N. S. Baer, *J. Anal. Appl. Pyrol.*, **25**, 77 (1993).
21. E. C. Stout, C. W. Beck, K. B. Anderson, *Phys. Chem. Miner.*, **27**, 665 (2000).
22. W. Buchberger, H. Falk, M. U. Katzmayr, A. E. Richter, *Monatsh. Chemie*, **128**, 177 (1997).
23. S. Bruni, F. Cariati, F. Casadio, L. Toniolo, *Vibr. Spectrosc.*, **20**, 15 (1999).
24. P. Calvini, A. Gorassini, *Restaurator*, **23**, 48 (2002).
25. B. Havlinova, D. Babiakova, V. Brezova, M. Durovic, M. Novotna, F. Belanyi, *Dyes Pigm.*, **54**, 173 (2002).
26. G. E. De Benedetto, R. Laviano, L. Sabbatini, P. G. Zambonin, *J. Cult. Herit.*, **3**, 177 (2002).
27. J. Senvaitiene, A. Beganskiene, A. Kareiva, *Vibr. Spectrosc.*, **37**, 61 (2005).
28. J. Kiuberis, S. Tautkus, R. Kazlauskas, I. Pakutinskiene, A. Kareiva, *J. Cult. Herit.*, **6**, 245 (2005).
29. M. R. Derrick, D. Stulik, J. M. Landry, Infrared spectroscopy in conservation science, The Getty Conservation Institute, Los Angeles, 1999.
30. A. Golloch, S. Heidbreder, C. Luhr, *Fresen. J. Anal. Chem.*, **361**, 545 (1998).
31. D. Gold, B. Hazen, W. G. Miller, *Organ. Geochem.*, **30**, 971 (1999).
32. Y. M. Moreno, D. H. Christensen, O. F. Nielsen, *Asian J. Spectrosc.*, **4**, 49 (2000).
33. J. Jehlicka, S. E. J. Villar, H. G. M. Edwards, *J. Raman Spectrosc.*, **35**, 761 (2004).
34. W. Starega, *Annal. Zoologici*, **52**, 601 (2002).
35. I. Angelini, P. Bellintani, *Archaeometry*, **47**, 441 (2005).
36. G. Dlussky, A. Radchenko, Acta Palaeont. *Polonica*, **51**, 561 (2006).
37. S. Mathur, H. Shen, N. Lecerf, M. H. Jilavi, V. Cauniene, J.-E. Jørgensen, A. Kareiva, *J. Sol-Gel Sci. Technol.*, **24**, 57 (2002).
38. K. Nakanishi, Infrared Absorption Spectroscopy, Holden Day, San Francisco, 1977.
39. Infrared and Raman Spectroscopy: Methods and Applications / Ed. by B. Schrader, VCH, Weinheim, 1995.
40. C. Beck, *Archaeometry*, **8**, 96 (1965).
41. A. J. Ross, *Geology Today*, **1-2**, 24 (1997).
42. D. Keyser, W. Weitschat, *Hydrobiologia*, **538**, 107 (2005).
43. D. Penney, *Biologist*, **53**, 247 (2006).
44. K. Nakamoto, Infrared and Raman Spectra of Inorganic and Coordination Compounds, John Wiley and Sons, New York, 1986.

Determination of insecticide monosultap residues in tomato and soil by capillary gas chromatography with flame photometric detection

Chuan-Jiang Tao, Ji-Ye Hu*, and Jian-Zhong Li

Research Center for Eco-Environmental Sciences, Chinese Academy of Sciences, Beijing, 100085, People's Republic of China

Abstract

A residue analysis method for the determination of monosultap in soil and tomato was developed. Samples were extracted with deionized water, derivatized in a single-step procedure of hydrolysis under alkaline condition (monosultap was converted to nereistoxin) and then cleanup by liquid-liquid partition. The tomato sample was further prepared by dispersive solid-phase extraction (dispersive-SPE) with primary secondary amine (PSA) as the sorbent. The residues were reconstituted in ethyl acetate and then determined by gas chromatography with a flame photometric detector (FPD-S). The results were further confirmed by gas chromatography-mass spectrometry (GC-MS). The limit of quantification was demonstrated to be as low as 0.01 mg/kg for the pesticide. The mean recoveries from soil and tomato ranged from 86.5 to 101.7 % with average relative standard deviation (R.S.D) ranging from 0.49 to 10.0 %. The method was applied to determine the fate of monosultap in soil and tomato. Data have shown that the disappearance rates on soil and tomato were described as pseudo-first-order kinetics and the half-life ($t_{1/2}$) was less than 2 days.

Keywords*: monosultap, tomato and soil, residue analysis, GC-FPD-S*

Résumé

Nous avons développé une méthode résiduelle pour la détermination du monosultap dans les sols et les tomates. Les échantillons sont d'abord extraits par l'eau déionisée, dérivatisés dans une étape unique d'hydrolyse sous condition alcaline (le monosultap a été converti en néréistoxine) et le tout a été complété par une étape de nettoyage en partition liquide liquide. Les échantillons de tomates ont été purifiés davantage par extraction dispersive en phase solide (dispersive-SPE) avec une amine primaire secondaire (PSA) comme sorbant. Les résidus ont été reconstitués dans l'acétate d'éthyle et déterminés par chromatographie en phase gazeuse couplée à un détecteur en photométrie de flamme (FPD-S). Les résultats ont été confirmés par chromatographie en phase gazeuse – spectrométrie de masse (GC-MS). Nous avons pu démontré une limite de quantification aussi basse que 0.01 mg/kg pour le pesticide. Les moyennes de recouvrement pour les sols et les tomates se situaient entre 86.5 et 101.7 %, avec des écarts types relatifs (R.S.D) se situant entre 0.49 et 10.0 %. La méthode a été appliquée pour déterminer le comportement du monosultap dans le sol et la tomate. Les données ont montré que les taux de disparition dans le sol et la tomate étaient décrits par des cinétiques de pseudo premier ordre et des temps de demi-vie ($t_{1/2}$) inférieurs à 2 jours.

Introduction

Nereistoxin (NTX) is a naturally occurring insecticidal substance isolated from the marine segmented worms, *Lumbriconereis heteropoda* [1]. Its structure was elucidated by Okaichi and Hashimoto in 1962 [2] and synthesized in 1968 by Hagiwara *et al* [3]. A variety of nereistoxin derivatives have been known for decades, including thiocyclam, cartap, bensultap, and monosultap etc. They generally are stomach poisons with some contact action and often show some systemic action, and

tend to be selectively active on *Lepidoptera*, *Coleoptera* and *diptera* insect pests [4]. The development and use of monosultap (2-N, N-dimethylanino-1-sodium-thio-sulphate-3-thiosulphate propane) (Figure 1) has taken place in China since 1970s, and is now widely used in various applications for crop control. There has been increased awareness in recent years about the residues of pesticide in crops and environmental matrices where the risk they may pose has to be controlled. Little work has been found in the literature on the residue analysis of monosultap in the environmental samples. Z.T. Zhang, *et al.* [5] reported a method for determination monosultap in paddy soil and rice plant, which concerned a laborious cleaning up procedure and dangerous reagent of ether. The main objective of this work was to develop a simple and sensitive method for the determination of monosultap in soil and tomato. The developed method was applied to determine the pesticide levels in the soil and tomato samples collected from the trial field. There has been no MRL (Maximum Residue Limit) of monosultap set by Chinese legislation or FAO (Food and Agriculture Organization)/WHO (World Health Organization) yet, while MRLs of the analogues of it such as thiocyclam, cartap and bensultap have been set to 0.1 to 25 mg/kg for crops and vegetables by various countries [6]. According to the analogues MRLs, the quantification limit of 0.01 mg/kg was suitable for residue analysis of monosultap in samples.

Experimental

Chemicals

Analytical grade monosultap (99.9%) and 16% monosultap EC (trade name Kuaijian) were supplied by the manufacturer of China. Analytical grade n-hexane, ethyl acetate, hydrochloric acid, sodium hydroxide, sodium chloride, anhydrous sodium sulfate and sodium sulfuration were purchased locally. Dispersive solid phase extraction (SPE) sorbents or SPE cartridges such as C_{18}, Florisil and primary secondary amine (PSA) were used.

Gas Chromatography System

A gas chromatograph, VARIAN CP 3800, equipped with a capillary column (Supelco equity-5, 30 m × 0.25 mm ID, 0.25 µm thickness film) a flame photometric detector (FPD-S) was employed. The chromatographic conditions used for the analysis of the derivatization product of monosultap residues were as follows: detector temperature, 300°C; injector temperature, 250°C; oven temperature program, 0.5 min at 50°C, 50°C to 120°C (30°C/min, hold 1 min), 120°C to 220°C, (15°C/min, hold for 3min). The injection volume was 2 µL. N_2 was used as the carrier gas, maintained at a constant flow rate of 1 mL/min. The approximate retention time of the monosultap-derivatization (nereistoxin) was 6.9 min.

GC-MS System

Confirmatory analysis of the derivatization product of monosultap was done on a Varian CP-3800 with a mass selective ion detector and a capillary column (Supelco
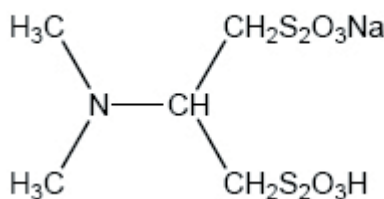

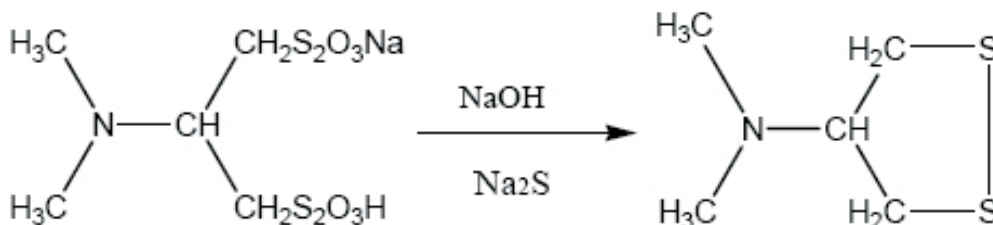
Figure 1. Chemical structure of monosultap

Figure 2. The derivatization process of monosultap

equity-5, 30 m × 0.25 mm ID, 0.25 μm thickness film). The column temperature was set at 60°C for 0.5 min, and then it was programmed to heat from 60°C to 120°C at 30°C/min (hold 1min), from 120°C to 220°C at 15°C/min (hold 3 min). The temperature of the injection was set at 250°C. Splitless injection mode was used. The carrier gas was helium, and its flow rate was set at 1 mL/mim. The mass spectrometer was operated in electron ionization mode with impact ionization voltage 70 eV, a transfer line temperature of 260°C, trap temperature of 180°C, manifold temperature of 80°C, and electron multiplier voltage 1950 V. The acquisition was performed in scan mode in the ranges m/z 40-200.

Standard preparation

For long-term storage, a stock solution (500 μg/mL) of monosultap was prepared in distilled water. Working calibration solutions of 0.1, 0.3, 0.6, 3.0, 4.4 and 30 μg/mL were made by serial dilutions. Working solutions between 0.1 and 30μg/mL were suitable for recovery assay and dissipation study. The derivatization procedures were performed as described for the samples.

Extraction

A 20 g sample of soil or tomato homogenized was extracted with 60 mL distilled water by shaking thoroughly in a conical flask for 1 h on a mechanical horizontal shaker, and then extracted once again with 20 mL distilled water. After centrifuged for 15 min at 5000 rpm, the supernatant from extraction was combined and transferred quantitatively to a 250 mL screw-cap bottle.

Derivatization

3.0 g NaCl was added to the 250 mL screw-up bottle above, and shaken for 10 min. The pH was adjusted to pH 8.5-9.0 with 0.1M NaOH, and 1mL 0.1M Na_2S was also added as catalyzer. The mixture was then held for 3 h in a water bath at 70ºC for derivatization. After derivatizated, the mixture was then cooled down to room temperature for further clean-up.

Clean-up

The mixture of derivatization was transferred to a 500-mL separatory funnel, the monosultap-derivatization was partitioned into n-hexane (3×30 mL). Soil samples were as follow: the n-hexane layer was separated, combined, dehydrated through anhydrous sodium sulfate, concentrated to 1-2 mL in rotary evaporator below 40ºC, and completely dried under a nitrogen purge. The residue was reconstituted in ethyl acetate for GC analysis. The

procedures for preparing the tomato samples were: the combined n-hexane layer was concentrated to about 20 mL on the rotary evaporator, and transferred into centrifuge tube containing 300 mg PSA sorbent. The tube was vortexed and then centrifuged for 5 min at 4800 rpm to separate the solution from solid. The separated solution was dehydrated through anhydrous sodium sulfate, and followed the procedures as the above soil sample.

Recovery assay

Samples of untreated soil and tomatoes were fortified with monosultap standard solutions to reach concentration of 0.01, 0.05, 0.5 and 2 mg/kg. Prior to the extraction step, the fortified samples were allowed to settle for 30 min. Afterward, they were processed according to the above extraction procedure. Three replicates for each concentration were analyzed.

Field Trials

The trial site was an experimental tomato greenhouse located at Xiaotangshang district of Beijing (China). A random block scheme was used with three replications for each test; each block was 30 m². Treatments were carried out with a portable motor sprayer using the commercial formulation of Kuaijian (16% monosultap EC). During the whole trial the average minimum/maximum daily air temperatures were 19.5/39.5ºC,the average relative humidity was 85.2%, the average solar radiation was 12.3 kWh m^{-2} day^{-1}.

Tomato plants were sprayed in three replicates with monosultap (Kuaijian) at the recommended two dosages by the manufacturer: 180 g of active ingredient per hectare (low dosage) and 360 g of active ingredient per hectare (high dosage), which were diluted with 3000-4000 fold water. Before the treatments, samples of tomato with the same ripening stage, size and shape were localized and tagged. Tomato samples were collected at random from sampling plots at 0 (1 h after spraying), 1, 2, 3, 5, 7, 10 and 15 days after the treatments. Immediately after picking, the samples were put into polyethylene bags and transported to the laboratory where they were chopped, thoroughly mixed, and divided into three sub-samples each. The sub-samples were kept deep-frozen (-30 ºC) until analysis.

Soil samples were collected from directly beneath the treated tomato plant canopy at surface and from different depths ranging from 0 to 20 cm with an Auger tube. The soil samples were collected at 0 (1 h after spraying), 1, 2, 3, 5, 7, 10 and 15 days after spraying. Control samples were obtained from the soil under the control plots.

Results and Discussion

Optimization of the derivatization reaction

Derivatization is often used in GC to increase the volatility of an analyte, to improve its thermal stability and to enhance the sensitivity or selectivity of the detection [7]. Due to its physical chemical properties such as thermal instability and polarity, monosultap is impossible to be analyzed using GC technique without the process of derivatization. HPLC-UV was also unsuitable for determination of monosultap at its residue levels owing to its weak UV absorbance.

The derivatization procedure was based on the principle proposed by Konosho in 1970 [8]. The procedure was optimized using an experimental design approach. Four variables were included in the preliminary experimental design: the amount of the reagents, the reaction temperature, pH, and the reaction time. The chromatographic responses revealed different behavior of the reaction conditions to the yields of the pesticide. The optimum reaction conditions were: under alkaline condition (pH=8-9) , the presence of 0.1 M Na_2S solution (1mL) as catalyzer, three hours reaction time, and 70ºC temperature incubation. Under these conditions, monosultap was converted into nereistoxin producing the highest yields, which was suitable for GC analysis.

And from the GC-MS results, it was concluded that the derivatization was achieved perfectly as expected. The derivatization process is illustrated in Figure 2.

GC-MS was used to verify whether the derivatization proceeded as expected or not. The results are shown in Figures 3 and 4, which confirm the structure of the generated derivative. The monosultap was converted into nereistoxin which has a molecular mass of m/z 149. Its mass spectrum shows a molecular ion at 149 and an ion of strong intensity at m/z 70 which is caused by a loss of S_2CH_3 (149-79).

Cleanup procedure

In order to improve the selectivity and reproducibility of the method, cleanup procedures were implemented after the derivatization process. For soil sample, liquid-liquid partition was employed to separate the pesticide using n-hexane, which gave good recoveries and little interference in the chromatogram and did not need further purification. As for tomato, additional cleanup procedure was required after liquid-liquid partition by n-hexane. Different sorbents were tested for SPE or dispersed SPE, such as Florisil, C_{18} and PSA. Poor recoveries were achieved (< 50%) using Florisil and C_{18} cartridges. Best results were obtained using dispersed PSA, which was thus chosen for all subsequent assays. Dispersed
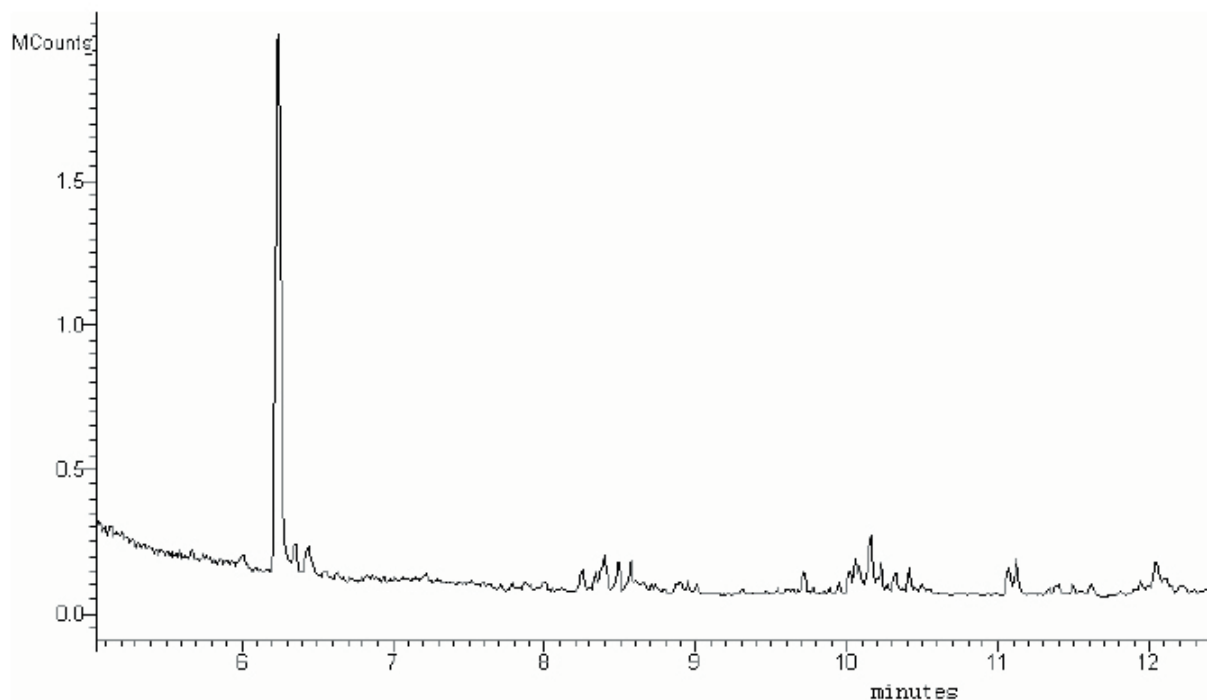

Figure 3. The total ion chromatography (TIC) of the generated derivative (nereistoxin)
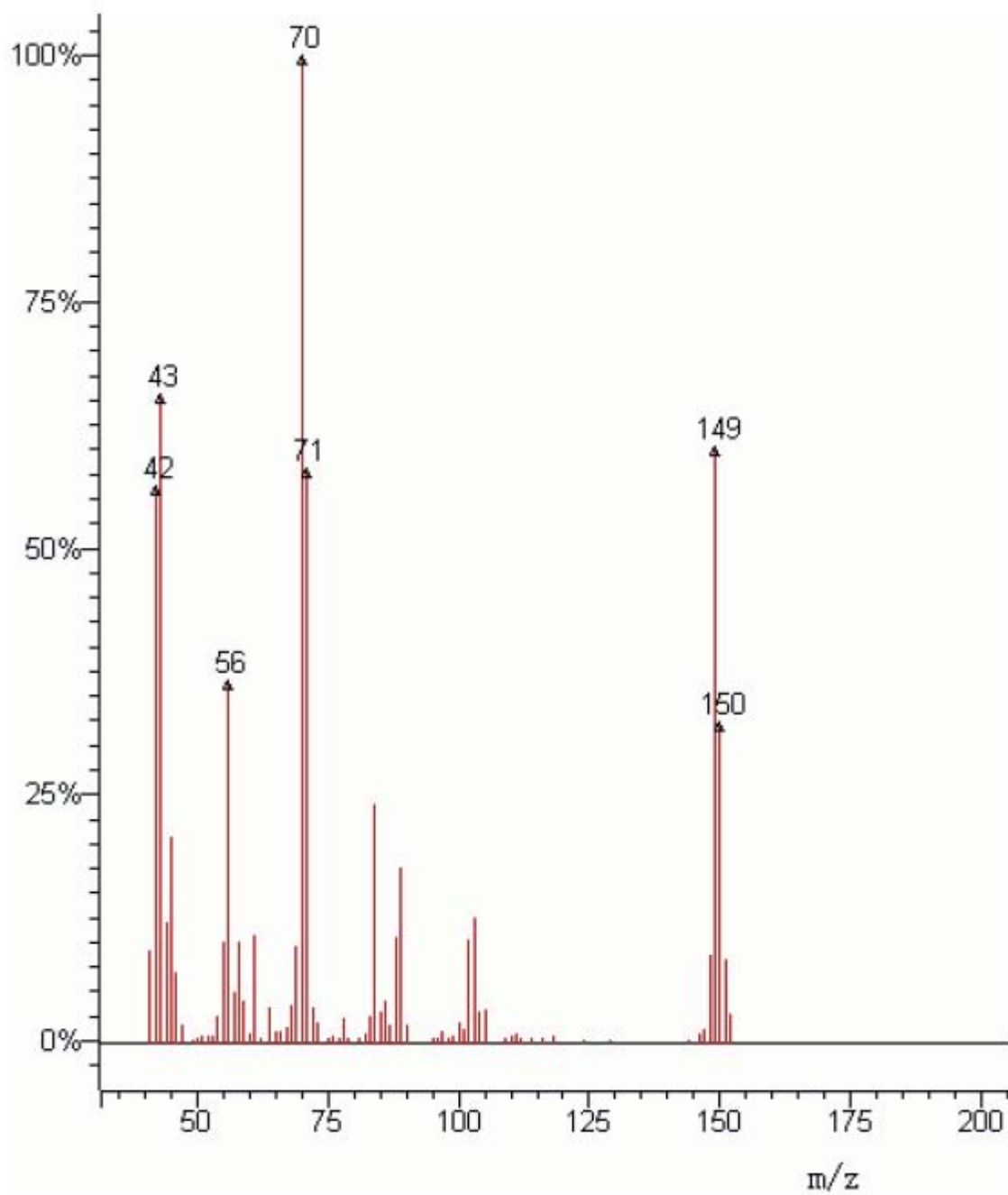
Figure 4. Gas chromatography-mass spectrum of the derivatization product of monosultap (nereistoxin)

PSA has allowed to obtain very high extraction yields (>95%) and good selectivity (no interference from the endogenous matrix).

Validation of the method

   Linearity. Quantification was accomplished by using standard curves constructed by plotting corresponding analyte concentrations against peak areas under proposed chromatographic conditions. A good linearity was achieved from 0.1 to 30 μg/mL with $R^2 = 0.9999$. The standard curve equation was $y = 47711x+5349.9$. The FPD chemilumenscent emission for sulfur-containing compound is dominated by S_2^*, resulting in a quadratic response. However, the software available for Varian usually provides linear response in relation to the dose. Corrections are not necessary.

   Accuracy, repeatability and sensitivity. The recoveries of monosultap from soil and tomato samples were investigated at concentrations of 0.01, 0.1, 0.5 and 2 mg/kg by using the prescribed procedure. The mean recoveries of monosultap from the samples ranged from 86.5 to 101.7 %, at four levels, as shown in Table 1. The

average relative standard deviation (R.S.D) was within 10.0 % at the four levels, and the lowest quantitation limit of monosultap in samples was 0.01 mg/kg, which was calculated using a signal-to-noise ratio of 10 (S/N = 10). Figure 5 shows the chromatograms of monosultap spiked and blank samples.

Dissipation studies in field experiment

   The proposed methodology was applied to a dissipation study of the pesticide monosultap after its application in an experimental greenhouse of tomatoes. The decrease in residue levels during the days after treatments is presented in Table 2. Figures 6 and 7 represent the dissipation rates of mososultap at recommended dosages. The monosultap in the field-treated samples after derivatization was also identified by the specific ions in the GC/MS analysis under the same conditions described above.

   Monosultap residues in tomato. The dissipation of monosultap residues with time was found to be described mathematically by a pseudo-first rate equation .The regression line equation for the concentration (C)

Table1. The recoveries of monosultap in tomato and soil (n = 3)

Spiked concentration, mg/kg	Recoveries, % tomato	RSD%	Recoveries, % soil	RSD %
0.01	86.5	10.0	101.7	9.8
0.05	97.4	2.58	99.8	2.60
0.1	91.3	2.02	95.2	1.28
2	98.2	1.01	97.2	0.49

Table 2. Monosultap residues in tomato and soil at different time intervals

Time elapsed after treatment in days	monosultap residues, mg/kg							
	soil				tomato			
	Trt. 1[a]	RSD, %	Trt. 2[b]	RSD, %	Trt. 1[a]	RSD, %	Trt. 2[b]	RSD, %
0	0.68	1.29	0.72	3.21	0.98	1.08	1.10	2.32
1	0.36	6.40	0.43	4.50	0.52	1.58	0.92	1.97
2	0.21	2.51	0.25	1.97	0.38	3.67	0.85	8.53
3	0.15	9.01	0.18	5.04	0.25	2.60	0.44	9.01
5	0.090	7.92	0.14	6.26	0.12	4.29	0.37	11.7
7	0.010	7.02	0.10	5.27	0.020	9.98	0.067	8.25
10	BDL[c]	--	0.010	9.48	BDL[c]	--	0.010	13.7
15	BDL[c]	--	BDL[c]	--	BDL[c]	--	BDL[c]	--

[a] Trt.1: Treatment #1 - 180 (*a.c.*) g/ha
[b] Trt.2: Treatment #2 - 360 (*a.c.*) g/ha
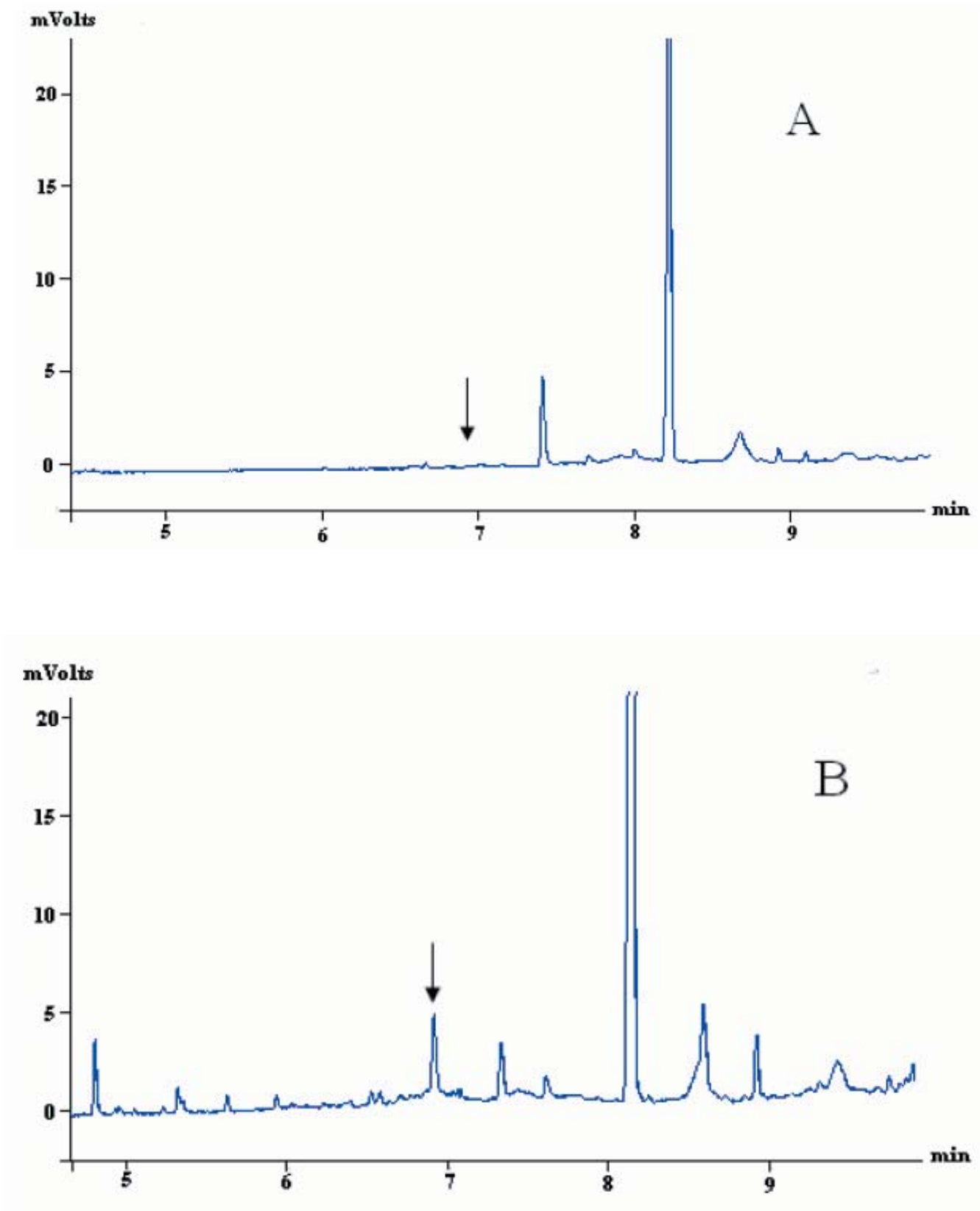[c] BDL: Below determination limit

Figure 5. Chromatograms of monosultap spiked and blank samples. (A) control tomato sample (B) fortified tomato at 0.1 mg /kg.
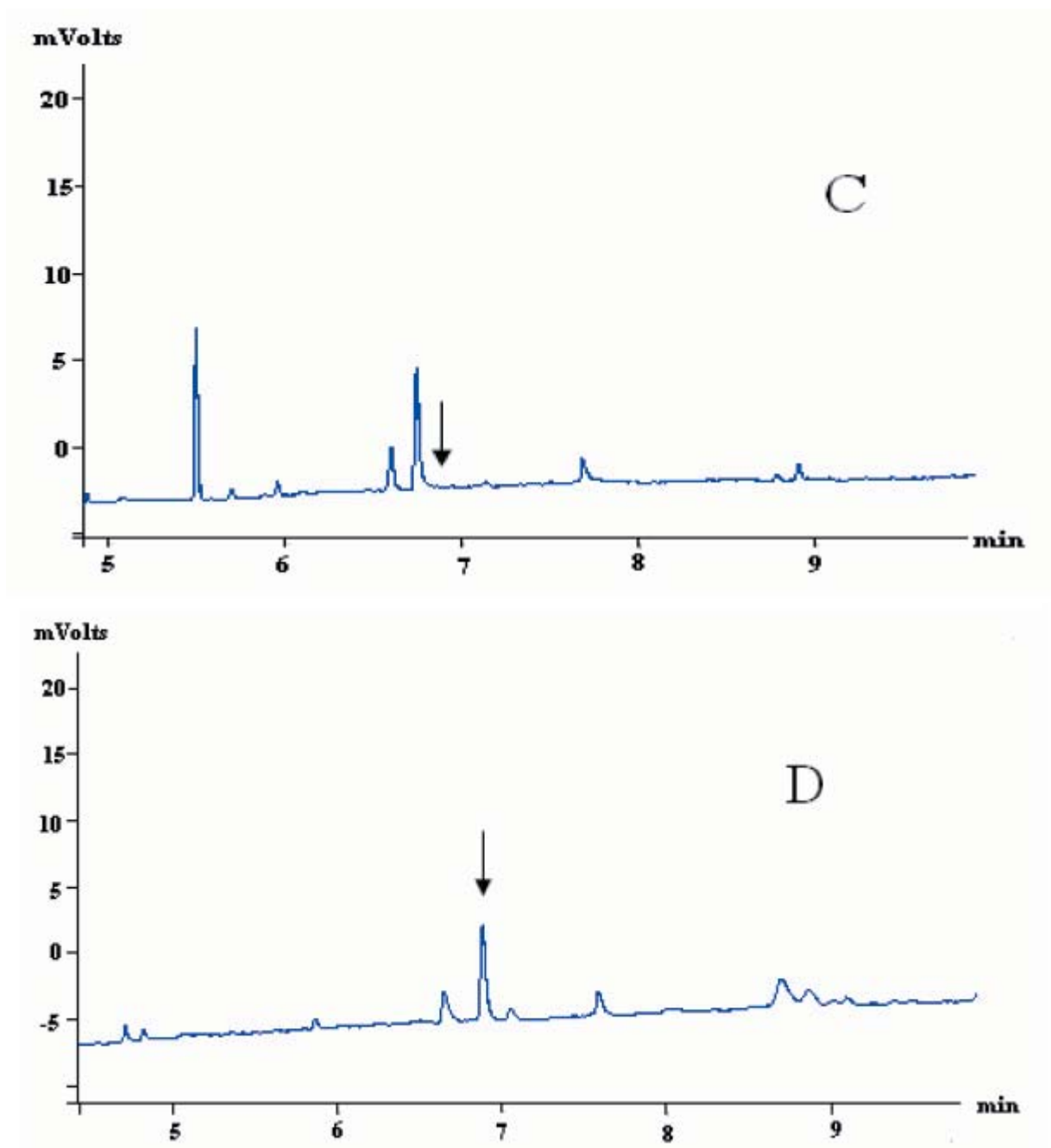
Figure 5. Chromatograms of monosultap spiked and blank samples(C) control soil sample (D) fortified soil at 0.1 mg /kg.
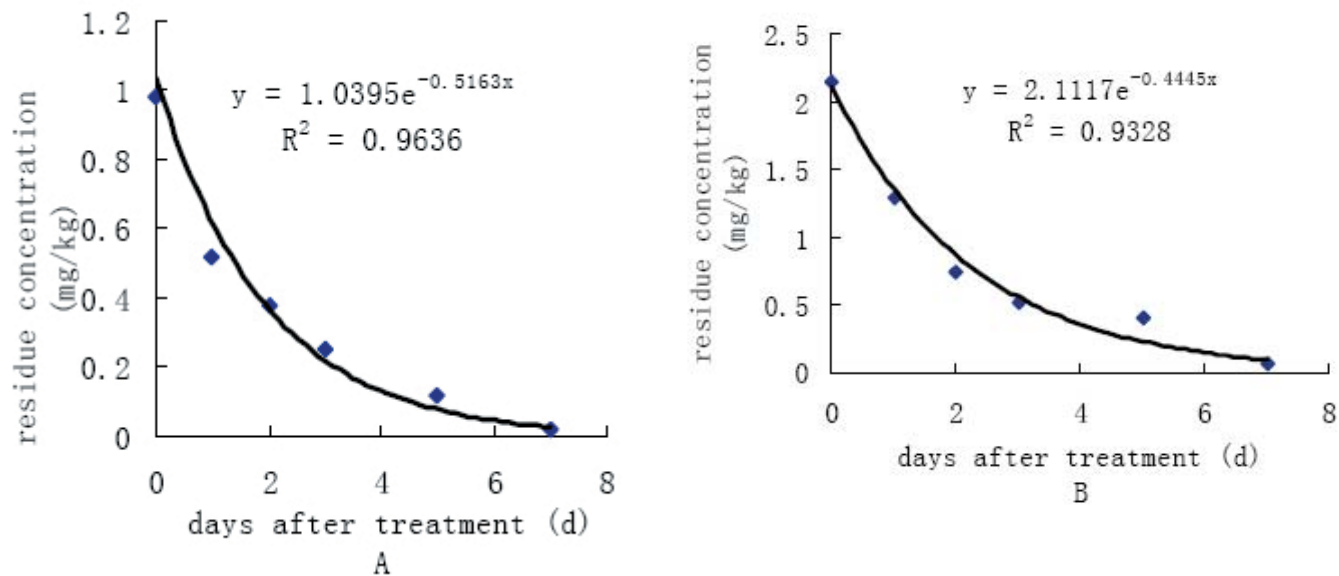
Figure 6. Dissipation rate of mososultap in tomato (A-- Treatment # 1 --180 (*a.c.*) g/ha; B--- Treatment # 2 --360 (*a.c.*) g/ha)
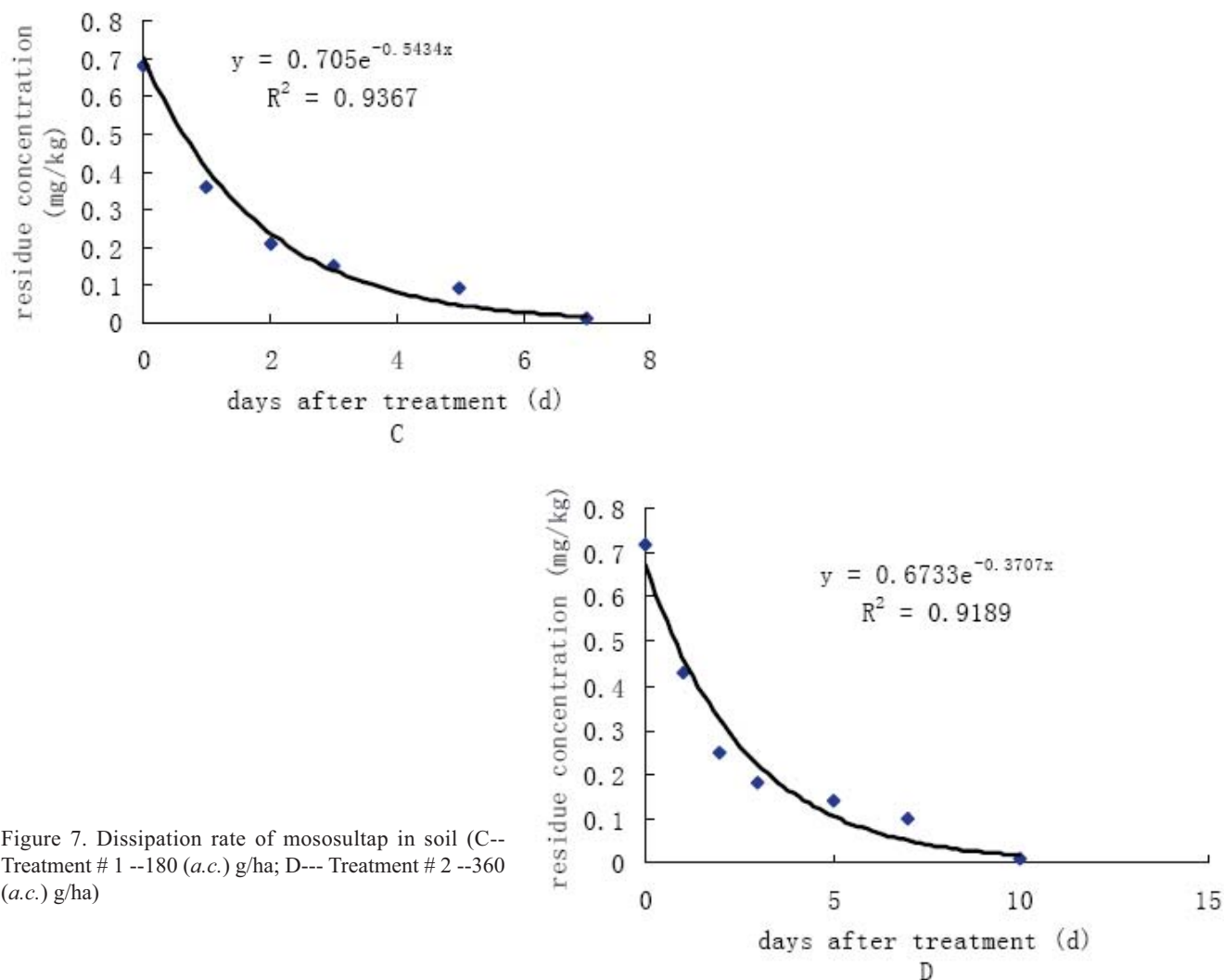

Figure 7. Dissipation rate of mososultap in soil (C-- Treatment # 1 --180 (*a.c.*) g/ha; D--- Treatment # 2 --360 (*a.c.*) g/ha)

related to time (t) was *C = 1.0395e^{-0.5163t} (R² = 0.9636)* and *C = 2.1117e^{-0.4445t} (R² = 0.9328)*, at Trt. 1 and Trt. 2, respectively, with the half-life times ($t_{1/2}$) of monosultap in tomato in a greenhouse was 1.35 and 1.56 days. At Trt. 1, the average residue levels of monosultap in tomato decreased from 0.98 (first sampling day) to 0.02 mg /kg (seventh sampling day), and from 1.10 to 0.067 mg/kg at the Trt. 2. Data presented in Table 2 and Figure 6 revealed that 98.0 % and 94.0 % residue reduction was achieved in treated tomato at application rates (180 and 360 a.i. g /ha) after 7 days, respectively. Pesticides decrease on account of fruit growing, evaporation, codistillation, thermodegradation, and photodegradation [9].

Monosultap residues in soil. The soil under investigation was neutral (6.81 pH), sandy loam in texture. The organic matter content was 2.69%. The residues in the top 20 cm degraded from 0.68 to 0.01 and 0.72 to 0.01 mg/kg in treatments 1 and 2 respectively, over a period of 7 days (Table 2). For Trt. 1 and Trt. 2, the half-life was 1.27 and 1.86 days, respectively. The dissipation rate of monosultap residues in soil also exhibited first order kinetics (Figure 7).

Conclusions

A rapid and sensitive method was developed for the determination of monosultap residues in tomato and soil samples. The proposed method involves optimization of the derivatization process, dispersive-SPE for purification, and GC-FPD(S) analysis. It showed satisfactory validation results, such as accuracy, precision, and selectivity. The results were further confirmed by gas chromatography-mass spectrometry (GC-MS). The developed method was applied to the determination of the dissipation rates of the studied pesticide in tomato and soil samples. The results indicated that monosultap disappeared quickly in both tomato and soil samples under the test field conditions, with a half-life of less than 2 days.

References

1. S. J. Lee, M. Tomizawa, and J. E. Cacida, *J. Agric. Food Chem.*, **51**, 2646 (2003).
2. Y. Hashimoto, and T. Okaichi, *Ann. N.Y. Acad. Sco.*, **90**, 667 (1960).
3. H. Hagiwara, and M. Numata, *Chem. Pharm. Bull.*, **16**, 311-317 (1968).
4. Z.J. Han, Z.K. Jiang, and W.H. Qian, *Mode. Agrochem.*, **3**, 5 (2004).
5. Z.T. Zheng, H.M. Wu, H.Y. Shi, G.N. Zhu, *Zhejing Agric. J.*, **2**, 92-95 (2004)
6. W.X. Lin, The compilation of Residue Limits Standards for pesticides and Veterinary Drugs in Foodstuffs in the world, Dalian Maritime University Press, Dalian. (2002).
7. J.L. Tadeo, C. Sánchez-Brunete, R.A. Pérez, and M.D. Fernández, *J. Chrom. A*, **882**, 175 (2000).
8. K. Konosho, *Agr. Biol. Chem.*, **34**, 935 (1970).
9. V.L. Garau, A. Angioni, A.A.D. Real, M. Russo, and P. Cabras, *J. Agric. Food Chem.*, **50**, 1929 (2002).